
# Determination of the Atomic Structure of Metal Nanoclusters from Aberration-Corrected Scanning Transmission Electron Microscope Images

Kusse Sukuta Bersha

**Faculty of Natural Sciences**
**School of Engineering and Natural Sciences**
**University of Iceland**
**2021**

# Determination of the Atomic Structure of Metal Nanoclusters from Aberration-Corrected Scanning Transmission Electron Microscope Images

Kusse Sukuta Bersha

Dissertation submitted in partial fulfillment of a
*Philosophiae Doctor* degree in Chemistry

Advisor
Prof. Hannes Jónsson

PhD Committee
Prof. Hannes Jónsson
Prof. Egill Skúlason
Dr. Elvar Örn Jónsson

Opponents
Prof. Jaakko Akola
Dr. Gísli Hólmar Jóhannesson

Faculty of Natural Sciences
School of Engineering and Natural Sciences
University of Iceland
Reykjavik, June 2021

Determination of the Atomic Structure of Metal Nanoclusters from Aberration-Corrected Scanning Transmission Electron Microscope Images
AC-STEM Image Analysis: Application to Gold Nanoclusters
Dissertation submitted in partial fulfillment of a *Philosophiae Doctor* degree in Chemistry



Faculty of Natural Sciences
School of Engineering and Natural Sciences
University of Iceland
Dunhagi 5
107, Reykjavik
Iceland

Telephone: 525-4000

Bibliographic information:
Kusse Sukuta Bersha, 2021, *Determination of the Atomic Structure of Metal Nanoclusters from Aberration-Corrected Scanning Transmission Electron Microscope Images*, PhD dissertation, Faculty of Natural Sciences, University of Iceland, 90 pp.

ISBN XXISBN

Printing: Háskólaprent, Fálkagata 2, 102, 107 Reykjavík
Reykjavik, Iceland, June 2021

# Abstract

Determining the atomic structure of nanoclusters is a challenging task and a critical one for understanding their chemical and physical properties. To fully understand the properties of a nanocluster, it is necessary to know the positions of the atoms in the nanocluster. Recently, the high-resolution aberration-corrected scanning transmission electron microscope (AC-STEM) technique has provided valuable information about such systems. While the AC-STEM experimental equipment is highly developed, the analysis of the images in terms of the atomic structure of the clusters is still often qualitative rather than quantitative.

In this work, a general method applicable in studies of irregular atomic structures has been developed for quantitative analysis of AC-STEM images of nanoclusters. An objective function formed by a linear combination of a measure of the agreement of a simulated image with the measured AC-STEM image plus an approximate description of the atomic interactions is used in a global optimization algorithm to extract the atomic coordinates. The method is first illustrated by analyzing synthetic images generated from regular as well as irregular structures of $Au_{55}$ nanocluster. As the method does not rely on the alignment of atoms, all the structures can be successfully determined even when a significant level of noise is added to the images. The method is then applied to an experimental AC-STEM image of a $Au_{55}$ nanocluster, a particularly challenging case since the atomic structure is irregular. Analysis of the local structure shows that the cluster is a combination of a part with icosahedral structure elements and a part with local atomic arrangement characteristic of a crystal packing, including a segment of a flat surface facet. The energy landscape of the cluster is explored in calculations of minimum energy paths between the optimal fit structure and other candidates generated in the analysis. This reveals low energy barriers for conformational changes, showing that such transitions can occur on laboratory timescale even at room temperature and lead to considerable changes in the AC-STEM image. Furthermore, the paths reveal additional cluster configurations, some with lower DFT energy and providing nearly as good fit to the experimental image.

Detailed analysis of AC-STEM images using theoretical modeling requires a reliable, quantitative measure of the extent to which a simulated image agrees with an experimentally measured image. A simple sum of pixel-by-pixel squared errors turns out to be unreliable and a more advanced measure is needed. A method based on the Speeded Up Robust Features (SURF) algorithm is applied to match simulated images to an experimental AC-STEM image of a $Au_{55}$ nanocluster. The method provides a quantitative measure that more closely corresponds to a visual assessment of image similarity.

# Útdráttur

Ákvörðun á uppröðun atóma í nanóklösum er erfitt verkefni en mjög mikilvægt til að öðlast skilning á efna- og eðlisfræðilegum eiginleikum þeirra. Nýleg mælitækni, spegilvilluleiðrétt og skannandi gegnumlýsingar rafeindasmásjá (e. aberration corrected scanning transmission electron microscope, AC-STEM) hefur gefið mikilvægar upplýsingar um slík kerfi. Þótt mælitækin séu háþróuð er úrvinnslan á mæligögnunum, sem er tvívíð mynd af klasanum á atómskala, oft ónákvæm og ekki magnbundin enn sem komið er. Í verkefninu er þróuð aðferðafræði til að vinna úr myndum sem koma úr AC-STEM mælingum. Þar er mat á samræminu milli útreiknaðrar myndar við mældu myndinarinnar ásamt mati á orku nanóklasans notað í bestunarreikningum til að ákvarða hnit atómanna. Fyrst er aðferðin prófuð fyrir líkön af AC-STEM myndum fyrir bæði reglulega og óreglulega $Au_{55}$ nanóklasa. Ekki er nauðsynlegt að atómin myndi raðir í klasanum og einnig er hægt að finna réttu hnitin þótt suð sé til staðar. Þá er aðferðinni beitt á mælda AC-STEM mynd af $Au_{55}$ klasa. Þetta er sérstaklega krefjandi dæmi því staðsetning atómanna er óregluleg í þessum klasa. Greining á staðbundinni uppröðun atómanna sýnir að klasinn er samsettur úr tveimur hlutum, annar með strúktúreiningar sem einkenna íkósahedru og hinn dæmigerður fyrir atóm í kristal og þar er jafnframt að finna bút af flötu yfirborði. Orkulandslag klasans er kannað með reikningum á lágmarksorkuferlum milli strúktúrsins sem gefur besta samsvörun við mælingarnar og annarra strúktúra sem einnig sýna góða samsvörun. Í ljós kemur að orkuhólarnir milli þessara strúktúra eru gjarnan lágir og slíkar umraðanir atómanna geta því greiðlega átt sér stað á meðan á mælingunum stendur og þar með haft áhrif á AC-STEM myndina. Ferlarnir leiða einnig í ljós nýja strúktúra sem sumir hafa lægri DFT orku og gefa næstum jafn góða samsvörun við myndina sem fékkst með mælingunum. Ítarleg úrvinnsla á AC-STEM myndum með útreikningum fyrir líkön af strúktúrum krefst þess að áreiðanlegt tölulegt mat sé hægt að leggja á hversu góð samsvörunin er. Í ljós kemur að einföld summa af kvaðrati frávikanna í styrk allra dílanna á myndinni er ekki góður mælikvarði á gæðin. Aðferð sem byggist á hraðaðri greiningu á afgerandi kennileitum (speeded up robust features, SURF) er þróuð og notuð til að bera saman reiknaðar myndir og mælda fyrir $Au_{55}$ klasann. Þessi aðferð gefur magnbundið mat á samsvörunina sem samræmist vel niðurstöðum sem fást við skoðun myndanna.

*Dedication*

*This thesis is dedicated to my late mother, Karato Beyene, and my father, Sukuta Bersha. I would also like to dedicate this thesis to my late brother-in-law Seifu Keylata.*

# Table of Contents

# List of Figures

# List of Tables

# List of Original Articles

## Publications included in the thesis

**I.** K. Sukuta, M. Van den Bossche, A. Pedersen, H. Jónsson. 2017. Nanocluster structure deduced from AC-STEM images coupled to theoretical modelling. *Nanosystems: Physics, Chemistry, Mathematics*. 8 (6): 723-731.

**II.** Kusse S. Bersha, Alejandro Peña-Torres, Hannes Jónsson. From AC-STEM Image to 3D Structure: A Systematic Analysis of $Au_{55}$ Nanocluster. *Submitted to J. Chem. Theory Comput.*

**III.** K. Sukuta, H. Jónsson. Theoretical Analysis of AC-STEM Images of Nanoclusters: Feature Based Method for Assessing the Quality of Fit. *Submitted to Nanosystems: Physics, Chemistry, Mathematics*.

## Publications not included in the thesis

Manuel Plasencia Gutiérrez, Kusse Sukuta Bersha, Andreas Pedersen, Hannes Jónsson. Global Optimization Based on Saddle Point Searches. *Submitted*

# Abbreviations

**AABB** axis-aligned minimum bounding box. 17, 19

**AC-STEM** aberration-corrected scanning transmission electron microscope. 1, 3, 6, 7, 9, 17, 18, 20, 22, 29, 37, 43, 44

**ADF** annular dark-field. 6

**ASE** Atomic Simulation Environment. 13, 21

**BF** bright-field. 6

**BFGS** Broyden–Fletcher–Goldfarb–Shanno. 21

**CI-NEB** climbing image nudge elastic band. 27

**CNA** common neighbor analysis. 17, 26

**DFT** density functional theory. 2, 22, 23

**DFTB** Density-Functional based Tight-Binding. 4

**DoH** determinant of Hessian. 38, 39

**EMT** effective medium theory. 3, 4, 13, 14, 19, 22, 38, 43

**EXAFS** extended X-ray fine structure spectroscopy. 3

**FCC** face-centered cubic. 2, 3

**GA** genetic algorithm. 4, 21, 22, 43

**GGA** generalized gradient approximation (GGA). 23

**GM** global minimum. 19

**GOUST** global optimisation using saddle traversals. 21, 22, 43

**HAADF** high angle annular dark field. 6, 9

**LoG** Laplacian of Gaussian. 11

**MEP** minimum energy path. xi, 17, 27

**MSE** mean squared error. 29, 44

**OpenCV** open-source computer vision. 37

**PBEsol** Perdew–Burke–Ernzerhof functional revised for solids. 23

**RMSD** Root-mean-square deviation. 14, 15, 27

**SD** standard deviation. 19

**SERS** surface enhanced Raman spectroscopy. 1

**SIFT** Scale-invariant Feature Transform. 44

**SP** saddle point. 21

**STEM** scanning transmission electron microscope. 5, 15

**SURF** Speeded up Robust Features. 29, 30, 32–35, 37, 38, 44

**VASP** Vienna ab initio simulation package. 23

**XRD** X-ray powder diffraction. 3

# Acknowledgments

I would like to express my deepest gratitude to my advisor Prof. Hannes Jónsson for his guidance and feedback throughout this project. Without his encouragement, continuous support, and patience, this thesis would hardly have been completed.

I am grateful to the University of Iceland Doctoral Fund for the fellowship opportunity to support my research. I am also thankful to the Icelandic Research Fund and the University of Iceland Research Fund. I would like to thank the Icelandic Research High Performance Computing (IRHPC) center for providing me computational resources to carry out calculations.

I would like to thank my Ph.D. opponents Prof. Jaakko Akola and Dr. Gísli Hólmar Jóhannesson, and my Ph.D. committee Prof. Egill Skúlason and Dr. Elvar Örn Jónsson for the thoughtful comments and recommendations on this dissertation.

This work would not have been reality without the kind support and help of many individuals. I would like to extend my sincere thanks to Dr. Maxime Van den Bossche, Dr. Alejandro Peña-Torres, Dr. Andreas Pedersen, and Dr. Manuel Plasencia Gutiérrez for their invaluable advice and contributions to my work. I would like to express my special thanks to Dr. BingCui Qi who introduced me to my supervisor.

Finally, I would like to thank my family for their continuous support and encouragement throughout my years of study. I would like to thank my beloved wife, Miheret Soka Gignarta, who is always by my side, and my beloved children Joshua and Elijah.

# 1 Introduction

Nanoclusters consist of a small number of atoms, at most in the tens, and often exhibit properties different from their larger counterparts.[1–3] Bulk gold, for example, has long been regarded as an inert metal with very low chemical and catalytic activity.[4] However, gold nanoclusters absorbed on metal oxides have shown remarkable catalytic activity.[5,6] It has, for example, been shown that carbon monoxide (CO) oxidation, an important reaction for cleaning exhaust, can occur readily below room temperature in the presence of Au nanoclusters deposited on a $TiO_2$ surface.[6] Carbon monoxide oxidation on gold nanoparticles are shown to be highly structure-dependent and only takes place on the low-coordinated corner atoms.[7] Understanding the structure of nanoparticles is therefore critical in the tailoring of new and better catalysts.

Metal nanoclusters have attracted much research interest in recent years for potential applications in various areas. Their strong reactivity, fluorescence, and magnetic property have attracted many researchers to exploit these properties for useful applications. Medical research is constantly looking for new and improved treatments for diseases, creating an enormous demand for scientific research to discover such new treatments. Metal nanoparticles can be used for targeted delivery of drugs with serious side effects to difficult sites such as the brain and retina.[8] Metal nanoclusters can be used to target tumors and provide detection using surface enhanced Raman spectroscopy (SERS).[9] Since metal nanoclusters are magnetic materials and can be embedded in glass, they can be used in optical data storage that can be used for many years without any loss of data.[10]

The relationship between structure and function underpins all modern chemical intuition and understanding. Only after identifying the ordering of the atoms can one reliably assess the various properties such as chemical reactivity. The development of aberration-corrected scanning transmission electron microscope (AC-STEM) has enabled researchers to obtain high-resolution images of nanoclusters. However, the analysis of the images has remained qualitative. In this thesis, a method that can be used to extract atomic coordinates from AC-STEM images is presented.

The rest of the thesis is organized is as follows. First, a literature review of nanoclusters is presented, followed by a brief introduction to AC-STEM imaging. The second section focuses on the methodology used in this thesis for the analysis of AC-STEM images. The application of the method to synthetic images is then presented, followed by the application to an experimental AC-STEM image of $Au_{55}$. Finally, a feature based image matching method is introduced to describe future challenges where the analysis of AC-STEM images will be pushed further by using computer vision algorithms.

## 1.1 Gold Nanoclusters

Gold has several qualities that have made it exceptionally valuable throughout history. More recently, gold nanoparticles have been researched and utilized in various applications such as catalysis. Gold catalysts are highly active for the oxidation of many components in ambient air at low temperatures, particularly CO and nitrogen-containing malodorous compounds.[11] This property offers scope for applications in air quality improvement and control of odors.[12,13] The catalytic properties of Au nanoclusters have been linked to specific cluster sizes and structures. The structure-property relationship has motivated many studies of the atomic-level structure of Au nanoclusters.

Several quantum mechanical calculations have shown that small gold clusters often adopt stable planar geometries. However, existing theoretical studies disagree on the critical size at which gold clusters favor 3D structures over 2D structures. For example, Xiao et al.[14] found planar geometries of Au clusters to be the global minima till the cluster size of $N = 13$ using density functional theory (DFT) calculations. In another theoretical calculation Santarossa et al.[15] used Born-Oppenheimer ab initio metadynamics to study the free-energy surface of neutral $Au_{12}$ and predicted coexisting planar/quasiplanar and tridimensional conformations separated by high-energy barriers. Using a genetic algorithm and meta-generalized density functional theory Johansson et al.[16] predicted the 2D and 3D structures almost isoenergetic at $N = 11$ while clusters with $N > 11$ are 3D.

In the size range $13 < N < 00$, global structural optimizations have shown that many topologically interesting low symmetry, disordered structures exist with energy near or below the lowest-energy ordered isomers. Using semiempirical Gupta potential and first-principles approaches, Garzón et al.[17] found almost equal structural stability for amorphous and ordered isomers of $Au_N$ clusters for ($N = 38, 55, 75$). Also using Gupta potential, Schebarchov et al.[18] mapped the equilibrium structures of $Au_N$ clusters in the size range $30 \leq N \leq 147$. Schebarchov et al. found the global minimum structure of most clusters in the size range $30 \leq N \leq 53$ to be ambiguous but with discernible fivefold disclinations. They predicted the global minima of larger clusters in the size range $54 \leq N \leq 147$ to be a lamellar-twinned or single-crystal face-centered cubic (FCC) lump or a decahedral motif with a single fivefold disclination. In addition to these theoretical calculations, experimental studies using high-resolution electron microscopy pointed out that the structure of small gold clusters was unstable and fluctuations between different geometries, primarily, between icosahedral and cuboctahedral structures were observed.[19,20]

Computational studies of the relative stability of magic-number nanoclusters indicate that for small Au clusters ($N < 100$), the icosahedral structure is more stable than the Ino-decahedral and the cuboctahedral structures.[21,22] For larger Au clusters ($500 < N < 1000$), the order of stability begins to change, with the Ino-decahedral structure becoming more stable than the icosahedral geometry. Further increasing the cluster size results in the order of stability changing to Ino-decahedral, cuboctahedral, icosahedral.

## 1.2 Structure and Stability of $Au_{55}$

The $Au_{55}$ cluster is of particular interest because it is one of the first and still widely investigated gold nanoparticles.[23,24] It is part of the family of so-called magic-number clusters and has been used as a model for small nanoclusters with a magic number of atoms. The term magic-number has to do primarily with nanoparticles forming perfectly completed geometries. In the case of $Au_{55}$, the inner shell contains 12 atoms surrounding the central atom, and the outer shell comprises 42 atoms surrounding the 13 atom core. Although $Au_{55}$ is one of the best-studied nanoparticles, the results of these studies are still inconsistent and sometimes contradictory regarding the structure and stability of $Au_{55}$.

The $Au_{55}$ structure was first characterised as cuboctahedral[24–26], illustrated in fig. 1.1(d), with single-crystal FCC atomic ordering. For example, Marcus et al.[25] performed optical absorption and temperature-dependent extended X-ray fine structure spectroscopy (EXAFS) measurements on $Au_{55}$ clusters and found results consistent with a cuboctahedron structure. Also using EXAFS Fairbanks et al.[26] studied the coordination environment of gold atoms in $Au_{55}(PPh_3)_{12}Cl_6$ and predicted a 3-shell cuboctahedral structure for the $Au_{55}$ cluster.

In theoretical calculation, Bao et al.[27] found a slightly different structure with FCC order, shown in fig. 1.1(e), by using the Gupta empirical potential and minima hopping global optimization method. The same structure had previously been identified as the global minimum for Sutton-Chen potential.[28] More recently, Schebarchov et al.[18] performed global optimisation of $Au_{55}$ and again found the global minimum to be FCC. They explained the disparity between the two by the differences in surface packing. The 42 surface atoms in the symetric cuboctahedron form only (100) facets, which are known to be particularly unfavourable but in the global minimum structure the 45 surface atoms are more close-packed and exhibit mainly (111) character.

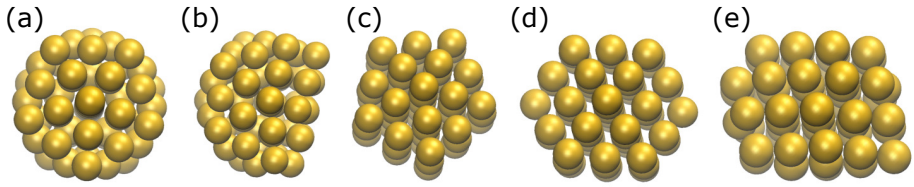


*Figure 1.1. The structure of some $Au_{55}$ isomers.(a) Icosahedral, (b) Structure found by Garzón et al.[17], (c) Ino-decahedral, (d) Cuboctahedral, (e) FCC Structure predicted by effective medium theory (EMT)*

Theoretical calculations by Garzón et al.[17] found several amorphous low-energy structures for $Au_{55}$. The lowest-lying amorphous isomer shown in fig. 1.1(b) was proposed as the global minimum. Similar results were found experimentally using X-ray powder diffraction (XRD)[29], AC-STEM[20], and photoelectron spectroscopy measurements.[30,31] More recently, $Au_{55}$ structures with subsurface cavities have also been reported from

theoretical calculations.[31–33] Van den Bossche[33] used a genetic algorithm (GA) optimization using Density-Functional based Tight-Binding (DFTB) and found the lowest energy $Au_{55}$ structure to be disordered and with cavities below the external shell. The presence of such cavities has previously been attributed to relativistic effects.

## 1.3 Theoretical Methods of Cluster Investigation

While quantum mechanical calculations are capable of providing accurate description of materials, their applications are limited by their high computational cost. Classical empirical potentials can be used to model large systems. However, one of the biggest drawbacks of classical simulations is that results are only as good as the force-field used to obtain them.

### 1.3.1 Effective Medium Theory Potential

The effective medium theory (EMT)[34] is an approximation in which models based on density-functional theory are used to describe the properties of solids metals. The basic idea behind EMT is to estimate the energy of an actual system by calculating the energy of the same in a well-known reference system and then estimate the difference between the two energies. Today there exist numerous many-body interatomic potentials which are based on EMT, in which the total energy is written in the form

$$E_{tot} = \sum_i F\left(n_i\left(\mathbf{R}_i\right)\right) + \frac{1}{2}\sum_{i,j}\phi\left(\mathbf{R}_i - \mathbf{R}_j\right), \tag{1}$$

where $F$ is a function of the electron density, and $\phi$ is a pair potential. In EMT the real material is replaced by jellium which consists of a homogeneous electron gas, formed by the free electrons of the metal and a constant positive background density created by the metal ions.

### 1.3.2 Gupta Potential

The Gupta potential[35] for metals is based on a second-moment approximation of the electron density of states in the tight-binding model. It contains a pairwise Born–Mayer repulsive term and an attractive term including the n-body effect, which is taken from the second moment approximation of the electron density states of the tight-binding model.[36] As a function of interatomic distance $r_{ij}$, the Gupta potential is expressed as:[18]

$$V = \sum_{j=1}^{N}\left(A\sum_{i\neq j}\exp\left(-\frac{p(r_{ij}-r_0)}{r_0}\right) - \left(\sum_{i\neq j}\xi^2\exp\left(-\frac{2q(r_{ij}-r_0)}{r_0}\right)\right)^{\frac{1}{2}}\right) \tag{2}$$

Schebarchov et al.[18] used $\xi = 1.855\,\text{eV}$, $A = 0.2197\,\text{eV}$, $p = 10.53$, $q = 4.30$, and $r_0 = 2.88\,\text{Å}$ in their calculations to get the structure shown in fig. 1.1(e).

## 1.4 Scanning Transmission Electron Microscopy

Scanning transmission electron microscope (STEM) is a microscopy technique whereby a beam of electrons is transmitted through a thin sample forming a high-resolution image. The first STEM was invented by Von Ardenne [37] in the 1930s as an alternative to light microscope to overcome the diffraction limit of visible light. By the early 1990s, improvements in STEM allowed for samples to be imaged with 2 Å resolution, providing what was at the time unprecedented clarity. [38] Over the years, the improved quality and stability of the electromagnetic lenses together with the development of aberration correctors have greatly improved the resolution of the STEM. Today, nanoclusters can be visualized with sub-Ångström resolution [39]. In this section, a brief review of the basic principles of STEM imaging is given in a simple, descriptive, and non-mathematical fashion.

Figure 1.2 shows a schematic diagram of STEM configuration. An electron beam is focused to a fine spot by the condenser lens system and scanned over the sample point by point in a raster illumination system. Annular detectors beneath the specimen are used to collect scattered electrons and integrated into an image as a function of probe position. The resulting image contrast depends largely on the collection range of the detector.

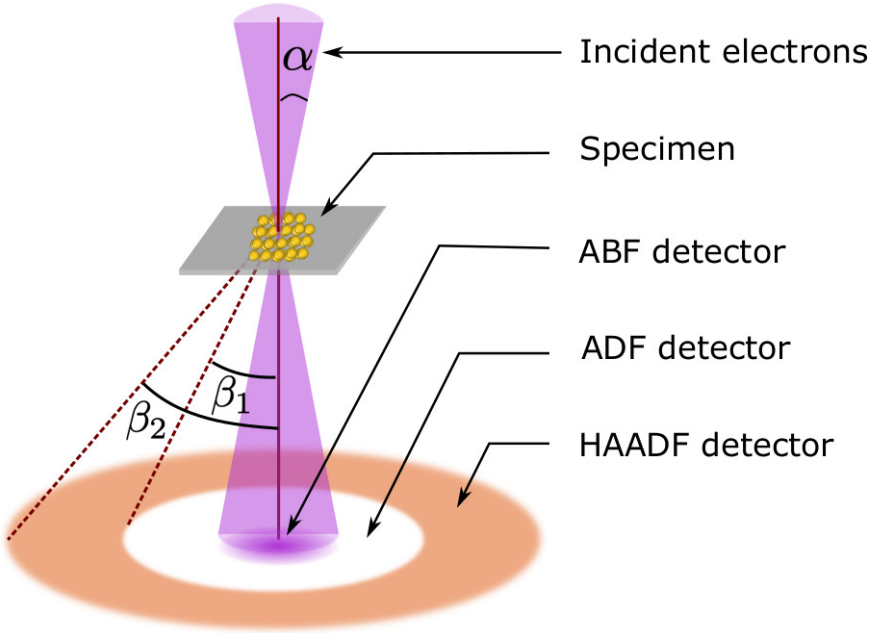


*Figure 1.2. Schematic diagram of a basic scanning transmission electron microscope (STEM). A focussed electron beam with convergence semi-angle $\alpha$ is raster-scanned over the sample. Scattered electrons are collected by an annular detector with inner and outer angle $\beta_1$ and $\beta_2$, respectively. Image adapted from ref.* [40]

### 1.4.1 STEM Detectors and Imaging Modes

Depending on the collection semi-angle, various images can be obtained corresponding to different contrast mechanisms.[41,42] Bright-field (BF) detectors are located in the path of the transmitted electron beam and are often used to provide complementary images to those obtained by annular dark-field (ADF) imaging. When the inner angle of the detector is greater than the convergence angle of the probe, an ADF image is recorded.[43] Thus, images in ADF mode are formed by electrons incident on an annular detector, which lies outside of the path of the directly transmitted beam.

High angle annular dark field (HAADF) is a technique that produces an annular dark-field image formed by very high angle, incoherently scattered electrons. In this setup, mainly Rutherford scattered electrons are recorded.[44] As a result, the image contrast in an HAADF image depends largely on the sample thickness and the atomic number. For elements with a higher atomic number, more electrons are scattered at higher angles due to greater electrostatic interactions between the nucleus and electron beam. Because of this, the HAADF detector senses a greater signal from atoms with a higher atomic number, causing them to appear brighter in the resulting image. The high dependence of the image contrast on the atomic number makes HAADF a useful way to easily identify small areas of an element with a high atomic number on the surface of a material with a lower atomic number.

### 1.4.2 Aberration Correction

The successful implementation of aberration correction to scanning transmission electron microscopy (AC-STEM) has enabled images with atomic resolution to be acquired. Before the introduction of aberration correction, a spatial resolution of 2 Å could be reached at best.[45] After aberration correction, AC-STEM was demonstrated with spatial resolution of 1.9 Å in 1997[46] and soon after in 2000 with 1.36 Å resolution[47]. Today, AC-STEM is capable of sub-Ångström resolution, achieving a spatial resolution of 0.5 Å in 2008[39]. The development of advanced aberration correctors has made it possible to identify individual atomic columns of crystalline nanoclusters with unprecedented clarity.

### 1.4.3 Applications of AC-STEM Imaging

More than 60% of the industrial products and 90% of the processes involving chemical reactions are based on catalysis, and innovations are increasingly reliant on catalysis.[48] Most catalytic processes are heterogeneous and often comprise heavy transition metals dispersed on light support, which is an ideal situation for HAADF imaging mode of AC-STEM. The most important research area in heterogeneous catalysts is understanding the relationship between the catalytically relevant surface structures and catalyst activity and selectivity for a particular chemical reaction. The main role of AC-STEM microscopy is to provide an atomic-level description of the underlying catalyst. The combination of first-principles theory and aberration-corrected STEM

imaging has been widely used to study transition metal nanoparticles' catalytic activity. For example, Rashkeev et al.[49] used aberration-corrected STEM and first-principles calculations to study the mechanism for the low-temperature oxidation of CO to $CO_2$ by Au nanoparticles on $TiO_2$ support. They used Au nanoclusters containing between 5 and 35 atoms deposited on a $TiO_2$ surface in the experiments. Theoretically, they found that low coordination accompanied by bond weakening in Au nanoclusters is the key to the catalytic activity of the nanoparticles. They confirmed this experimentally from atomically resolved Z-contrast AC-STEM images. From AC-STEM images, they observed many individual Au atoms when deposited, but after reduction to the active form, the atoms are much less visible, confirming bond weakening in catalytically active Au nanoparticles.

### 1.4.4 AC-STEM Image Interpretation and Simulations

Despite the high resolving power of AC-STEM, the atomic structure of nanoclusters is not easily extracted from the image. Until now, the most widely used method for identifying nanoparticle structure from AC-STEM is based on visual inspection. A catalog of simulated images is generated from ideal structures, and the experimental image is compared to the catalog by visual inspection that requires a skilled technician with experience. While this type of analysis is in many ways good enough to identify ordered structures, comparing AC-STEM images of disordered structures by eye is extremely difficult. This is, in particular, true for small Au clusters such as $Au_{55}$ where the atomic ordering is quite irregular. This suggests the necessity for more robust, powerful, and automated analysis tools for identifying nanoparticles in a more efficient and faster way.

The multislice algorithm is widely used in the simulation of high-resolution AC-STEM and serves as a valuable tool for analyzing experimental images[50,51]. In the multislice algorithm, the sample is divided into many slices. Each slice is thin enough to be approximated as a simple phase shift of the electron beam. The incident electron beam enters the top, propagates through the sample, and exits at the bottom. The electron beam propagates between slices as a small angle outgoing wave. The wave is transmitted through a slice and then propagates to the next layer. The multislice simulation can be very time-consuming, which can be a hurdle when one has to deal with a large set of images.

Recently, several AC-STEM image analysis methods based on parameter estimation procedures have been developed. These methods rely on the availability of a parametric model to describe the expectations of the experimental image. The combination of this technique with AC-STEM images has been used to determine structure parameters, such as atomic column positions[52]. For AC-STEM images of crystalline structures, acquired along a major zone-axis, intensities peaks at the atomic column positions and can be modeled as a superposition of Gaussian functions. The unknown parameters are estimated by fitting the model to the experimental image using a goodness of fit criterion, quantifying the similarities between the experimental images and the model.

# 2 Methodology

It is well known that AC-STEM imaging in the HAADF mode offers the possibility to visually distinguish between different atomic column types[53]. However, direct interpretation of the images is inadequate when studying irregular structures such as $Au_{55}$ where the atoms are not lined up in well-defined columns. For such systems, a quantitative analysis of AC-STEM images is required. In this section, a general method applicable in the study of regular as well as irregular atomic structures is described.

## 2.1 AC-STEM Image Simulation

From measured AC-STEM images and detailed electron scattering calculations, Li et al.[21] found that at small cluster size (N < 1500), atoms within the cluster contribute nearly equally to the scattered electron intensity detected in the experiments and that the contribution of each atom can be approximated by a Gaussian. Based on these findings, the intensity at a given pixel can be approximated as a linear combination of the intensity contributions from all the atoms in the cluster. Thus the intensity of the image at pixel $(i, j)$ for a cluster consisting of $N$ atoms of the same type can be written as:

$$I_{ij}(\boldsymbol{x},\boldsymbol{y},\sigma) = \sum_{k=1}^{N} \mathcal{A} \exp\left( -\frac{\left(x'_i - x_k\right)^2 + \left(y'_j - y_k\right)^2}{2\sigma^2} \right), \tag{3}$$

where $\boldsymbol{x} = (x_1, \cdots, x_N)$ and $\boldsymbol{y} = (y_1, \cdots, y_N)$ are vectors of coordinates of the atoms, $x'$ and $y'$ are the spatial coordinates of the image pixels, and $\sigma$ and $\mathcal{A}$ are the width and height of the Gaussian peak. An atom makes a full contribution to the intensity for a given grid point when that point lies directly above the center of the atom. The height of the Gaussian peak can be approximated by matching the integrated intensity of the atoms to the integrated intensity of the experimental image and solving for $\mathcal{A}$ as:

$$\mathcal{A} = \frac{1}{2\pi\sigma^2 R^2 N} \sum_{i=1}^{m} \sum_{j=1}^{n} I'_{ij}, \tag{4}$$

where $I'$ denote the idealized AC-STEM signal that one would obtain without any noise in the image acquisition, $m$ and $n$ give the number of rows and columns of pixels in the image and $R$ is the resolution of the image in pixels/Å.

The unknown parameters of the model are the atom coordinates and the width ($\sigma$) of the Gaussian. These are estimated by fitting the model to the experimental data. The goodness of fit ($\chi^2$) can be estimated as the pixel-by-pixel difference between the measured ($I'$) and calculated ($I$) intensity as:

$$\chi^2(\boldsymbol{x},\boldsymbol{y},\sigma) = \sum_{i=1}^{m}\sum_{j=1}^{n}\Big(I'_{ij} - I_{ij}(\boldsymbol{x},\boldsymbol{y},\sigma)\Big)^2. \tag{5}$$

## 2.2 Minimization of the Residual Sum of Squares

An important aspect of the analysis method is the systematic optimization of the atom coordinates as well as the width parameter in the Gaussian representing the signal originating at an atom. Using eq. (5), the steepest descent direction for reducing the discrepancy between a simulated and measured images can be obtained by differentiating $\chi^2$. Using $I_{ij} = I_{ij}(\boldsymbol{x},\boldsymbol{y},\sigma)$ and $\chi^2 = \chi^2(\boldsymbol{x},\boldsymbol{y},\sigma)$ to shorten the notation, the partial derivative of $\chi^2$ with respect to the $x$-component of atom $k$ can be written as:

$$\frac{\partial\chi^2}{\partial x_k} = -2\sum_{i=1}^{m}\sum_{j=1}^{n}\left(I'_{ij} - I_{ij}\right)\frac{\partial I_{ij}}{\partial x_k}, \tag{6}$$

with

$$\frac{\partial I_{ij}}{\partial x_k} = \frac{1}{\sigma^2}\left(x'_i - x_k\right) I_{ij}(x_k, y_k, \sigma). \tag{7}$$

Substituting Eq. 7 into Eq. 6 and using $I_{ij}^{(k)} = I_{ij}(x_k,y_k,\sigma)$, the $x$-component of the steepest descent vector for atom $k$ is:

$$\frac{\partial\chi^2}{\partial x_k} = -\frac{2}{\sigma^2}\sum_{i=1}^{m}\sum_{j=1}^{n}\left(I'_{ij} - I_{ij}\right)\left(x'_i - x_k\right) I_{ij}^{(k)}. \tag{8}$$

Similarly, the $y$-component of the steepest descent vector for atom $k$ is:

$$\frac{\partial\chi^2}{\partial y_k} = -\frac{2}{\sigma^2}\sum_{i=1}^{m}\sum_{j=1}^{n}\left(I'_{ij} - I_{ij}\right)\left(y'_j - y_k\right) I_{ij}^{(k)}, \tag{9}$$

and the $\sigma$-component is:

$$\frac{\partial\chi^2}{\partial\sigma} = -\frac{2}{\sigma^3}\sum_{i=1}^{m}\sum_{j=1}^{n}\left(I'_{ij} - I_{ij}\right)\Big(\left(x'_i - x_k\right)^2 + \left(y'_j - y_k\right)^2\Big) I_{ij}. \tag{10}$$

It is important to note in the above equations that $I_{ij} = I_{ij}(\boldsymbol{x},\boldsymbol{y},\sigma)$ represents the intensity from all atoms whereas $I_{ij}^{(k)} = I_{ij}(x_k,y_k,\sigma)$ represents the intensity from atom $k$ only.

The steepest descent displacement vector that reduces the image discrepancy most rapidly is calculated as:

$$d\chi^2 = \left[\frac{\partial\chi^2}{\partial x_1},\quad \frac{\partial\chi^2}{\partial y_1},\quad \frac{\partial\chi^2}{\partial z_1},\quad \cdots,\quad \frac{\partial\chi^2}{\partial x_N},\quad \frac{\partial\chi^2}{\partial y_N},\quad \frac{\partial\chi^2}{\partial z_N},\quad \frac{\partial\chi^2}{\partial\sigma}\right]. \tag{11}$$

## 2.3 The Combined Objective Function

Within the level of approximation given eq. (5), the AC-STEM image does not give any information about the $z$-coordinate of the atoms. Therefore, an objective function that also includes the energy of the cluster is defined to complement the image fit. The combined objective function is thus given by the weighted sum of the pixel-by-pixel fit and the estimate of energy of the cluster as:

$$f(\boldsymbol{x},\boldsymbol{y},\boldsymbol{z},\sigma) = \omega\chi^2(\boldsymbol{x},\boldsymbol{y},\sigma) + U(\boldsymbol{x},\boldsymbol{y},\boldsymbol{z}), \tag{12}$$

where $\boldsymbol{z}=(z_1,\cdots,z_N)$ corresponds to the $z$-coordinates of the atoms, $U$ is the energy and $\omega$ is a weight parameter used to control the relative importance of the two contributions.

The gradient of the combined objective function then consist of the negative atomic force plus a weighted contribution from the gradient of the image fit ($\chi^2$). The estimate of the energy ($U$) of the clusters does not need to be highly accurate. The most important information is in the image, but without some estimate of the optimal distance between atoms, it is impossible to assign the $z$-coordinates. Therefore, the estimate of the energy serves mainly to control the nearest neighbor distance between atoms and provide attraction so as to produce an intact cluster.

To get a good compromise between the information from the AC-STEM image and the energy estimate, a suitable value of $\omega$ needs to be determined. If $\omega$ is too small, the objective function is dominated by the potential energy. The optimization leads to a low energy structure that has no similarity to the experimental image. Conversely, if $\omega$ is too large, the objective function is dominated by $\chi^2$. The simulated image fits the experimental image nicely, but the resulting cluster structure may be relatively high in energy.

## 2.4 Generation of 3D Structures

The method starts out by detecting local maxima in the target image using a Laplacian of Gaussian (LoG) detector[54]. The LoG detector not only accurately locates the blob centers but also estimates the width of the Gaussian that fits the blob. The first atom is placed at the location of the blob with the strongest LoG response. The intensity contribution of the atom is then subtracted from the target image, and a second atom is placed at the location of the maximum in the reduced image. The $z$-coordinate of the atom is generated randomly while respecting a minimal interatomic distance. A local minimization of the objective function is then performed with more emphasis on image fitting than energy minimization. This process is continued until the coordinates of a predefined number ($N$) of atoms have been assigned. By repeating this process with different random number seeds, several 3D structures are generated. Starting from the initial structures, global optimization is then carried out by minimizing the combined objective function. The method can be applied to disordered as well as ordered clusters.

# 3 Application to Synthetic Images

Before analyzing experimental AC-STEM images, the developed method is first applied to synthetic AC-STEM images for which the atomic structure is known.To do this, target images are generated from ordered $Au_{55}$ nanoclusters with icosahedral, decahedral and cuboctahedral geometries as well as from the highly disordered Garzón $Au_{55}$ structure [17]. Given a 2D synthetic image of a nanocluster structure, the goal is to extract the three-dimensional atomic coordinates of the nanocluster from the image.

Hardball models of the structures used for testing are shown in fig. 3.3 alongside their synthetic images generated via the Gaussian approximation model in eq. (3). The images have dimensions of $25\,\text{Å}\times25\,\text{Å}$ and are sampled with $160\times160$ pixels. A Gaussian width of $\sigma=0.8\,\text{Å}$ is used to generate the images. The effectiveness of the method is investigated by performing a series of simulations at varying orientations by randomly tilting the structures away from zone axis alignment.

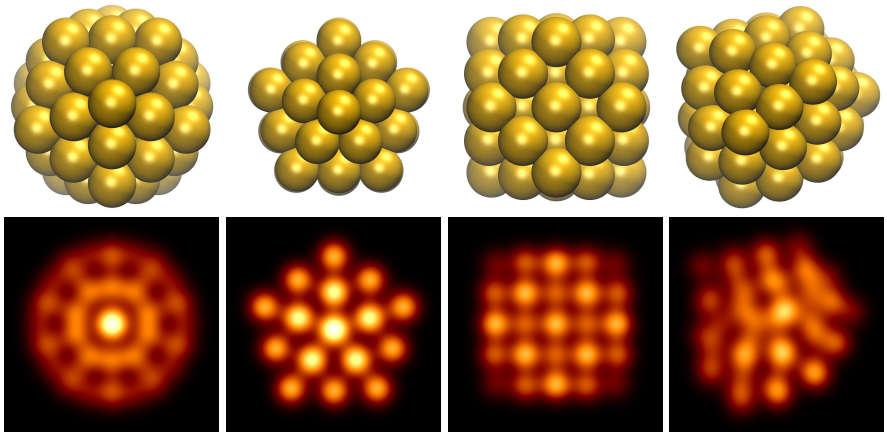

*Figure 3.3. Top: $Au_{55}$ hardball models for icosahedron, decahedron, cuboctahedron and the Garzón structures, respectively. Bottom: Corresponding simulated images.*

The estimate of the energy of the clusters is obtained from the effective medium theory (EMT) [55] potential energy function implemented in the Atomic Simulation Environment (ASE). This estimate does not need to be highly accurate. The most important information is in the image, but without some estimate of the optimal distance between atoms, it is impossible to assign the $z$-coordinates. The estimate of the energy serves mainly

to control the nearest neighbor distance between atoms and provide attraction so as to produce an intact cluster. The gradient of the total objective function then consists of the negative EMT atomic force plus a weighted contribution from the difference between the experimental image and the simulated one.

These structures are interesting test problems for several reasons. The symmetric structures, although simple in principle, are not optimal on the EMT potential surface. With the use of only EMT energy minimization, the method would never converge to any of these structures. The Garzón structure is more challenging as it is highly disordered plus the EMT predicts an entirely different optimal structure than the Garzón structure.

Figure 3.4 shows the convergence behavior of the GA calculations for different orientations of the Garzón structure. The curves start at high objective values due to the randomness in the initial structures but decrease monotonically as better structures are found. The statistics are based on 20 independent GA runs, with each run starting with 20 initial structures. Some of the GA runs find the target structure within the initial population obtained after the first phase, whereas a few runs use more than 50 candidates before the target structure is found. In all cases, the target structure is found with almost 100% success rate within 200 GA steps.

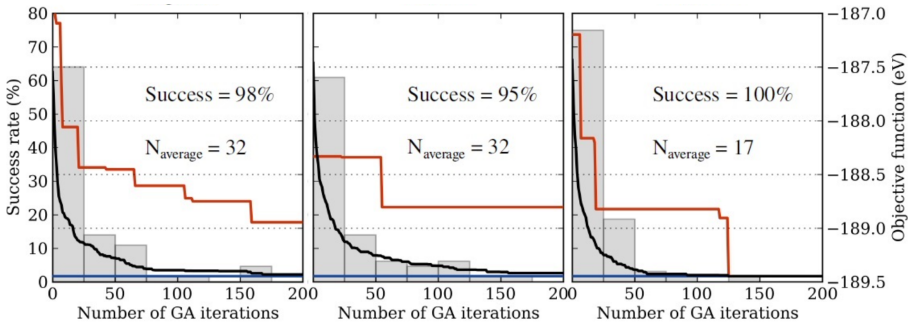


*Figure 3.4. GA optimization for 3 different orientations of the Garzón structure. The curves show the evolution of the best-scoring candidates in the best performing (lowest curve) and worst performing (highest curve) runs and the average over the 20 runs (middle curve).*

For each test case, the extracted structure matches well with the reference structure. Because we have the 3D coordinates of the structures, we can compare the atomic positions to quantify the similarity between the original and the reconstructed structures. A widely used method for comparing identical structures is to translate and rotate one structure with respect to the other to minimize the Root-mean-square deviation (RMSD).

The RMSD between two structures of $N$ atoms each can be calculated as

$$\mathrm{RMSD} = \sqrt{\frac{1}{N}\sum_{i=1}^{N}\Big((x_i - x_i')^2 + (y_i - y_i')^2 + (z_i - z_i')^2\Big)}, \tag{13}$$

where $(x,y,z)$ and $(x',y',z')$ are the coordinates of the original and extracted structures respectively. The average difference in atomic coordinates is less than 0.1 Å for the Garzón structures and much smaller for the ordered structures Figure 3.5 shows that the extracted structures for the Garzón structure. The extracted coordinates are in excellent agreement with the original structures.

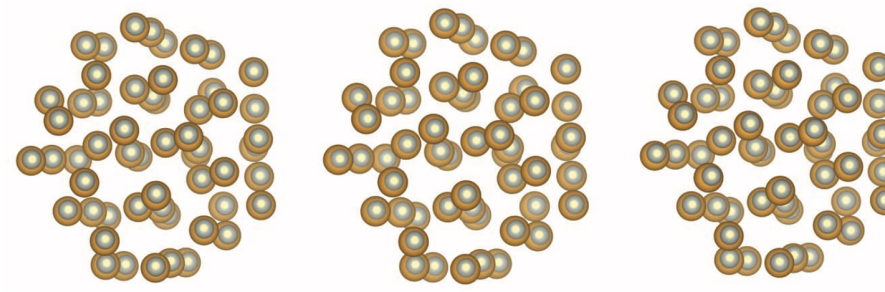

*Figure 3.5. The extracted structures (gray atoms) are superimposed over the target structures (gold atoms). The gray atoms have been rendered with smaller radius to make visual comparison easier.*

## 3.1 The Effect of Noise

Various levels of noise are added to the images to better emulate experimental data. While noise models are usually not studied in detail in the STEM literature, Gaussian noise models are used frequently in practice mainly because of their mathematical tractability in both the spatial and frequency domains. Therefore, the target images are corrupted by random noise drawn from a Gaussian distribution with zero mean and standard deviation proportional to the local intensity. In an additive zero mean Gaussian noise model, the noisy image $H$ is defined as:

$$H_{ij} = I_{ij} + \eta_{ij}\ ; \qquad \eta_{ij} \sim \mathcal{N}(0,\sigma) \tag{14}$$

where $I$ is the noise free image and $\eta_{ij}$ is a random number drawn from a normal distribution, $\mathcal{N}$, with mean 0 and standard deviation of $\sigma = \beta I_{ij}$.

Three different noise levels were added with $\beta = 0.1$, $\beta = 0.2$ and $\beta = 0.5$, respectively. The resulting images are shown in fig. 3.6 for the Garzón structure. At the highest noise level, $\beta = 0.5$, some pixels acquire negative intensities. The added noise is then adequately reduced by subsequent Wiener filtering[56]. The Wiener filter is an algorithm

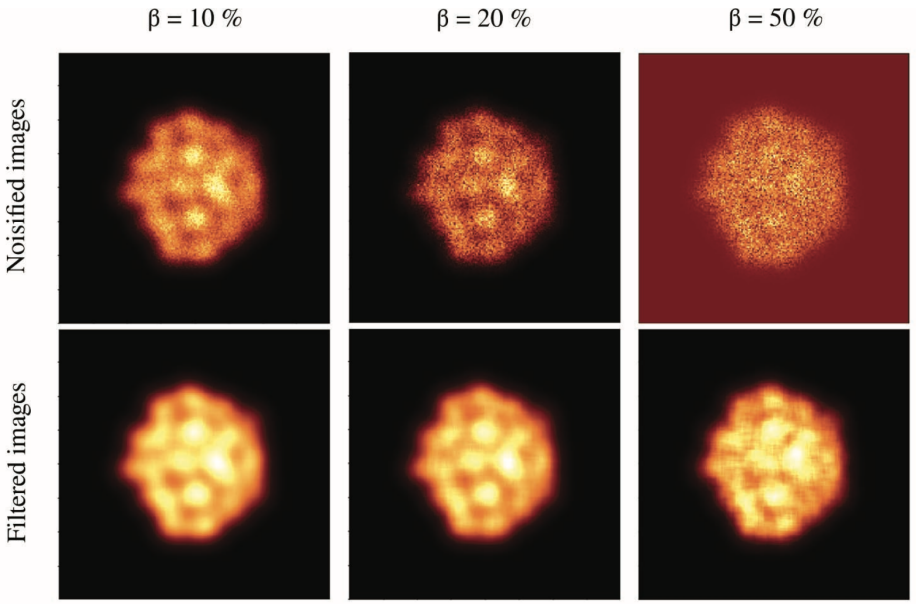


*Figure 3.6. Top row: Simulated STEM images with added noise levels. Bottom row: The corresponding images after Wiener filtering.*

optimized to find the minimum mean square error estimate of the original signal from a noisy measurement. The images obtained after such filtering are also shown in fig. 3.6.

It can be concluded that using the noisy but filtered images in the GA optimization only slightly increases the number of steps required to reach convergence. The optimal structures obtained using the filtered images agree closely with the reference Garzón structure. This indicates that the method is robust with respect to the presence of noise in the AC-STEM images.

Tests were also performed where the target image is generated after the test structures have been perturbed by adding random displacements in the $x$ and $y$ positions, drawn from a uniform distribution $[0, \alpha]$. Such tests effectively correspond to evaluating the relative difficulty of finding an optimal structure which is not close to a local minimum structure of the potential energy surface. The convergence data obtained for maximal displacements of $\alpha = 0.2\,\text{Å}$, $\alpha = 0.5\,\text{Å}$ and $\alpha = 1.0\,\text{Å}$ show that it is possible to use an objective function including both the potential energy and an image discrepancy term, even when the experimental AC-STEM image is affected by large noise.

# 4 Application to AC-STEM Images

The method is applied to an experimental AC-STEM image of $Au_{55}$ cluster for the extraction of atom coordinates from the image. The obtained clusters are compared on the basis of the total energy, coordination numbers of the atoms, and common neighbor analysis (CNA). The side length of the axis-aligned minimum bounding box (AABB) characterizing the overall shape of the cluster are compared. The energy landscape of the cluster is explored in calculations of minimum energy path (MEP) between the optimal fit structure and other candidates generated in the analysis. This reveals low energy barriers for conformational changes, showing that such transitions can occur on laboratory timescale even at room temperature and lead to large changes in the AC-STEM image.

## 4.1 Preparation of AC-STEM Image

The experimental image used in this work is adapted from figure 3(a) in ref.[20] Based on the scale bar presented in the image, a box of size roughly 2.5 nm × 2.5 nm containing the cluster is cropped from the image (see fig. 4.7). Although the image had been processed by the authors to remove noise and enhance image quality, some noise is still visible in the vicinity of the cluster, especially around the edges. For example, small bright spots that are spatially separated from the main cluster can be seen in the image, as indicated by red circles in fig. 4.7(b). These isolated features and small intensity patches around the edges are not considered as part of the cluster and are removed from the image. In this way, the noise in the image is significantly reduced as shown in figure fig. 4.7).

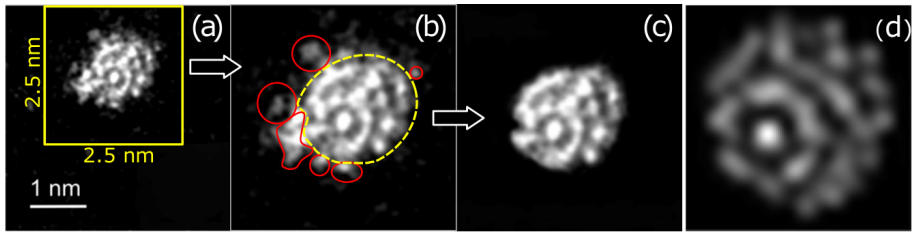


*Figure 4.7. Experimental AC-STEM image of $Au_{55}$ from ref.[20] (b) Cropped image. Noise can be seen in the vicinity of the cluster, as indicated by red circles. (c) Image used in the fitting process, with noise removed. (d) Best fit image in the ref.[20]*

## 4.2 Phase I: Generation of Initial Structures

The first phase starts out by locating local intensity maxima in the AC-STEM image. The first atom in the model is then placed at the location of the highest maximum and its $z$-coordinate is arbitrarily given a value of $z = 0$. The intensity contribution of this atom is then subtracted from the experimental image and a second atom is placed at the location of the maximum in the reduced image. The $z$-coordinate of the second atom, and all subsequent atoms, is generated randomly between $-10\,\text{Å}$ and $-10\,\text{Å}$ while ensuring a minimal interatomic distance of $2.8\,\text{Å}$. A local minimization of the combined objective function is performed with a weight of $\omega = 1000\,\text{eV}$ after the placement of each atom. This process is continued until the coordinates of a predefined number, $N = 55$ in this case, of atoms has been assigned. By repeating this process with different random number seeds, several three-dimensional atomic structures are generated with $(x,y)$ coordinates that almost perfectly fit the AC-STEM image, but have relatively high energy. They serve as input for a structure optimization procedure in the second phase.

The experimental AC-STEM image and the simulated one are in excellent agreement. Figure fig. 4.8 shows a comparison between the experimental image (inset a) and an image obtained by the fitting procedure described above (inset b). Horizontal line scans illustrate the excellent agreement with respect to both the peak positions and the relative peak intensities.

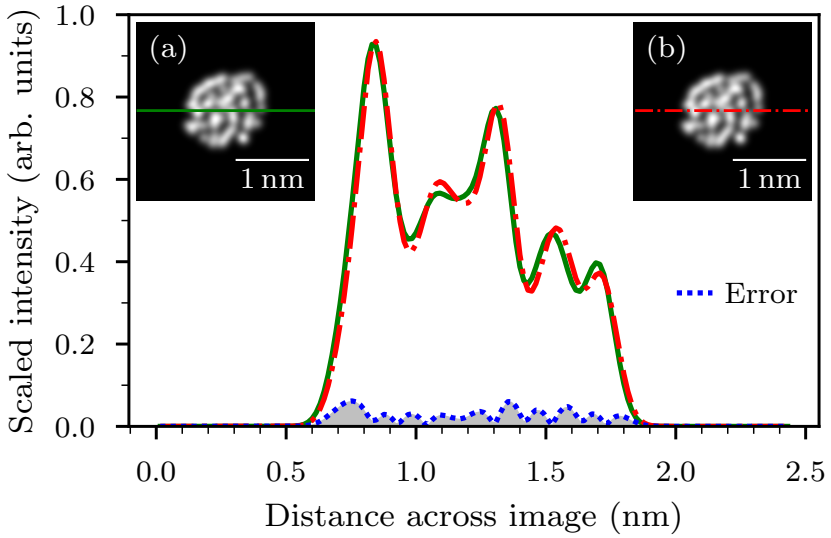


*Figure 4.8. (a) Experimental AC-STEM image taken from ref.[20]. (b) Simulated image of a structure obtained after the first phase of the fitting procedure. Horizontal line scans of the intensity are also shown. The solid green curve is for the experimental image and the broken red curve is for the simulated one. The difference between the two intensity profiles is shown by the blue dotted curve.*

At this point, the extracted structures are not compact as the $z$-coordinates of the atoms have not been optimized. Hence the clusters have relatively high energy and are slightly elongated in the $z$-direction as shown in table 4.1. The lowest energy structure obtained in the first phase is at least 1.219 eV higher in energy than the EMT global minimum (GM) structure. The AABB is used to characterize the shape of a cluster. The AABB side lengths $l_x$, $l_y$, and $l_z$ parallel to the cartesian coordinate axes are obtained by taking the absolute difference between the minimal and maximal value of the corresponding coordinates for the atoms in the cluster. The ratios of the average $l_x$ and $l_y$ to $l_z$ are approximately 0.91, and 0.84 showing a slight elongation along the $z$-axis. The table also shows the values obtains for the width $\sigma$ and amplitude $\mathcal{A}$ of the Gaussian. The values of *sigma* and $\mathcal{A}$ of the best fit structure are chosen and kept fixed during the optimization of the structures in the second phase.

*Table 4.1. Potential energy $\Delta E(\mathrm{eV})$ relative to the EMT GM, axis-aligned minimum bounding box (AABB) side lengths $l_x$, $l_y$, and $l_z$ (in Å), estimate of the Gaussian width $\sigma$(in Å), and the sum of squared intensity differences $\chi^2$ for 20 initial structures. The average (Mean) and standard deviation (SD) are also shown.*

| | $\Delta E$ | $l_x$ | $l_y$ | $l_z$ | $\sigma$ | $\mathcal{A}$ | $\chi^2$ |
|---|---|---|---|---|---|---|---|
| 1 | 1.219 | 10.047 | 9.042 | 10.228 | 0.600 | 0.008142 | 0.002203 |
| 2 | 1.478 | 10.070 | 9.013 | 10.962 | 0.606 | 0.007993 | 0.002808 |
| 3 | 1.688 | 9.981 | 9.188 | 9.958 | 0.615 | 0.007751 | 0.002173 |
| 4 | 1.766 | 9.885 | 9.283 | 10.159 | 0.606 | 0.008006 | 0.002029 |
| 5 | 1.793 | 9.900 | 9.221 | 10.233 | 0.612 | 0.007842 | 0.001950 |
| 6 | 1.893 | 9.889 | 9.279 | 10.371 | 0.598 | 0.008219 | 0.002312 |
| 7 | 2.006 | 9.796 | 9.386 | 10.860 | 0.601 | 0.008112 | 0.002814 |
| 8 | 2.030 | 9.996 | 9.266 | 10.128 | 0.610 | 0.007911 | 0.002943 |
| 9 | 2.077 | 9.806 | 9.204 | 11.736 | 0.588 | 0.008459 | 0.001820 |
| 10 | 2.077 | 10.028 | 9.176 | 10.177 | 0.594 | 0.008322 | 0.002132 |
| 11 | 2.135 | 10.049 | 9.042 | 10.248 | 0.595 | 0.008274 | 0.002161 |
| 12 | 2.198 | 9.995 | 9.220 | 11.168 | 0.610 | 0.007888 | 0.001925 |
| 13 | 2.281 | 9.773 | 9.094 | 11.067 | 0.599 | 0.008157 | 0.001627 |
| 14 | 2.321 | 9.849 | 9.168 | 11.455 | 0.592 | 0.008359 | 0.001451 |
| 15 | 2.350 | 9.889 | 9.126 | 10.952 | 0.600 | 0.008143 | 0.001630 |
| 16 | 2.355 | 10.053 | 9.296 | 11.064 | 0.598 | 0.008195 | 0.002147 |
| 17 | 2.515 | 9.995 | 9.195 | 11.593 | 0.606 | 0.007983 | 0.002452 |
| 18 | 2.677 | 9.919 | 9.214 | 12.070 | 0.598 | 0.008200 | 0.001507 |
| 19 | 2.944 | 9.985 | 9.140 | 11.468 | 0.598 | 0.008179 | 0.002439 |
| 20 | 2.984 | 9.937 | 9.165 | 11.739 | 0.596 | 0.008255 | 0.001764 |
| Mean | 2.139 | 9.942 | 9.186 | 10.882 | 0.6011 | 0.008119 | 0.002114 |
| SD | 0.435 | 0.089 | 0.091 | 0.639 | 0.0069 | 0.000179 | 0.000418 |

## 4.3 Phase II: Optimization of the Structures

An optimization of the atomic coordinates of the cluster generated in the first phase is carried out by minimizing the combined objective function given by eq. (12). In order to get a good compromise between the information from the AC-STEM image and the energy estimate, a suitable value of $\omega$ needs to be determined. To do this, different values for $\omega$ are examined. Figure 2 shows the relationship between image fit and cluster energy for different values of the weight parameter. When $\omega$ is small, the objective function is dominated by the energy term and the optimization therefore leads to low energy structures, but there is not much similarity between the experimental image and the fit, as shown in fig. 4.9 for $\omega = 0\,\text{eV}$. Conversely, when $\omega$ is large, the simulated image fits well the experimental image but the resulting cluster structure has relatively high energy and a rough surface as shown in fig. 4.9 for $\omega = 1000\,\text{eV}$.

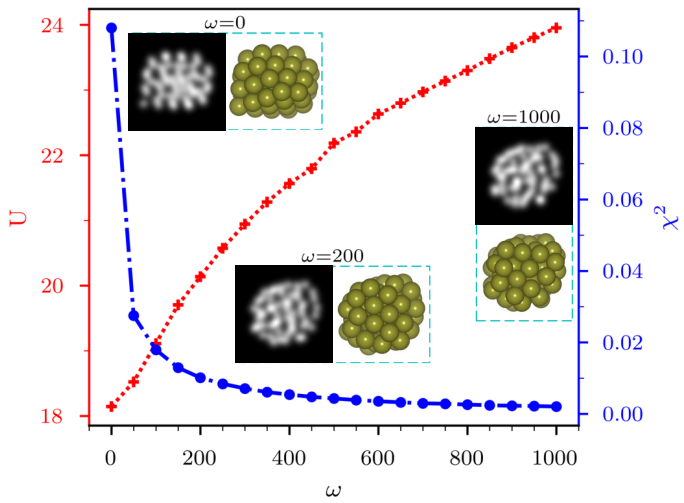


*Figure 4.9. Relationship between the energy, U, of a $Au_{55}$ cluster and the measure, $\chi^2$, of the fit to an AC-STEM image as a function of the weight parameter $\omega$ (in* eV*) in eq.* (12)*. The axis on the left and the red curve show the energy given by the EMT potential function, the axis on the right and the blue curve show the sum of squared discrepancy, $\chi^2$, between the experimental AC-STEM image (shown in fig. 4.8(a)) and a simulated image.*

Given that a value for $\omega$ ranging between 100 and 300 eV seems to give a good compromise between the image fit and the energy, the optimizations are carried out for different values within this range. Note the large discrepancy in the image generated from the lowest energy configuration obtained from the EMT potential, where the local ordering is essentially that of a face centered cubic crystal, but this approximate interatomic potential still suffices for the present purposes. Two different methods are used for the structure optimization in the second phase. The two methods give roughly the same success rate with similar computational effort and are described below.

### 4.3.1 Optimization via Saddle Point Searches

The method is based on the search for new local minima of the objective function by driving the system through regions of first order saddle points (SPs) and then sliding down towards a new local minimum on the other side of the saddle point. The method is called global optimisation using saddle traversals (GOUST) and is implemented in the EON software[57]. Detailed explanation of the method can be found in refs.[58,59].

The search starts from the structures generated in the first stage. For each system everal saddle point searches are performed by applying small random displacements to the atomic coordinates. For each of the perturbed structures, the minimum mode following method[60] is used to converge onto a saddle point. The system is then displaced along the minimum mode from the saddle point, locally minimized to slide down to the adjacent minimum. For a given local minimum, several SP searches are carried out in order to find several surrounding SPs and adjacent minima. From the list of local minima found, the one with the lowest value of the objective function is selected, and a new search for SPs is carried out. The process is repeated until the system reaches a local minimum of the objective function that is lower than any of the nearby local minima. In this way, the system is taken down a funnel on the objective function surface by hopping over energy barriers, but it does not guarantee that a global minimum has been reached.

### 4.3.2 Optimization using a Genetic Algorithm

A genetic algorithm (GA) is a search-based optimization technique based on the principles of Natural Selection. Genetic algorithms have been successfully applied to global structural optimisation of nanoclusters[33,52,61]. A GA uses mechanisms inspired by biological evolution, such as reproduction, mutation, recombination, and selection. Candidate solutions to the optimization problem play the role of individuals in a population, and the fitness function determines the quality of the solutions. In this work, a GA implemented in the Atomic Simulation Environment (ASE)[62,63] was used.

The GA evolution starts from a population of initial structures generated in the first phase. In each generation, a new structure is generated either by crossover or mutation. To maintain population diversity and guarantee the survival of the fittest, parent structures are selected with a bias towards configurations that give low values of the objective function and have been less frequently selected. During crossover, two structures are selected from the population and an offspring is produced through the pairing of the parent structures. Crossover is carried out 75% of the time using the standard cut-splice algorithm[64]. During mutation a cluster is selected and a new cluster is generated by randomly displacing the atoms in the cluster in random directions by a distance that ranges from zero to 1.5 Å. The new structure is locally relaxed using Broyden–Fletcher–Goldfarb–Shanno (BFGS)[65] to the nearest local minimum on the combined objective function and the population is updated so that it always contains the 20 best unique structures. The loop is repeated until 2000 structures have been tested.

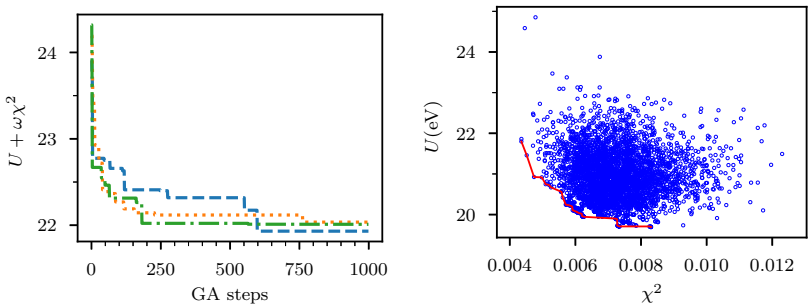


*Figure 4.10. Left: GA convergence of the best scoring candidates for three independent runs. Right: Distribution of the potential energy $U$ versus image fit $\chi^2$ for 2000 candidates tested in a GA run. The red curve represents the Pareto front, showing the objective values that give the best trade-off between the two terms.*

Figure 4.10(a) shows the convergence behavior of three independent GA runs. The curves represent the evolution of the best-scoring candidate. Figure 4.10(b) shows the energy versus image fit distribution of the obtained local minima. The red curve shows Pareto front[66]. For every point on this curve, one can improve neither of its objectives without degrading the other.

### 4.3.3 Density Functional Theory Calculations

Both GOUST and GA optimization methods provide a set of structures that have low values of the objective function and are thereby candidates for describing the atomic structure of the cluster. After performing either optimization method, selected structures are further optimized using DFT. However, to maintain a good fit to the experimental AC-STEM image, the structures are first optimized with EMT by gradually decreasing the weight $\omega$.

First, a local minimization of the objective function is carried out with a weight parameter of $\omega = 100\,\text{eV}$ regardless of the value of $\omega$ used in the optimization procedure. The optimization is repeated for smaller and smaller weight down to $\omega = 50\,\text{eV}$. At this point, the EMT part of the objective function is replaced by a DFT calculation to get a more accurate estimate of the energy, and a minimization carried out with $\omega = 50\,\text{eV}$. In this way, the energy of a cluster is gradually reduced while maintaining some level of fit to the experimental image. Finally, the contribution of the AC-STEM image in the objective function is turned off, $\omega = 0\,\text{eV}$, and the DFT energy minimized until the magnitude of the atomic forces drops below $0.01\,\text{eV}\,\text{Å}^{-1}$. Since DFT calculations involve significant computational effort, only the best 25 structures are selected for this final minimization. The relaxation is performed carefully using a small step size to ensure convergence to the nearest local minimum.

The DFT calculations are performed using the PBEsol[67] functional approximation, and a plane-wave basis set with a kinetic energy cutoff of 250 eV. The choice of this functional was motivated by recent studies that found PBEsol to be more accurate than other generalized gradient approximation (GGA) (GGA) functionals for calculating the surface energies of metal clusters.[68,69] The calculations are performed in a cubic simulation box of side length 25 Å. Gaussian smearing is used with a width of 0.1 eV. Spin polarization is not included. The Vienna ab initio simulation package (VASP)[70] is used in the DFT calculations.[70]

## 4.4 Image Comparison

Figure 4.11 shows a set of simulated images (S1-S5) for the experimental AC-STEM image shown in fig. 4.7. In almost all cases, the main features within the simulated and experimental image are in good agreement. The bright feature in the lower left region and bright ring surrounding it is well reproduced, with S4 having the best fit to the experimental image. Nevertheless, some imperfections can be seen as well, and most of the discrepancies appear to be on the right side of the obtained structures. A close comparison between S1 and the experimental image in Fig. 4.11 shows some inconsistencies in intensity distribution at the edges of the image even though the value of $\chi^2$ is relatively low, only slightly higher than for S4. The simulated image has peaks in the intensity along the edge of the image consistent with the presence of atoms. But the intensity is more diffuse in the experimental image. This diffuse appearance of the experimental image might be attributed to the enhanced thermal vibrations of surface atoms. Structural fluctuations of small gold clusters during AC-STEM image acquisition have been noted in the literature.[20,71,72].

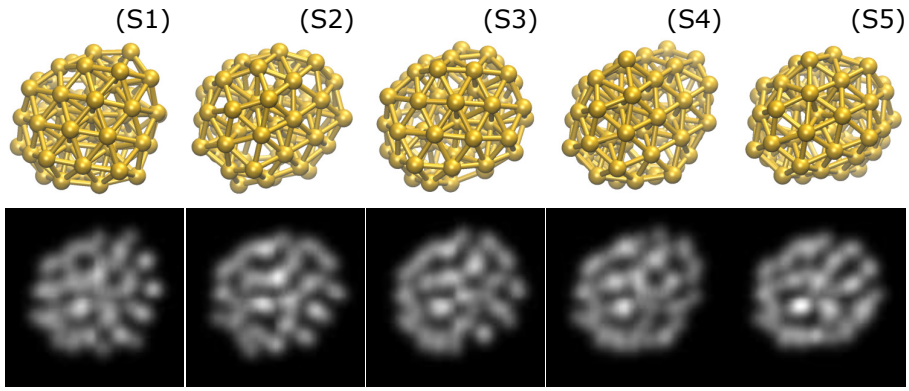


*Figure 4.11. Best fit structures and the corresponding calculated images obtained for the experimental image shown in fig. 4.8.*

## 4.5 Energy Comparison

Table 4.2 shows the relative energy of various $Au_{55}$ cluster structures obtained in the calculations. For the sake of comparison, the table also gives results for the high-symmetry $Au_{55}$ clusters such as the icosahedral, decahedral and cuboctahedral structures as well as configurations originating from energy minimization using Gupta function, EMT function and DFT based tight binding (DFTB)[73] followed by relaxation at the DFT/PBEsol level of theory. The relaxation is performed carefully using a small step size to ensure convergence to the nearest local minimum. There are only minor changes in the structures obtained with Gupta, EMT, and DFTB, and virtually no structural changes in the highly symmetry structures. As one might expect, there is a large difference in the energy of the various clusters. The optimal structure found by Garzón *et al.*[17] using the Gupta potential has the ninth highest energy of 0.51 eV above the lowest energy structure. The slightly distorted FCC-type structure predicted by the EMT potential function is much higher, 1.1 eV. The symmetric icosahedral (Ico), Ino-decahedral (Dec) and cuboctahedral (Cub) configurations are the least stable structures. The difference in the energy of the isomers found here from the fit to the AC-STEM image is less than 0.75 eV, with the exception of S4, and the energy barriers between most of them are small as shown in **??**. As mentioned above, the small energy barriers between the isomers may be overcome by thermal activation and lead to the superposition of different isomers during AC-STEM imaging. This could account for smearing of the experimental image, especially around the edges of the cluster.

*Table 4.2. Energy (*eV*) obtained with DFT/PBEsol of the $Au_{55}$ structures generated relative to the most stable one, S11.*

| Structure | $\Delta E$ | Structure | $\Delta E$ | Structure | $\Delta E$ |
|---|---|---|---|---|---|
| S11 | 0.000 | S9 | 0.322 | EMT | 1.121 |
| S10 | 0.021 | S5 | 0.415 | S4 | 1.642 |
| S2 | 0.099 | GAR | 0.514 | ICO | 1.711 |
| S7 | 0.118 | S3 | 0.681 | DEC | 2.592 |
| S6 | 0.156 | S1 | 0.713 | CUB | 3.310 |
| S8 | 0.178 | DFTB | 0.865 | | |

## 4.6 Coordination Number Analysis

The coordination numbers of the obtained clusters are presented in table 4.3. A cutoff distance of 3.4 Å is used to define neighboring (i.e. 'bonded') atoms. Most of the clusters show pronounced peaks for coordination numbers 12, 8, 7, and 6. The exception is S10, the one with lowest DFT/PBEsol energy, which has a peak at a coordination number of 11 (the same is true for the similar S11 structure). The Garzón structure differs from the clusters obtained from the AC-STEM fitting in that it has higher coordination numbers, in particular three atoms with a coordination number of 13. The lower coordination

numbers of structures obtained here by fitting the AC-STEM image, and even more so the lowest DFT/PBEsol energy structures, show that they are less compact than the Garzón structure.

*Table 4.3. Coordination numbers for the structures that give best fit to the AC-STEM image, as well as the Garzón structure and the three symmetric structures after local minimization with DFT/PBEsol.*

| | S1 | S2 | S3 | S4 | S5 | S6 | S7 | S8 | S9 | S10 | S11 | GAR | CUB | ICO | DEC |
|---|---|---|---|---|---|---|---|---|---|---|---|---|---|---|---|
| 4 | 0 | 0 | 0 | 1 | 0 | 0 | 0 | 0 | 0 | 0 | 0 | 0 | 0 | 0 | 0 |
| 5 | 0 | 6 | 2 | 3 | 5 | 4 | 2 | 3 | 3 | 5 | 5 | 1 | 12 | 0 | 10 |
| 6 | 15 | 10 | 20 | 10 | 9 | 10 | 15 | 13 | 10 | 11 | 11 | 14 | 0 | 12 | 7 |
| 7 | 12 | 20 | 12 | 15 | 15 | 15 | 10 | 13 | 22 | 16 | 17 | 12 | 24 | 0 | 10 |
| 8 | 17 | 8 | 7 | 17 | 16 | 16 | 17 | 16 | 10 | 12 | 11 | 17 | 6 | 30 | 15 |
| 9 | 1 | 3 | 4 | 0 | 1 | 1 | 1 | 1 | 2 | 3 | 3 | 1 | 0 | 0 | 0 |
| 10 | 0 | 4 | 4 | 2 | 1 | 1 | 0 | 0 | 1 | 0 | 0 | 0 | 0 | 0 | 0 |
| 11 | 3 | 1 | 3 | 1 | 1 | 2 | 2 | 3 | 4 | 5 | 6 | 3 | 0 | 0 | 0 |
| 12 | 7 | 3 | 2 | 5 | 7 | 4 | 7 | 6 | 2 | 2 | 1 | 4 | 13 | 13 | 13 |
| 13 | 0 | 0 | 1 | 1 | 0 | 2 | 1 | 0 | 1 | 1 | 1 | 3 | 0 | 0 | 0 |
| Avg | 7.9 | 7.4 | 7.6 | 7.7 | 7.8 | 7.8 | 7.9 | 7.8 | 7.6 | 7.6 | 7.6 | 8 | 7.9 | 8.5 | 8.0 |

## 4.7 Common Neighbor Analysis

The CNA method characterizes the local environment of pairs of atoms by a set of three integer indices. The first one denotes the number of atoms that are neighbors of both atoms in the pair, the second index is the total number of bonds between the common neighbors, and the third index is the number of bonds in the longest continuous chain of bonds between the common neighbors. Additional information about CNA can be found in refs [74–77].

*Table 4.4. Relative abundance of selected CNA pairs(in %) for the structures that gives the best fit to the AC-STEM image. For comparison, the CNA pairs for Garzón, icosahedron, EMT, cuboctahedron and Ino-decahedron locally minimized with DFT/PBEsol are also given. Indices with small relative abundance, such as 444, are ignored.*

| Pairs | S1 | S2 | S3 | S4 | S5 | S6 | S7 | S8 | S9 | S10 | S11 | GAR | ICO | CUB |
|---|---|---|---|---|---|---|---|---|---|---|---|---|---|---|
| 211 | 3 | 3 | 9 | 3 | 4 | 2 | 5 | 1 | 2 | 2 | 3 | 4 | – | 33 |
| 311 | 31 | 26 | 28 | 31 | 31 | 30 | 29 | 31 | 29 | 27 | 26 | 27 | 26 | 11 |
| 322 | 24 | 22 | 12 | 21 | 17 | 22 | 19 | 20 | 25 | 21 | 21 | 24 | 26 | – |
| 421 | 2 | 1 | 6 | 4 | 0 | 2 | 3 | 1 | 0 | 3 | 3 | 3 | – | 56 |
| 422 | 17 | 7 | 6 | 14 | 13 | 16 | 21 | 17 | 7 | 11 | 7 | 21 | 38 | – |
| 433 | 6 | 4 | 9 | 4 | 8 | 4 | 4 | 4 | 9 | 6 | 8 | 4 | – | – |
| 544 | 2 | 2 | 3 | 3 | 4 | 2 | 3 | 2 | 2 | 2 | 3 | 2 | – | – |
| 555 | 4 | 3 | 0 | 2 | 2 | 3 | 4 | 3 | 3 | 3 | 2 | 4 | 10 | – |

Table 4.4 shows the relative abundance of bonded pairs with the most common CNA indices for the cluster structures that give best agreement with the AC-STEM. The CNA signature can, in particular, be used to distinguish between the local ordering in a crystal, as in the cuboctahedral structure, and the non-crystallographic, five-fold symmetry icosahedral structure. A distinction between the two can be made by looking at the numbers of pairs of type 421, 422 and 555, as can be seen from the table. The main difference between these structures is that pairs of type 421 that are abundant in the cuboctahedral structure, are not present in the icosahedral structure. On the contrary, pairs of type 555 and 422, which are abundant in the 55 atom icosahedral structure, are not present in the cuboctahedral structure. The Ino-decahedral cluster has slightly more 422 pairs than 421 pairs, due to local hexagonal close pack (HCP) ordering at the stacking faults.

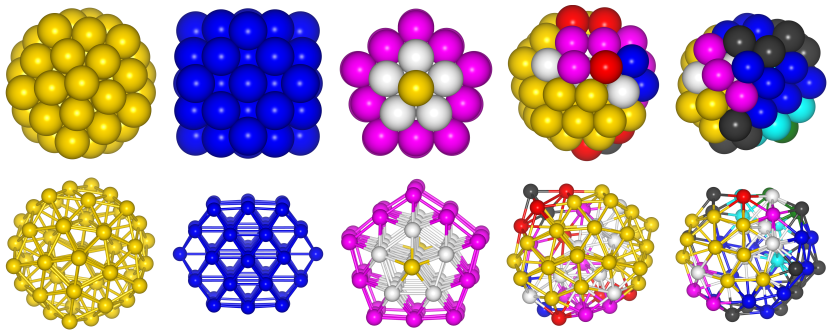

*Figure 4.12. $Au_{55}$ structures with atoms colored according to the three important CNA pairs: 421, 422 and 555. The structures from left to right are icosahedal, cuboctahedral, Ino-decahedral, the Garzón structure and S11 respectively. Blue atoms are involved in 421 pairs, yellow atoms are involved in 422 and 555 pairs, magenta atoms are involved in 421 and 422 pairs (a characteristic of local hexagonal close pack ordering, HCP). Red atoms are characteristic of local FCC ordering, where 421 pairs are formed but not 422 pairs. White atoms are involved in all three types of pairs, 421, 422 and 555 and gray atoms are not involved in any of those three.*

To illustrate the CNA analysis further, fig. 4.12 shows color-coded configurations of the icosahedral, cuboctahedral, ino-decahedral and S10 structures. Even though the S10 structure appears to be highly disordered, it presents mostly an icosahedral- like structure with just a couple of atoms containing pairs related to the local FCC ordering. Every atom in the cuboctahedral structure has at least one 421 bonded pair and no 422 or 555 pairs. Every atom in the icosahedral structure has at least one 422 and one 555 pair but no 421. In the S10 structure, the majority of atoms have at least one 422 and one 555 pair but some atoms are involved in 421 pairs. These three types of pairs, 421, 422 and 555, can be used to classify the local atomic ordering in the core of the cluster, while some of the outer shell atoms are not involved in any of these pairs but rather lower CNA index pairs.

## 4.8 Minimum Energy Path Calculations

To explore the energy landscape between the optimal structures (S1-S5), they were ordered according to the average distance between the atoms. Then, using the climbing image nudge elastic band (CI-NEB)(CI-NEB) method,[78,79] the MEP between each pair of structures was calculated using the PBEsol functional. Structures with the lowest energy in the minimum energy paths were further relaxed, leading to new local minima (S6-S11), as can be seen in fig. 4.13. A remarkable feature of the energy landscape is that adjacent local minima show large differences in the simulated images, indicating significant structural changes occur as the system hops over a single, low energy barrier. This can be observed from the CNA color-code in fig. 4.13.

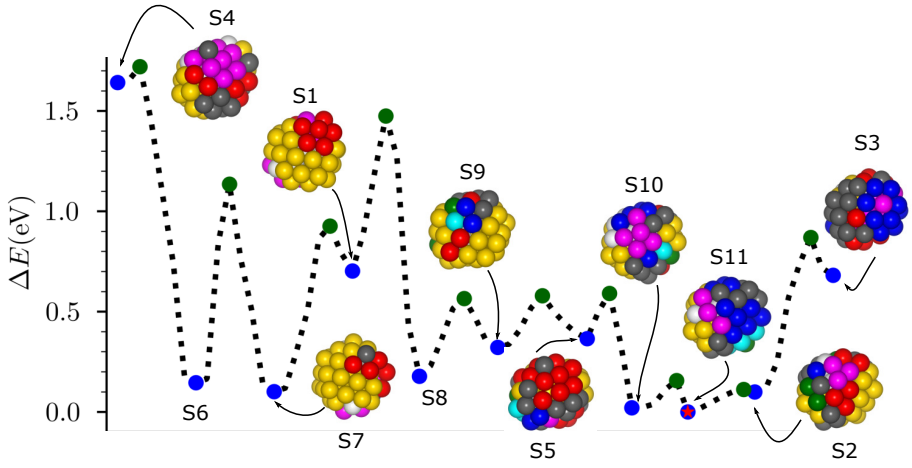


*Figure 4.13. Minimum energy path (MEP) between the five structures (S1-S5) deducted from the AC-STEM image. Each blue dot corresponds to an image in an NEB calculation and each new local minimum found in the NEB calculations has the corresponding simulated AC-STEM image of the structure below (S6-S11). For comparison, the experimental AC-STEM image is located above the graph. The same colorcode is used as in fig. 4.12*

The structural changes occur due to concerted displacement of a large number of atoms and without rotation. The RMSD between structures S5 and S8 is around 0.5 Å, and the energy required to go from S5 to S9 is 0.165 eV, which means that these kinds of fluctuations are most likely taking place during the atomic imaging process. Further analysis shows that the atoms that move the most during the transition are located almost exclusively on the right hand side of the cluster, which is where the simulated images differ the most with respect to each other and the experimental one. Here we see that the structural fluctuations observed in experiments could in fact be due to concerted change in the relative position of the atoms rather than rotation.

# 5 Image Matching using Local Features

Image matching is important in computer vision and image processing. The standard method for the recognition of nanostructures from AC-STEM images is mainly based on visual comparison with a pre-calculated catalog of simulated images over a range of orientations. While this type of analysis is in many ways good enough to distinguish ordered structures such as the cuboctahedra, icosahedra, and decahedra, these ideal structure motifs do not apply in all cases, in particular for small clusters such as $Au_{55}$ where the atomic ordering is less regular.

In recent years, some efforts have been made to develop computational methods for the analysis of AC-STEM images[52]. Most of these methods rely on minimizing the mean squared error (MSE) between the experimental image and a simulated one. The MSE is simple to calculate, but in many instances, it provides an inaccurate representation of the image's quality. This suggests the necessity for more robust, powerful, and automated analysis tools for identifying nanoparticles in a more efficient and faster way.

The method described in this chapter provides a quantitative measure that more closely corresponds to a visual assessment of image similarity. The method uses the Speeded up Robust Features (SURF) algorithm to detect points of interest, also called keypoints or features[80]. Feature detection aims to enable computers to match images by recognizing similar objects between them using a series of algorithms. The method is demonstrated on an experimentally measured AC-STEM image of $Au_{55}$ nanocluster and compared with other image similarity measures commonly used in the literature.

## 5.1 Integral Image

Much of the performance increase in SURF algorithm can be attributed to the use of an intermediate image representation known as the integral image[81]. The integral image is a technique for quickly and efficiently calculating the sum of pixels in a rectangular subregion of an image[82]. The value at any point $(k,l)$ in the integral image $I'$ is the sum of all the pixels in the input image $I$ above and to the left of $(k,l)$, inclusive.

$$I'_{kl} = \sum_{i=0}^{k} \sum_{j=0}^{l} I_{ij} \tag{15}$$

Once the integral image has been computed, evaluating the sum of intensities of the original image over any rectangular region requires exactly three operations regardless of the size of the region. If we consider a rectangle bounded by vertices $A = (i_0, j_0)$,

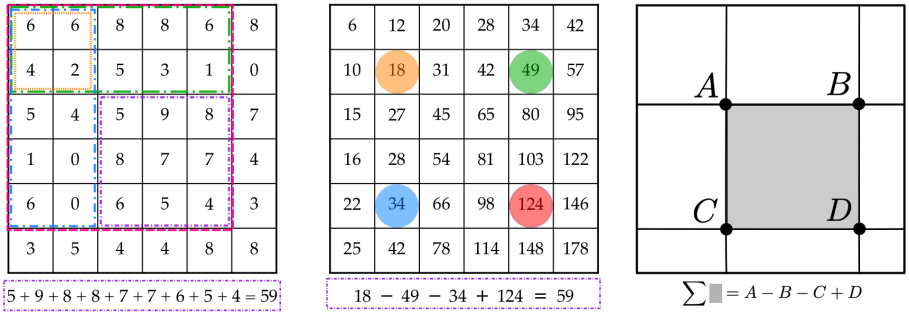


*Figure 5.14. The integral image. Left: A simple input image I with randomly generated pixel values. Center: The computed integral image $I'$. Each coloured spot in $I'$ highlights the sum inside the rectangle of that colour in I. Right: Only 3 operations and 4 memory accesses are required to calculate the sum of intensities over a rectangular region using the integral image.*

$B = (i_0, j_1)$, $C = (i_1, j_0)$ and $D = (i_1, j_1)$, as in fig. 5.14, the sum of pixel intensities is calculated by:

$$\sum_{i=i_0}^{i_1} \sum_{j=j_0}^{j_1} I_{ij} = I'_A - I'_B - I'_C + I'_D \tag{16}$$

Since computation time is independent of the size of the rectangular region, this approach is particularly useful when large areas are required. SURF makes good use of this property to perform fast convolutions of varying size box filters at constant time.

## 5.2 Hessian Detector

The SURF algorithm uses a detector based on the determinant of the Hessian matrix to find points of interest. The Hessian matrix is a square matrix of second-order partial derivatives. It describes the local curvature of a function of many variables. Given differentiable real function $f$ of two variables, the Hessian matrix $\mathcal{H}$ of $f$ at the point $(x, y)$ is:

$$\mathcal{H}(x,y) = \begin{bmatrix} f_{xx}(x,y) & f_{xy}(x,y) \\ f_{yx}(x,y) & f_{yy}(x,y) \end{bmatrix} \tag{17}$$

where $f_{xx}$, $f_{yy}$ and $f_{xy}$ are the second order partial derivatives of $f$ with respect to $x$, $y$, and $xy$. The determinant of the Hessian matrix $\mathcal{H}$ is calculated by:

$$\mathcal{D}(x,y) = det(\mathcal{H}) = f_{xx}(x,y)\ f_{yy}(x,y) - (f_{xy}(x,y))^2 \tag{18}$$

The value of the discriminant can be used to classify the maxima and minima of the function by using the second derivative test. Since the determinant is the product of

eigenvalues of the Hessian we can classify the points based on the sign of the result. If the determinant is negative then the eigenvalues have different signs and hence the point is not a local extremum; if it is positive then either both eigenvalues are positive or both are negative and in either case the point is classified as an extremum[81].

Applying the same concept to digital images rather than continuous function is a fairly straightforward task. The continuous variables $x$ and $y$ are replaced by integers and the function value $f(x,y)$ is replaced by the image pixel intensity $I(x,y)$. The second order partial derivatives of image are computed by using convolution filters. Accordingly, the four entries of the Hessian matrix $\mathcal{H}$ are calculated by convolving the image with an appropriate Gaussian kernel. Given a pixel $(x,y)$ in an image $I$, the Hessian matrix $\mathcal{H}(x,y,\sigma)$ at $(x,y)$ and scale $\sigma$ is:

$$\mathcal{H}(x,y,\sigma) = \begin{pmatrix} L_{xx}(x,y,\sigma) & L_{xy}(x,y,\sigma) \\ L_{yx}(x,y,\sigma) & L_{yy}(x,y,\sigma) \end{pmatrix}, \tag{19}$$

where $L_{xx}(x,y,\sigma)$, $L_{yy}(x,y,\sigma)$, and $L_{xy}(x,y,\sigma)$ are the convolutions of the second-order derivatives of Gaussian with the image $I$ at the point $(x,y)$. The Gaussian function in two dimensions is defined by

$$G(x,y,\sigma) = \frac{1}{2\pi\sigma^2}\, exp\left(-\frac{(x^2+y^2)}{2\sigma^2}\right). \tag{20}$$

The second-order partial derivatives of the continuous Gaussian function $G$ are calculated are calculated as:

$$G_{xx}(x,y,\sigma) = \frac{\partial^2 G}{\partial x^2}(x,y,\sigma) = \left(\frac{x^2-\sigma^2}{\sigma^4}\right) G(x,y,\sigma), \tag{21}$$

$$G_{yy}(x,y,\sigma) = \frac{\partial^2 G}{\partial y^2}(x,y,\sigma) = \left(\frac{y^2-\sigma^2}{\sigma^4}\right) G(x,y,\sigma), \tag{22}$$

$$G_{xy}(x,y,\sigma) = \frac{\partial^2 G}{\partial x \partial y}(x,y,\sigma) = \frac{xy}{\sigma^4} G(x,y,\sigma). \tag{23}$$

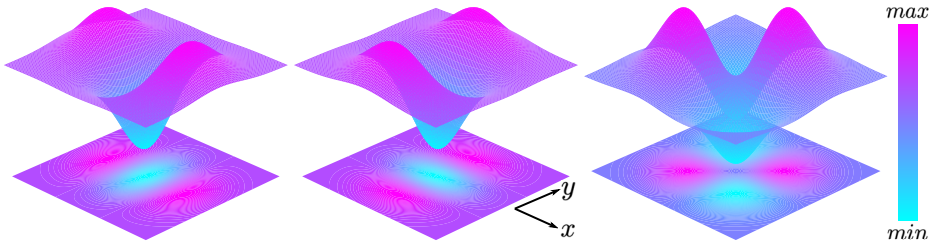


*Figure 5.15. The second order partial derivatives of the Gaussian function in the x, y and xy-directions, respectively.*

The convolution kernels are generated by sampling the continuous second-order derivative functions in a local area around the central pixel. Since images are stored as a

collection of discrete pixels, the Gaussian derivatives need to be discretised and cropped before the convolution can be performed. The second-order partial derivatives of the image are produced by convolving the discretised second-order derivative Gaussian kernels with the image.

The SURF algorithm goes a little further and approximates the convolution kernels with Box Filter. Figure 5.16 illustrates a visual comparison between between the discretised and cropped kernels and their box filter counterparts. The weights applied to each of the box filter sections are kept simple for rapid calculation using integral images. For the $D_{xx}$ and $D_{yy}$ filters, the white regions are weighted with +1 and the black regions are weighted with -1. For the $D_{xy}$ filter, the white regions are weighted with a value of +1 and the black regions with a value of -1. In all cases the gray regions are weighted with a value of 0.

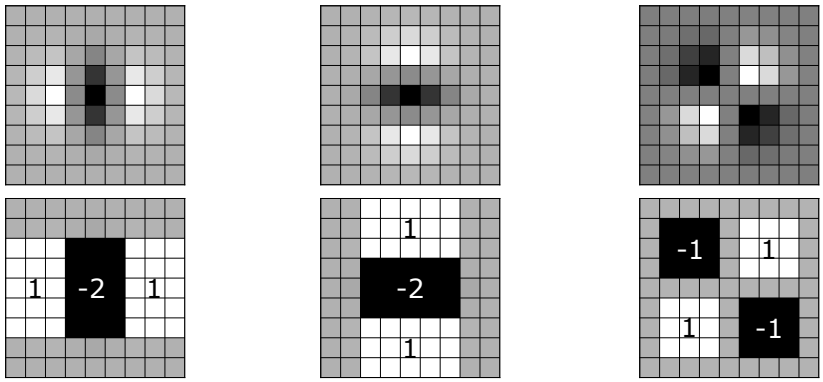


*Figure 5.16. Top: The discretised second order Gaussian derivatives in the x, y and xy-directions. Convolutions with these filters are referred to as $L_{xx}$, $L_{yy}$, $L_{xy}$. Bottom row: Corresponding box filter approximations. Convolutions with box filters are referred to as $D_{xx}$, $D_{yy}$, $D_{xy}$. The grey regions are equal to zero. Images adapted from ref.*[80]

One big advantage of using the box filter approximation is that, convolution with box filters can be easily calculated with the help of integral images[80]. Convolutions with box filters are denoted by $D_{xx}$, $D_{yy}$, and $D_{xy}$. The determinant of the Hessian matrix of the image is given by:

$$det(\mathcal{H}_{approx}(x,y,\sigma)) = D_{xx}D_{yy} - (\omega D_{xy})^2 \tag{24}$$

where the weight $\omega$ is used to balance the difference in response between the discretised Gaussian kernels and their box filter approximations.

$$\omega = \frac{|L_{xy}(1.2)|_F \; |D_{xx}(9)|_F}{|L_{xx}(1.2)|_F \; |D_{xy}(9)|_F} \; = \; 0.912 \; \approx \; 0.9, \tag{25}$$

where $|x|_F$ is the Frobenius norm. The determinant $\mathcal{H}_{approx}(x,y,\sigma)$ is referred to as the

Hessian response at location $(x,y)$ and scale $\sigma$. The maxima of the determinant of the Hessian matrix yield the interest points for an image.

## 5.3 Feature Detection

In computer vision, features (also called interest points or keypoints) refer to distinct local structures found in an image. These features typically take the form of corners, blobs, edges, junctions, or lines. Feature detection is the process of computing image information and making local decisions at every pixel to determine whether there is an image feature of a given type at that point.[83]. In the SURF approach, interest points are detected as local maxima of the determinant of Hessian operator applied to the input image. In order to detect image features using the determinant of Hessian matrix, it is first necessary to introduce the concept of a scale-space.

### 5.3.1 Scale-space Representation

The scale-space theory provides a well-founded framework for dealing with image structures. The motivation for generating a scale-space representation of a given image data originates from the basic observation that real-world objects are composed of different structures at different scales. Traditionally, the scale-space is usually realized as an image pyramid where the input image is repeatedly smoothed with a Gaussian kernel and subsequently sub-sampled in order to get the next higher level of the pyramid[84]. The scale-space in SURF is obtained by up-scaling the filter size rather than iteratively reducing the image size as illustrated in fig. 5.17.

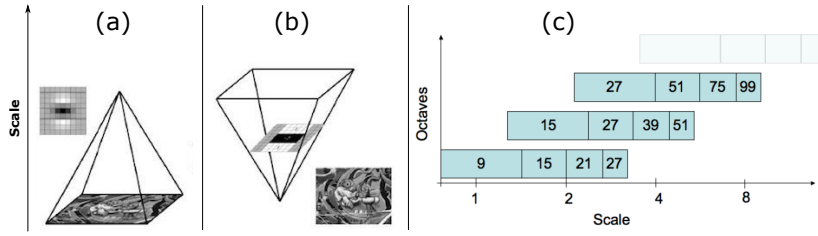


*Figure 5.17. Graphical representation of scale-space. (a) The traditional approach to constructing a scale-space. (b) The SURF approach to constructing a scale-space. The original image is kept unchanged and the filter size is varied. (c) Filter sizes for different octaves. Images taken from ref.*[80]

The scale space is divided into octaves, where an octave refers to a series of filter response maps obtained by convolving the same input image with a filter of increasing size. In SURF, the lowest level of the scale-space is obtained from the output of the $9 \times 9$ box filters, corresponding to the second-order Gaussian derivatives with $\sigma = 1.2$. Subsequent layers of the pyramid are obtained by filtering the image with gradually bigger box filters, while maintaining the same filter layout ratio. This results in filters

of size $9\times 9$, $15\times 15$, $21\times 21$, $27\times 27$, $\cdots$. The Gaussian scale associated with each filter size is approximated as:

$$\sigma_{\text{approx}} = \text{current filter size} \times \left(\frac{\text{base filter scale}}{\text{base filter size}}\right) = \frac{1.2}{9} \times \text{current filter size}. \quad (26)$$

### 5.3.2 Interest Point Localisation

The scale-space detection of the local maxima of the determinant of Hessian matrix produces too many candidate points of interest, some of which are unstable. In order to select the most salient features from the set of detected local maxima, SURF performs a detailed analysis of the features to reject the unstable ones. The task of localising the interest points can be divided into three steps.

**I. Thresholding:** First the Hessian responses are thresholded such that all values below the predetermined threshold are discard. A larger value results in fewer, but more salient interest points, whereas a smaller value results in more numerous but less salient points of interest.

**II. Non-maximal Suppression:** After thresholding, images are searched for local maxima over scale and space using non-maximal suppression. Each pixel in the scale-space is compared to its 26 neighbours, comprised of the 8 points in the current scale and the 9 pixels in each of the scales above and below. If the pixel is a local extrema, it is a potential keypoint. It basically means that the keypoint is best represented in that scale. Figure 5.18 illustrates the non-maximal suppression step.

**III. Interpolation :** The final step in localising the points involves interpolating

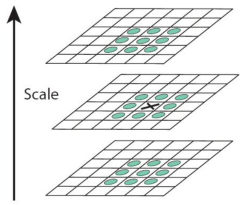


*Figure 5.18. Non-Maximal Suppression. The pixel marked 'X' is selected as a maxima if it is greater than the 8 surrounding pixels as well as the 9 pixels above and the 9 pixels below. Image taken from ref.*[80]

the nearby data to accurately determine its position in both space and scale to sub-pixel accuracy. The interpolation is done using the quadratic Taylor expansion of the determinant of the Hessian scale-space function, with the candidate keypoint at the origin[85]. The Taylor expansion is given by:

$$\mathcal{H}(\mathbf{x}) = \mathcal{H} + \frac{\partial \mathcal{H}}{\partial \mathbf{x}}^T \mathbf{x} + \frac{1}{2}\mathbf{x}^T \frac{\partial^2 \mathcal{H}}{\partial \mathbf{x}^2}\mathbf{x} \quad (27)$$

where $\mathcal{H}$ and its derivatives are evaluated at the candidate keypoint and $\mathbf{x} = (x, y, \sigma)$ is

the offset from this point. The interpolated location of the extremum, $\hat{\mathbf{x}}$, is determined by taking the derivative of this function and setting it to zero such that:

$$\hat{\mathbf{x}} = -\frac{\partial^2 \mathcal{H}^{-1}}{\partial \mathbf{x}^2} \frac{\partial \mathcal{H}}{\partial \mathbf{x}} \tag{28}$$

If the offset $\hat{\mathbf{x}}$ is larger than 0.5 in any dimension ($x$, $y$ or $\sigma$), then that's an indication that the extremum lies closer to another candidate keypoint. In this case, the candidate keypoint is changed and the interpolation performed instead about that point. This procedure is repeated until $\hat{\mathbf{x}}$ is less than 0.5 in all directions or the the number of predetermined interpolation steps has been exceeded. Those points which do not converge are dropped from the set of interest points leaving only the most stable and repeatable [86?] .

## 5.4 Feature Description

The goal of a feature descriptor is to provide a robust description of an image features by describing the intensity distribution of the pixels within the neighbourhood of the keypoint. The extraction of a SURF descriptor takes place in two steps. The first step consists of fixing a reproducible orientation based on information from a circular region around the keypoint. In the second step a square region centered at the keypoint and aligned to the selected orientation is constructed and the SURF descriptor for that keypoint is extractd from the square region.

### 5.4.1 Orientation Assignment

In order to achieve rotational invariance, each detected keypoint is assigned a reproducible orientation. To determine the orientation of a keypoint, horizontal and vertical Haar wavelet responses of size $4\sigma$ are calculated within a circular neighbourhood of radius $6\sigma$ around the keypoint, with $\sigma$ being the scale at which the interest point was detected. The specific set of pixels is determined by sampling those from within the circle using a step size of $\sigma$.

Once the wavelet responses have been calculated, they are weighted with a Gaussian centered at the keypoint. To reduce the impact of remote pixels, the responses are weighted according to their distance from the keypoint, using a discrete Gaussian kernel, with a standard deviation equal to $2.5\sigma$. The responses are then represented as vectors with the horizontal response along the abscissa and the vertical response along the ordinate. The domimant orientation is estimated by rotating a circle segment covering an angle of $60^\circ$ around the origin. At each position, the horizontal and vertical responses within the segment are summed and used to form a new vector as illustrated in fig. 5.19. The longest such vector overall defines the orientation of the keypoint.

**Upright-SURF:** For some applications, rotation invariance is not required. The orientation assignment step can therefore be omitted hence providing further performance increase. This version of SURF is referred to as Upright-SURF or U-SURF and has

been shown to maintain robustness for image rotations of up to $\pm 15^{\circ}$.[80].

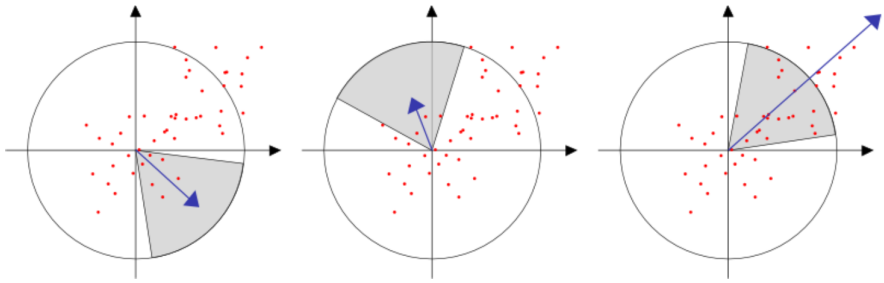

*Figure 5.19. SURF Orientation Assignment: As the circule sector of angle $\frac{\pi}{3}$ rotates around the origin the components of the responses are summed to yield the vectors shown in blue. The largest such vector determines the dominant orientation of the keypoint. Image taken from ref.*[80]

### 5.4.2 Descriptor Components

To describe the region around the point, a square window of size $20\sigma \times 20\sigma$, centered on the keypoint and oriented along the selected orientation is constructed. The square window is divided into $4 \times 4$ subregions each with side length equal to $5\sigma$. For each subregion, gradients are calculated using horizontal and vertical Haar wavelet responses of side length $2\sigma$. The gradient responses are regularly sampled, using a step length equal to $\sigma$. Hence, within each subregion gradients are calculated for 25 regularly distributed sample points. The gradient responses are weighted according to the distance of the pixel from the interest point. This processing aims at reducing the importance of distant pixels which are more sensitive to orientation or scale perturbation. It is worth noting that horizontal and vertical directions are defined in relation to the selected keypoint orientation found in section 5.4.1. If we refer to the $x$ and $y$ wavelet responses as $d_x$ and $d_y$ respectively, then a vector is formed for each subregion as:

$$v = \left(\sum d_x, \quad \sum |d_x|, \quad \sum d_y, \quad \sum |d_y|\right) \tag{29}$$

Each subregion contributes four values to the descriptor vector leading to an overall vector of length $16 \times 4 = 64$. The resulting SURF descriptor is invariant to rotation, scale, brightness and, after reduction to unit length, contrast.

**Extended SURF:** For more distinctiveness, SURF feature descriptor has an extended 128 dimension version. The sums of $d_x$ and $|d_x|$ are computed separately for $d_y < 0$ and $d_y \geq 0$. Similarly, the sums of $d_y$ and $|d_y|$ are split up according to the sign of $d_x$ , thereby doubling the number of features. There each subregion contributes 8 values to the descriptor. When represented as a vector, this gives SURF feature descriptor with total $16 \times 8 = 128$ dimensions. The extended version has been shown to provide better distinctiveness of features without adding much computation complexity.

## 5.5 Application to AC-STEM Images

In this section, the SURF algorithm is demonstrated on an experimental AC-STEM image and a set of simulated images. First, local image features or keypoints are identified. Then, a descriptor vector is generated for each keypoint, thereby providing a unique fingerprint to distinguish one keypoint from other keypoints. Finally, keypoint locations and the descriptor vectors are matched between the images using a Euclidean distance measure. The implementation of the SURF algorithm in the open-source computer vision (OpenCV)[87] library is used here. Figure 5.20 shows the experimental

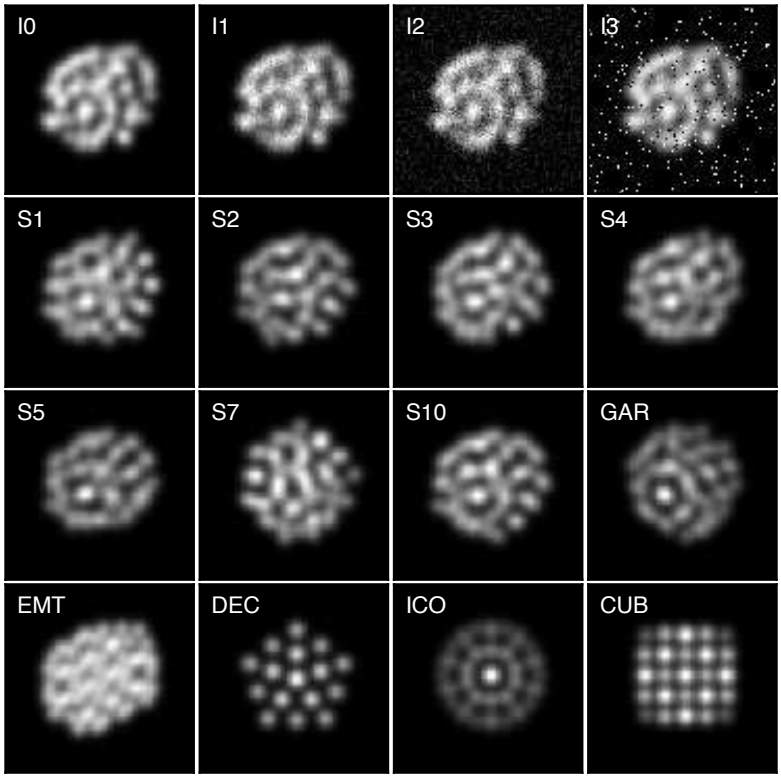


*Figure 5.20. Comparison of simulated images of $Au_{55}$ with an experimental image, I0. Images I1 - I3 are same as the experimental image but corrupted with speckle, Gaussian and salt-and-pepper noise.*

image, I0, and fifteen test images. Images I1-I3 are the same as the experimental image, but the image has been corrupted with speckle, Gaussian, and salt-and-pepper noise, respectively. Except for small changes in intensity, the corrupted images are visually similar to the original image. The Gaussian and speckle noises are sampled from the normal distribution with zero mean and standard deviation of 0.1. The salt-and-pepper noise is produced by adding random bright and dark pixels to about 10%

of the image pixels. It looks noticeably corrupted by the noise. Images S1 - S5 are simulated from atomic coordinates of $Au_{55}$ structures shown in fig. 4.11. Images GAR and EMT are generated from the global minimum structure obtained from the Gupta potential by Garzón and the global minimum structure obtained from EMT potential function, respectively. The last three images are generated from ordered $Au_{55}$ structures belonging to icosahedral, decahedral, and cuboctahedral structures. They are referred to as ICO, DEC, and CUB, respectively. They are visually different from the reference image in content, shape, and brightness and are included here to represent outliers. All the images have the same size of $160 \times 160$ pixels and the same dynamic range of 0-255.

### 5.5.1 Feature Detection

Figure 5.21 shows detected keypoints for selected images. The radius of each circle is proportional to the scale at which the keypoint is detected and its color shows the strength of the determinant of Hessian (DoH) response. In order to cope with noise and increase stability, the SURF algorithm selects the most salient features by using a threshold, $t_H$, on the response of the DoH operator. The threshold determines how large the output from the DoH operator must be in order for a point to be considered as an interest point. A larger value for $t_H$ results in fewer, but more salient keypoints, whereas a smaller value results in more keypoints, but they may be less informative. Only features whose DoH response is larger than $t_H$ are retained by the detector.

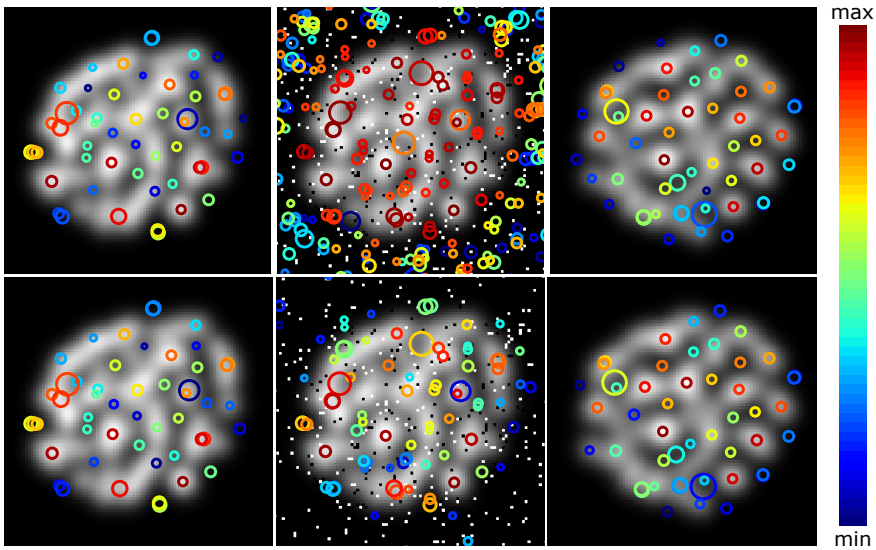


*Figure 5.21. Illustration of SURF interest point detection. Top row: 53, 408, and 54 keypoints are detected for images I0 (left), I3 (middle), and S10 (right), respectively, with $t_H = 100$. Bottom row: 50, 83 and 49 keypoints are detected for the same images with $t_H = 1000$.*

It can be observed from the salt-and-paper noise image in fig. 5.21 that most of the key points that have DoH lower than 1000 correspond to the noise pixels. Keypoints that have DoH larger than 1000 are mainly located at local intensity maxima, local intensity minima, corners, or edges of the images.

### 5.5.2 Feature Description and Matching

After keypoints have been identified and refined, a descriptor is computed for each one. To match a test image to the reference image, each feature in the reference image is compared to all features in the test image. For each keypoint in the reference image, the best three candidates with the lowest descriptor distance are chosen in the test image. The one with the smallest spatial distance is selected if it lies within 7 pixels from the reference keypoint. This matching strategy eliminates many of the false matches without significantly affecting the correct ones. Figure 2 shows examples of feature matching with and without taking into account the location of the keypoints.

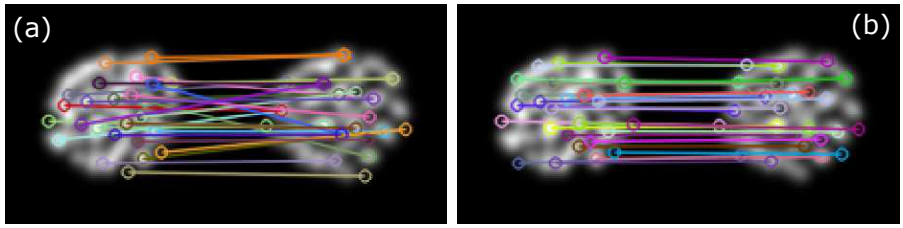


*Figure 5.22. (a) Matches obtained between I0 and S10 by comparing descriptors only. (b) Matches obtained between the same images by taking the locations of the keypoints into account.*

The feature based image distance (FBID) measure proposed here is a combination of the descriptor distances $d_s$ and spatial distance $d_p$ plus a weighted fraction of the number keypoints for which matches are not found. The new distance measure FBID is defined as

$$\text{FBID} = \sum_{i}^{Nk} (dp)_i \, (ds)_i + \gamma \frac{Nk - Nm}{Nk} \tag{30}$$

where $N_k$ represent the total number of keypoints in the reference image and $N_m$ represent the number of keypoints for which correct matches are found. The weight parameter $\gamma$ is introduced to balance the two terms of the equation. The descriptor distance $d_s$ between two descriptors $D$ and $D'$ is calculated as:

$$ds = \sqrt{\sum_{i=1}^{Nd} (D_i - D'_i)^2}, \tag{31}$$

where $Nd = 128$ denote the number of dimensions of a descriptor. The spatial distance

$d_p$ between the locations $(x,y)$ and $(x',y')$ of the two keypoints is calculated as:

$$dp = \sqrt{(x-x')^2 + (y-y')^2}, \tag{32}$$

Table 5.5 shows the various calculated measures, MSE, SSIM and the FBID, for the comparison of the 15 test images with the experimental AC-STEM image. For each measure, the images are ranked based on the calculated value, the lower value of the measure indicating a better fit. The image with the lowest value was ranked as 1 and the image with the highest valued ranked as 15. For each measure, image I0 necessarily has a value of zero since it is the reference image.

*Table 5.5. Comparison of the MSE, IMSE, SSIM and FBID measures for matching the images shown in fig. 5.20 with the experimental AC-STEM image, I0. The same image labeling as in fig. 5.20 is used here.*

| | MSE | | SSIM | | FBID | |
|---|---|---|---|---|---|---|
| Images | value | rank | value | rank | value | rank |
| I0 | 0.000 | 0 | 0.000 | 0 | 0.000 | 0 |
| I1 | 11.433 | 2 | 0.018 | 1 | 0.068 | 1 |
| I2 | 55.757 | 15 | 0.829 | 15 | 0.076 | 2 |
| I3 | 1.179 | 1 | 0.663 | 14 | 0.143 | 3 |
| S1 | 19.834 | 4 | 0.109 | 4 | 0.496 | 7 |
| S2 | 19.617 | 3 | 0.108 | 3 | 0.502 | 8 |
| S3 | 20.148 | 5 | 0.112 | 6 | 0.434 | 5 |
| S4 | 20.643 | 8 | 0.099 | 2 | 0.396 | 4 |
| S5 | 20.294 | 6 | 0.122 | 7 | 0.505 | 9 |
| S7 | 23.025 | 14 | 0.200 | 12 | 0.578 | 11 |
| S10 | 20.598 | 7 | 0.111 | 5 | 0.494 | 6 |
| GAR | 22.319 | 12 | 0.170 | 9 | 0.574 | 10 |
| EMT | 22.327 | 13 | 0.149 | 8 | 0.603 | 12 |
| ICO | 20.718 | 9 | 0.203 | 13 | 0.661 | 14 |
| DEC | 20.966 | 10 | 0.196 | 11 | 0.765 | 15 |
| CUB | 21.769 | 11 | 0.184 | 10 | 0.606 | 13 |

The values obtained for images I1-I3 test how robust the various measures are towards noise. The speckle, Gaussian and salt-and-pepper noise corrupted images are indeed found to be the first, second and third closest matches with the FBID. This is reassuring as it is consistent with the visual similarity of the noisy images with the original. The MSE measure fails to recognize the similarity of image I2 which includes Gaussian noise, and the SSIM fails to recognize both image I2 and image I3, the latter having salt-and-pepper noise. These measures are, therefore, found to be vulnerable to noise.

The results for ICO, DEC and CUB structures are interesting and particularly important, as these cluster structures are far from being optimal for $Au_{55}$ and the corresponding images are not similar to the experimental image. Nevertheless, the MSE and SSIM measures indicate a better match for these images than some of the noisy images derived from the experimental image. The MSE even gives a preference to these images over images generated from optimized $Au_{55}$ structures, such as the structure obtained with the Gupta potential function.

The lowest energy cluster structure according to the EMT potential is completely different from any of the $Au_{55}$ structures obtained with higher level theoretical methods and the image calculated from it bears no similarity to the experimental image. This is essentially a structure characteristic of the face centered cubic ordering of the crystal. Yet, the SSIM measure indicates a closer match than the Gupta structure. This shows that the SSIM measure is not reliable. The MSE measure also gives nearly the same value for the EMT structure as the Gupta structure, showing that it cannot be trusted.

The FBID measure correctly places images for EMT, ICO, DEC and CUB at the bottom of the list. It, furthermore, gives ranking to the images of low energy $Au_{55}$ structures that corresponds well with visual inspection. The image for structure S4 is deemed best and the image for S3 second best. The cluster with lowest DFT energy, S10 is identified as the third best. This is reassuring and shows that the FBID measure is providing numerical ranking that is consistent with visual inspection as well as known quality of the atomic structures of the clusters.

# 6 Conclusion and Outlook

To summarize, a method is presented for performing a systematic analysis of experimental AC-STEM images. The first phase of the method corresponds to the extraction of ($x$, $y$) coordinates of the atoms by placing a Gaussian representing the contribution of each atom to the image and assigning a $z$-coordinate using a random number generator to construct a three-dimensional structure. Local optimization of the structure is carried out after the placement of each atom using an objective function that combines pixel-by-pixel fit to the image and approximate energy function to represent the interaction between the atoms. A simple EMT energy function is used in the objective function to keep the computational cost low. Even though the lowest energy structure predicted by the EMT potential is inconsistent with the experimental image, it has turned out to be adequate as a component in the objective function. It only serves to give a rough estimate of the distance between neighboring atoms and an attraction to ensure a compact structure.

Before analyzing experimental AC-STEM images, the method is first applied to synthetic images for which the atomic structure is known. Target images are generated from regular as well as irregular isomers of $Au_{55}$ nanocluster. Given a two-dimensional synthetic image of a nancluster, the goal is to extract the three-dimensional structure of the nanocluster from the image. The method successfully extracted the positions of the atoms from the corresponding synthetic images even when a significant level of noise is added to the images.

The method is then applied to an experimental AC-STEM image of $Au_{55}$. After generating several trial structures using different random number seeds, global optimization is carried out using either GOUST or GA. Finally, the optimized structures are relaxed using electronic structure calculations based on DFT/PBEsol. The lowest energy structure found here is more stable than the icosahedral as well as the structure found by Garzó and coworkers. The CNA structural analysis performed reveals that the structures obtained can be described as “Janus” type clusters, where a part of the structure has the local icosahedral ordering of the atoms, and the other part has local order characteristic of a crystal. The latter is also manifested by a flat surface segment corresponding to a close-packed layer with ten atoms, characteristic of crystalline ordering.

The potential energy surface in the vicinity of the best fit structures is characterized by calculating the minimum energy path (MEP) connecting the local energy minima. The MEP calculation reveals several new adjacent local minima, some with lower energy and a nearly as good fit to the AC-STEM image. Transitions between neighboring structures

along the minimum energy path can, in some cases, occur readily by thermal activation and a hop over a single energy barrier typically involves concerted displacement of several atoms in the cluster. This rearrangement of the atoms can lead to considerable changes in the simulated AC-STEM images. This could shed light on the rapid structural fluctuations observed in the AC-STEM experiments. Structural fluctuations during AC-STEM imaging have been attributed to rotations of the cluster. However, from the calculations presented here, it is evident that they are more likely due to concerted displacements of several atoms that may even involve just a single energy barrier. Given that some of the calculated energy barriers between the structures are small, the corresponding transitions could be fast on the time scale of the experimental measurements, so the measured images may be a superposition of two or more structures, making a perfect fit with a single structure impossible.

A simple numerical measure for the goodness of fit generated as a sum over pixel-by-pixel squared intensity difference turns out to be useful for fine adjustments in the cluster structure. However, it does not eliminate well enough images that differ strongly from the target image. In some cases, entirely different images can give a similarly low value and falsely indicate a good match. A revised measure where the weight of bright pixels is increased fivefold is found to work better in such cases. A more robust measure for image similarity is presented. The method is based on a computer vision algorithm for determining similarity through distinct features extracted from the images. The application of the method for AC-STEM image analysis is illustrated on an experimental image of $Au_{55}$. The method successfully extracts salient features present in the AC-STEM image and matches them with similar image features in the simulated ones. However, the function describing the similarity measure is not differentiable, so it is not easy to optimize atomic structures directly from a comparison with an AC-STEM image. A practical way forward in that respect may be to develop an improved MSE by adjusting weights and penalty measures in such a way as to get an agreement with a ranking from the feature-based method for a set of test images and then use the obtained improved MSE in structure optimization.

The results obtained from the studies of the $Au_{55}$ cluster indicate that the method presented here would be useful in future AC-STEM image analysis. A software will be developed which allows systematic analysis of AC-STEM of small nanoparticles. The software can be incorporated with automatic image recognition algorithms, such as SURF and Scale-invariant Feature Transform (SIFT), to enable easier searching for a particular nanoparticle structure from a catalog of simulated images. We foresee that our approach will provide a powerful tool for the analysis of AC-STEM images, of small nanoclusters in particular, where the structures are less regular, and both the search of low energy minima and the analysis of the experimental image are especially challenging.

# Article I

**Nanocluster structure deduced from AC-STEM images coupled to theoretical modelling**

K. Sukuta, M. Van den Bossche, A. Pedersen, H. Jónsson

*Nanosystems: Physics, Chemistry, Mathematics. 8(6): 723–731*

NANOSYSTEMS: PHYSICS, CHEMISTRY, MATHEMATICS, 2017, 8 (6), P. 723–731

# Nanocluster structure deduced from AC-STEM images coupled to theoretical modelling

K. Sukuta[1], M. Van den Bossche[1], A. Pedersen[1], H. Jónsson[1,2]

[1]Science Institute and Faculty of Physical Sciences, University of Iceland, 107 Reykjavík, Iceland

[2]Center for Nonlinear Studies, Los Alamos, NM 87545, USA

hj@hi.is

**DOI 10.17586/2220-8054-2017-8-6-723-731**

Determining the atomic structure of nanoclusters is a challenging task and a critical one for understanding their chemical and physical properties. Recently, the high resolution aberration corrected scanning transmission electron microscope (AC-STEM) technique has provided valuable information about such systems, but the analysis of the experimental images has typically been qualitative rather than quantitative. A method is presented for detailed analsis of AC-STEM images combined with theoretical modelling to extract atomic coordinates. An objective function formed by a linear combination of a fit to the two-dimensional AC-STEM image plus an estimate of the cluster's energy for adding information about the third dimension is used in a global optimization algorithm to extract the atomic coordinates. The method is illustrated by analyzing model images generated for the Garzón structure of the $Au_{55}$ cluster, which is a metastable structure for the embedded atom method (EAM) potential function used here to estimate the total energy. As the method does not rely on the alignment of atom rows in the AC-STEM image, the partially disordered chiral structure of the $Au_{55}$ can successfully be determined even when a significant level of noise is added to the images.

**Keywords:** nanocluster, AC-STEM, atomic structure, global optimization, genetic algorithm.

*Received: 24 November 2017*

*Revised: 27 November 2017*

## 1. Introduction

Modern chemistry and condensed matter physics is based on knowing the atomic scale structure of the systems under study. Only after identifying the ordering of the atoms can one reliably assess the various properties such as chemical reactivity. The relationship between structure and function underpins all modern chemical intuition and understanding. Heterogeneous catalysis occurs, for example, on the surface of solids and for a long time a serious hindrance in understanding the catalytic activity was the difficulty in determining the atomic scale structure of solid surfaces. While it is relatively easy to determine atomic ordering in bulk crystals with X-ray scattering, the surface layer of atoms, which can have a significantly different atomic composition and structure than the bulk, gives a too small signal to be 'visible'. With the advent of the scanning tunneling microscope in the early 1980's [1], this problem was largely solved, and since then, there has been an explosion in the study of structure and chemical reactivity of surfaces and a great leap forward in understanding heterogeneous catalysis.

Nanoscale clusters of atoms have shown remarkable catalytic activity. With modern nanotechnology, it is possible to prepare such clusters and deposit them in a non-destructive manner on solid surfaces or into porous solids. It has, for example, been shown that CO oxidation, an important reaction for cleaning exhaust, can occur readily at below room temperature in the presence of Au nanoclusters deposited on a $TiO_2$ surface if the diameter of the clusters is in the range of 2–3 nm, corresponding to ca. $10^3$ atoms. For larger as well as smaller clusters, the catalytic activity per site drops dramatically [2]. This and similar observation on other nanocluster catalysts remain puzzling. A consensus on the reason for the strong size dependence of the catalytic activity has not been reached. In other experiments, the catalytic activity of transition metal nanoclusters has been found to depend strongly on preparation conditions and slight variations in composition [3].

A major obstacle for gaining a better understanding of nanocluster catalysis is the lack of information about the atomic structure of the clusters. While, for example, gold crystallizes in the face centered cubic (FCC) structure, small Au clusters can have very different atomic ordering by forming, for example, icosahedral or decahedral structures with fivefold symmetry (see, for example, Ref. [4]) Various theoretical calculations have addressed this problem, using mainly empirical potential functions to describe the interaction between the Au atoms, electronic density functional theory (DFT), or a combinations of both. But, it is extremely hard to search for the optimal structure of such a cluster even if it contains only ca. $10^2$ atoms. Also, it is not clear whether the current approaches to describing the atomic interactions are sufficiently accurate for these unusual systems.

An experimental technique that can provide information about the atomic scale structure of nanoclusters deposited on surfaces has been lacking until the recent development of the aberration-corrected scanning transmission electron microscope (AC-STEM). Based on ideas presented in the late 1990's [5, 6], the first such instrument was built in Daresbury in England in 2001 and several such instruments have now been set up at major universities and research laboratories. Publications describing structural determination of nanoclusters and other nanosized systems using AC-STEM have appeared in the past decade, see for example Refs. [7–12].

While the AC-STEM experimental equipment and the refinements of the measured images are highly developed, the analysis of the images in terms of atomic structure of the clusters is still often qualitative. In some cases, a catalog of calculated images based on ideal cluster structures is generated and the measured images then compared to the catalog by eye. This type of analysis is in many cases good enough to determine, for example, which one of the three main categories of structures a measured metallic cluster belongs to: FCC, icosahedra and decahedra. However, more information could be extracted from the images with a quantitative analysis tool. For example, in order to understand catalytic properties, it is important to obtain information about the atomic ordering at the surface of the cluster. The atoms at the surface of a cluster may order in a different way than would be expected from the ordering in the interior, as is well known for the surfaces of crystals.

In this article, we describe an algorithm that can be used to extract atomic coordinates from an AC-STEM image. The method is based on a two-step procedure. First, atomic coordinates in the plane of the AC-STEM image are generated. Then, the image is complemented with an estimate of the energy of the cluster to determine the three-dimensional structure. The algorithm is applied to an analysis of the $Au_{55}$ cluster. This is an interesting test case for two reasons. Firstly, Garzón and coworkers have carried out extensive studies of this cluster using the Gupta potential and shown that the structure is chiral while being highly disordered [13–15] (see Fig. 2). We will refer to this as the Garzón structure of $Au_{55}$. Experimental AC-STEM studies have supported this prediction as ca. half of the measured images were found to be consistent with the Garzón structure [16]. The other half of the images were ascribed to higher energy configurations due to thermal energy and electron beam interaction with the clusters but the atomic coordinates of those configurations were not determined. No high symmetry structures were observed. The analysis was based on image simulations using multiple scattering calculations [16].

We choose the $Au_{55}$ cluster as a demonstration for our method because it is more challenging than a structure where the atoms line up in rows. Furthermore, it is small enough that the globally optimal structure can be found without too much computational effort. Recently, a method for extracting atomic coordinates from AC-STEM images was presented, but it relies on the atoms forming rows and cannot be applied to structures such as the Garzón structure [17]. The estimate of the energy of the cluster is obtained from the embedded atom method (EAM) potential energy function [18] rather than the Gupta potential because EAM predicts a slightly different optimal structure than the Garzón structure. This choice reflects the fact that the energy of a cluster can rarely be calculated to high precision, whether the calculation is based on an empirical potential or DFT. But, when combined with an AC-STEM image the correct structure should be obtained despite errors in the energy. Fig. 1 shows a comparison of the Garzón structure and the optimal structure predicted by the EAM potential. The average difference in atomic coordinates is 0.52 Å. The Garzón structure is metastable for the EAM potential function and is 0.1 eV higher in energy than the global minimum on the EAM energy surface. Nevertheless, the method presented here for analysis of AC-STEM images is able to converge on the atomic coordinates of the Garzón structure even though it relies on an EAM energy estimate.

## 2. Methodology

The method for extracting atomic coordinates from an AC-STEM image in combination with an estimate of the cluster energy is described in this section. Instead of analyzing an experimental AC-STEM image at this stage, we use for testing and presentation purposes a simulated AC-STEM image for the Garzón structure of the $Au_{55}$ cluster. We will refer to this as the target image and it is specified by the intensity of pixels in the $x$–$y$ plane, $I_{tar}(x, y)$. Following Li *et al.*, we assume each of the $N = 55$ atoms is the source of a signal described by a Gaussian [7]:

$$I_{tar}(x, y) = \sum_{i=1}^{N} \exp\left(\frac{-(x - x_i)^2 + (y - y_i)^2}{2\sigma^2}\right), \quad (1)$$

where $x_i, y_i$ denotes coordinates of atom $i$. The width of the Gaussian, $\sigma$, is chosen to have the value 0.78 Å as was deduced by Li *et al.* from their experimental AC-STEM data on Au nanoclusters [7]. A similar value, 0.8 Å, was deduced by He *et al.* [19].

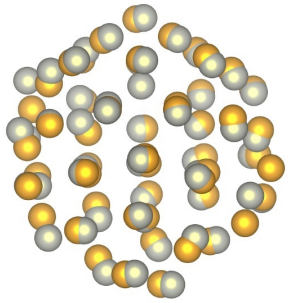

FIG. 1. Comparison of the Garzón structure (the global minimum on the Gupta energy surface) and the EAM optimal structure (the global minimum on the EAM energy surface). The Garzón structure has 0.1 eV higher energy than the EAM optimal structure when the energy is evaluated with the EAM potential. The average difference in the distance between corresponding atoms in the two structures is 0.52 Å.

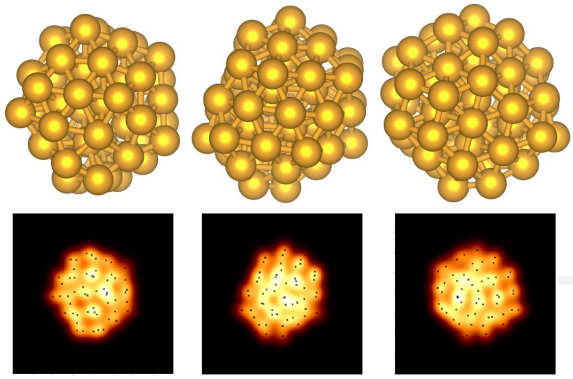

FIG. 2. Three different views of the Garzón structure of a $Au_{55}$ cluster (top), referred to as viewing angle #1, #2 and #3, and simulated AC-STEM images (bottom). The STEM images cover an area of 20 Å × 20 Å and the atomic positions are indicated as black crosses.

Simulated AC-STEM images for three different viewing angles are shown in Fig. 2. Various levels of noise are also added to the images to better emulate experimental data, as described below. The target image is normalized by summing the intensity of all pixels in the image and then dividing the intensity of each pixel with the sum.

The method for generating atomic coordinates from a target image consists of two stages. First, coordinates of the atoms in the plane of the image are generated. This will be referred to as the $x$–$y$ plane. Then, several three-dimensional structures are created by generating $z$-coordinates for the atoms and a GA optimization is performed to minimize an objective function constructed from a weighted sum of the difference between target and simulated

images plus an estimate of the potential energy of the cluster. The procedure should, in general, be repeated for different choices of the total number of atoms to find the value that gives best agreement with the target image. The procedure is described in detail in the following paragraphs.

### 2.1. Generation of $x$–$y$ coordinates

The first step is to determine $(x, y)$ coordinates for the atoms in such a way that a simulation image, $I_{sim}$, best fits a target image, $I_{tar}$ (in practice an experimentally measured AC-STEM image, but here the target image is calculated from the Garzón structure in order to have a well-defined test problem).

Each atom, $i$, located at $(x_i, y_i)$, makes a contribution to the simulated intensity at a pixel $(x, y)$ given by:

$$I_a(x, y, x_i, y_i) = \frac{1}{2N\pi\sigma^2} \exp\left(\frac{-(x - x_i)^2 + (y - y_i)^2}{2\sigma^2}\right). \tag{2}$$

The normalization is chosen in such a way that the total intensity of N atoms matches the total intensity of the target image. A reasonable estimate for the peak width $\sigma$ is required. This can be obtained by fitting the width of an isolated feature that is likely to correspond to an isolated atom, or by fitting to the width of a brighter spot corresponding to a column of atoms, if present. Atoms are assigned $(x, y)$ coordinates in the following way. The pixel with highest intensity is selected and the first atom placed at this location in the $x$–$y$ plane. Then, the contribution of this atom is subtracted from the target intensity. The second atom is placed at the maximum of the reduced target intensity, $I_{tar}(x, y) - I_a(x, y, x_1, y_1)$, etc.

After $(x, y)$ coordinates have been assigned to all $N$ atoms, they are refined by minimizing the difference between the simulated and target images:

$$S_{\text{image}} = \sum_{\text{pixels } p} D(x_p, y_p)^2, \tag{3}$$

$$D(x_p, y_p) = \left(\sum_{i=1}^{N} I_a(x_p, y_p, x_i, y_i)\right) - I_{\text{tar}}(x_p, y_p). \tag{4}$$

$S_{\text{image}}$ represents the sum over all pixels of the difference squared between the simulated and target images. The steepest descent displacement vector for each atom that reduces the discrepancy most rapidly is obtained by differentiating $S_{\text{image}}$ with respect to the atomic coordinates. For example, the $x$-component of the steepest descent vector for atom $i$ is:

$$\frac{\partial S_{\text{image}}}{\partial x_i} = \sum_{\text{pixels } p} 2\, D(x_p, y_p)\, \frac{\partial D(x_p, y_p)}{\partial x_i} \tag{5}$$

$$= \sum_{\text{pixels } p} 2\, D(x_p, y_p)\, \frac{\partial I_a(x_p, y_p, x_i, y_i)}{\partial x_i} \tag{6}$$

$$= \sum_{\text{pixels } p} 2\, D(x_p, y_p)\, I_a(x_p, y_p, x_i, y_i)\, \left(\frac{x_i - x_p}{\sigma^2}\right). \tag{7}$$

A similar expression applies to the $y$-components of the coordinates of the atoms.

### 2.2. Addition of $z$-coordinates

After $(x, y)$ coordinates have been assigned, the task is to generate a best estimate of the $z$-coordinates. As an initial estimate, $z$ coordinates are randomly chosen in such a way that the cluster is roughly spherical and no two atoms are too close together. An improved estimate is then generated by defining an objective function that includes the energy of the cluster, $E_{\text{pot}}$, plus the difference in simulated and target images. Here, an EAM potential function constructed by Foiles *et al.* [18] is used to estimate the energy of the cluster, even though it is known not to have the Garzón structure as the global minimum on the energy surface. The combined objective function, $Z$, is:

$$Z(r_1, r_2, ..., r_N) = E_{\text{pot}}(r_1, r_2, ..., r_N) + \chi\, S_{\text{image}}(r_1, r_2, ..., r_N). \tag{8}$$

The weighting factor $\chi$ is required to bring the potential energy and the image difference on a similar scale. We found it advantageous to start the local minimizations with $\chi = 0$ and to gradually increase this value to $\chi$ = 100 eV over the course of the first 50 steps in the local minimization loop.

The potential energy $E_{\text{pot}}$ of the nanocluster is estimated using the LAMMPS software [20]. This estimate does not need to be highly accurate, the most important information is in the image, but without some estimate of the optimal distance between atoms it is not possible to assign the $z$-coordinates. The gradient of the total objective

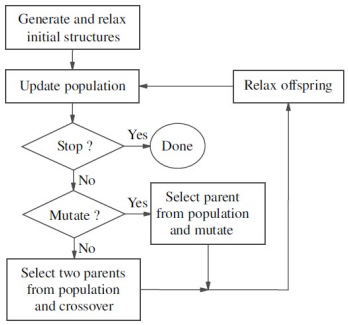


FIG. 3. Flowchart of the genetic algorithm used after a population of cluster structures consistent with the AC-STEM image have been generated.

function then consist of the negative EAM atomic force plus a $\chi$-weighted contribution from the difference in the images, $S_{\mathrm{image}}$.

The full set of coordinates of the atoms in the cluster is refined by local minimization of the objective function (Eq. 8) using the BFGS algorithm [21].

### 2.3. Genetic algorithm optimization

A global optimization of the atomic coordinates is then carried out by minimizing the objective function, Eqn. (8), using genetic algorithm (GA) tools [22] implemented in the Atomic Simulation Environment (ASE) [23, 24]. The outline of the GA used here is shown in Fig. 3. Twenty initial structures are generated as described in the previous subsection. They all have the same $x$- and $y$-coordinates for the atoms and the simulated image reproduces well the target image, but they differ in the $z$-coordinates.

The GA loop starts from a population of lowest energy structures that are also sufficiently distinct, as judged from fingerprint functions (see [25]). New structures are generated either by crossover or mutation (a 25 % mutation probability was used). The required number of parent structures are drawn from the population with a bias towards the more stable and less frequently selected structures (as in Ref. [26]). In the case of crossover, the offspring is produced through standard cut-and-splice pairing of two parent structures [27]. Single-parent mutation can occur in three different ways, as listed in Table 1. The energy of the resulting structure is subsequently minimized using the BFGS algorithm until the largest atomic force drops below $10^{-2}$ eV/Å. The minimized structure is then added to the list of candidate structures.

## 3. Results

Figure 4 shows the convergence behavior of the GA calculations for the three orientations of the Garzón structure. In all three cases, the Garzón structure is found with near 100 % success rate within 200 GA steps. On

TABLE 1. The various mutation schemes used in the GA optimization.

| Mutation | Probability | Description |
|---|---|---|
| Rattle | 60 % | Randomly displace the atoms with amplitudes uniformly sampled between 0 and 1.5 Å. |
| Match | 30 % | Force the atomic positions to the initial $(x, y)$ data set after matching using the Hungarian algorithm [28, 29]. |
| Squish | 10 % | Compress the structure along the $z$ direction. |

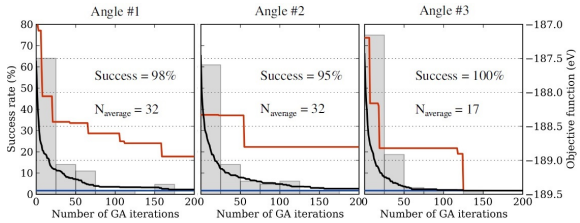


FIG. 4. Hartke graphs of the GA convergence for the three different viewing angles. The statistics are gathered on the basis of 64 independent GA runs.The gray histograms show the distribution of the required number of steps before the Garzón structure is found. The lines represent the evolution of the best-scoring candidating in the best performing (lowest curve) and worst performing (highest curve) runs and the average over the 64 runs (middle curve).

average, circa 30 GA steps are required. A small fraction of the GA runs already finds the GM within the initial population obtained after the first step and random generation of $z$-coordinates for a near spherical cluster. Such AC-STEM-assisted GA runs tend to converge at a faster rate than regular GA runs without the first step involving only the AC-STEM image fitting. When only the potential energy is used as the objective function, we find the success rate to be only 40 % after 1000 iterations, requiring circa 470 steps on average to find the global minimum on the EAM surface.

Noise is added to the target AC-STEM image by adding random numbers drawn from a Gaussian distribution $G$ centered at zero and with a standard deviation proportional to the local intensity:

$$I_{nois-tar}(x,y) = I_{tar}(x,y) + \eta, \tag{9}$$

where $\eta$ is a Gaussian random variable obtained from the probability distribution given by

$$G(\eta,\sigma_n) = \frac{1}{\sqrt{2\pi\sigma_n^2}}\, e^{-\eta^2/2\sigma_n^2}, \tag{10}$$

where $\sigma_n = \beta I_{tar}(x,y)$.

Three different noise levels were used setting the proportionality constant in the width of the Gaussian, $\beta$, to 0.1, 0.2 and 0.5, respectively. The resulting images are shown in Fig. 5. At the highest noise level, $\beta = 0.5$, some pixels acquire negative intensities. The added noise is then adequately reduced by subsequent Wiener filtering [30]. The images obtained after such filtering are also shown in Fig. 5. as well as convergence graphs for GA calculations employing the filtered images. When comparing to the data in Fig. 4, it can be concluded that using the noisy but filtered images in the GA optimization only slightly increases the number of steps required to reach convergence. The bottom panel in Fig. 5 confirms that the GM structures obtained using the filtered images agree closely with the reference Garzón structure. This indicates that the method is robust with respect to the presence of noise in the AC-STEM images.

We have also performed tests where the target image is generated from a structure that has been perturbed from the Garzón structure by adding random displacements in the $x$ and $y$ positions, drawn from a uniform distribution $[0,\alpha[$. Such tests effectively correspond to evaluating the relative difficulty of finding an optimal structure which is not close to a local minimum structure of the potential energy surface. The convergence data obtained for maximal displacements of $\alpha = 0.2$ Å, 0.5 Å and 1.0 Å are shown in Fig. 6. It can be noted that the convergence speed is reduced, but that fair success rates are still achieved even at the large maximal displacement of 1.0 Å. The corresponding atomic displacements and changes in the simulated AC-STEM image are illustrated in Fig. 6. We conclude from these tests that it is advisable (though not critically important) to use sufficiently accurate representations of the potential energy surface, such that the real structure is not too distant from a local minimum on the potential energy surface.

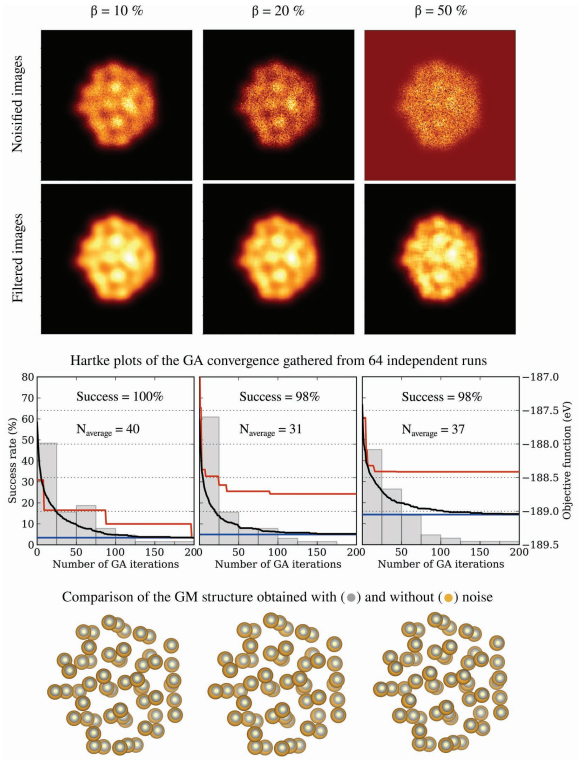


FIG. 5. Top: simulated STEM images with added noise levels (top row) and the corresponding images after Wiener filtering (second row). Center: Hartke graphs showing the convergence of the corresponding GA calculations (bars and lines as in Fig. 4). Bottom: 2-dimensional projections of the Garzón structure (gold) and of the results of the GA calculations with the various noise levels (gray). The latter have been displaced towards the viewer by 0.8 Å to make it easier to compare the positions in the $x$–$y$ plane.

## 4. Discussion

The method presented here for the extraction of atomic coordinates from AC-STEM images supplemented by a method for estimating the cluster energy does not rely on the presence of distinct atomic rows in the AC-STEM image. This is in contrast to the approach by Yu *et al.* [17], where such rows are employed to create the initial population and to apply specific mutations. A second major difference is that we consistently use the total

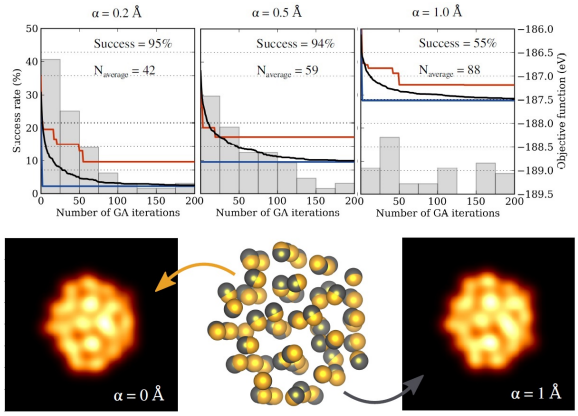


FIG. 6. Top panel: Hartke graphs showing the GA convergence for the three different maximal perturbations from the Garzón structure, $\alpha$, in the generation of the target image. The histogram and lines are of the same kind as in Fig. 4. Bottom panel, center: Overlay of the structural models of the unperturbed (lighter coloured) and the most strongly perturbed structure ($\alpha = 1.0$ Å) (darker coloured). The atomic radii are 1.5 Å, for comparison. Bottom panel, left and right: simulated AC-STEM images for the unperturbed Garzón structure and most strongly perturbed structure.

objective function (Eq. 8) throughout the GA run. Yu and coworkers minimize the potential energy during the local optimization and add the image discrepancy term only as a single-point correction after the optimization.

The tests presented here show that it is possible to successfully use an objective function including both the potential energy and an image discrepancy term, even when the experimental AC-STEM image is affected by large noise. The method can be applied to studies of disordered clusters. It should also be able to identify whether the atoms at the surface of the cluster are ordered in a different way than the atoms in the interior, an important aspect for the study of catalytic properties.

## 5. Acknowledgements

We thank Ignacio Garzón for providing us with the atomic coordinates in the optimal $Au_{55}$ structure deduced from the Gupta potential function. This work was supported by the Icelandic Research Fund and the University of Iceland Doctoral Fund. KS and MVDB gratefully acknowledge computer resources at the University of Iceland Computing Services (Reiknistofnun) and through a SNIC grant at C3SE (Göteborg, Sweden).

## References

[1] Binning G., Rohrer H., Gerber Ch., Weibel E. Surface studies by scanning tunneling microscopy. *Phys. Rev. Letters*, 1982, **49**(1), P. 57–61.
[2] Valden M., Lai X., Goodman D.W. Onset of catalytic activity of gold clusters on titania with the appearance of nonmetallic properties. *Science*, 1998, **281**, P. 1647.
[3] Yamauchi M., Abe R., Tsukuda T., Kato K., Takata M. Highly selective ammonia synthesis from nitrate with photocatalytically generated hydrogen on CuPd/$TiO_2$. *J. Am. Chem. Soc.*, 2011, **133**(5), P. 1150–1152.
[4] Li H., Li L., Pedersen A., Gao Y., Khetrapal N., Jónsson H., Zeng X.C. Magic-number gold nanoclusters with diameter 1 to 3.5 nm: Relative stability and catalytic activity for CO oxidation. *Nano Letters*, 2015, **15**, P. 682.
[5] Brown L.M. A Synchrotron in a Microscope. *Institute of Physics Conference Series*, 1997, **153**, P. 22.
[6] Krivanek O.L., Dellby N., Lupini A.R. Towards sub-Å electron beams. *Ultramicroscopy*, 1999, **78**(1-4), P. 1–11.
[7] Li Z.Y. *al.* Three-dimensional atomic-scale structure of size-selected gold nanoclusters. *Nature*, 2007, **451**(7174), P. 46–48.
[8] W Zhou W., Ross-Medgaarden E.I., Knowles W.V., Wong M. S., Wachs I.E., Kiely C.J., *Nature Chemistry*, 2009, **1**, P. 722.

[9] Van Aert S., Batenburg K.J., Rossell M.D., Erni R., Van Tendeloo G. Three-dimensional atomic imaging of crystalline nanoparticles. *Nature*, 2011, **470**, P. 374.
[10] Bals S., Van Aert S., Romero C.P., Lauwaet K., Van Bael M.J., Schoeters B., Partoens B., Yücelen E., Lievens P., Van Tendeloo G., Atomic scale dynamics of ultrasmall germanium clusters. *Nature Communications*, 2012, **3**, P. 897.
[11] Liu J., Single atom and cluster catalysis: The era of aberration-corrected scanning transmission electron microscopy. *Microscopy and Microanalysis*, 2013, **19** (Suppl. 2), P. 1678.
[12] Corma A. *et al.*, Exceptional oxidation activity with size-controlled supported gold clusters of low atomicity. *Nature Chemistry*, 2013, **5**, P. 775.
[13] Garzón I.L., Posada-Amarillas A. Structural and vibrational analysis of amorphous $Au_{55}$ clusters. *Phys. Rev. B*, 1996, **54**, P. 11796–11802.
[14] Garzón I.L. *et al.* Lowest Energy Structures of Gold Nanoclusters. *Phys. Rev. Letters*, 1998, **81**, P. 1600–1603.
[15] Michaelian K., Rendón N., Garzón I.L. Structure and energetics of Ni, Ag, and Au nanoclusters. *Phys. Rev. B*, 1999, **60**(3), P. 2000–2010.
[16] Wang Z.W., Palmer R.E. Experimental evidence for fluctuating, chiral-type $Au_{55}$ clusters by direct atomic imaging. *Nanoletters*, 2012, **12**, P. 5510–5514.
[17] Yu M., Yankovich A.B., Kaczmarowski A., Morgan D., Voyles P.M. Integrated computational and experimental structure refinement for nanoparticles. *ACS Nano*, 2016, **10**(4), P. 4031–4038.
[18] Foiles S.M., Baskes M.I., Daw M.S. Embedded-atom-method functions for the fcc metals Cu, Ag, Au, Ni, Pd, Pt, and their alloys. *Phys. Rev. B*, 1986, **33**(12), P. 7983–7991.
[19] He D.S., Li Z.Y., Yuan J. Kinematic HAADF-STEM image simulation of small nanoparticles. *Micron*, 2015, **74**(C), P. 47–53.
[20] Plimpton S. Fast parallel algorithms for short-range molecular dynamics. *J. Comput. Phys.*, 1995, **117**(1), P. 1–19.
[21] Head J.D., Zerner M.C. A Broyden-Fletcher-Goldfarb-Shanno optimization procedure for molecular geometries. *Chem. Phys. Lett.*, 1985, **122**(3), P. 264–270.
[22] Vilhelmsen L.B., Hammer B. Systematic study of $Au_6$ to $Au_{12}$ gold clusters on MgO(100) F centers using density-functional theory. *Phys. Rev. Lett.*, 2012, **108**(12), P. 126101(4 pp.).
[23] Bahn S.R., Jacobsen K.W. An object-oriented scripting interface to a legacy electronic structure code. *Comput. Sci. Eng.*, 2002, **4**(3), P. 56–66.
[24] Larsen A.H., *et al.* The atomic simulation environment a Python library for working with atoms. *J. Phys.: Condens. Matter*, 2017, **29**(27), P. 273002.
[25] Lyakhov A.O., Oganov A.R., Stokes H.T., Zhu Q. New developments in evolutionary structure prediction algorithm USPEX. *Comput. Phys. Commun.*, 2013, **184**(4), P. 1172–1182.
[26] Vilhelmsen L.B., Walton K.S., and Sholl D.S., Structure and mobility of metal clusters in MOFs: Au, Pd, and AuPd clusters in MOF-74. *J. Am. Chem. Soc.*, 2012, **134**(30), P. 12807–12816.
[27] Daven D.M., Tit N., Morris J. R., Ho K.M. Structural optimization of Lennard-Jones clusters by a genetic algorithm. *Chem. Phys. Lett.*, 1996, **256**(12), P. 195–200.
[28] Kuhn H.W. The Hungarian method for the assignment problem. *Naval Research Logistics*, 1955, **2**(1-2), P. 83–97.
[29] Munkres J. Algorithms for the assignment and transportation problems. *J. Soc. Ind. Appl. Math.*, 1957, **5**(1), P. 32–38.
[30] Kilaas R. Optimal and near-optimal filters in high-resolution electron microscopy. *J. Microsc.*, 1998, **190**(1-2), P. 45–51.

# Article II

**From AC-STEM Image to 3D Structure: A Systematic Analysis of $Au_{55}$ Nanocluster**

Kusse S. Bersha, Alejandro Peña-Torres, Hannes Jónsson

*Submitted to J. Chem. Theory Comput.*

# From AC-STEM Image to 3D Structure: A Systematic Analysis of $Au_{55}$ nanocluster

Kusse S. Bersha,[†] Alejandro Peña-Torres,[†] and Hannes Jónsson[*,‡,¶]

†*Science Institute of the University of Iceland, 107 Reykjavík, Iceland*
‡*Faculty of Physical Sciences, University of Iceland, 107 Reykjavík, Iceland*
¶*Department of Applied Physics, Aalto University, FI-00076 Espoo, Finland*

E-mail: hj@hi.is

## Abstract

Aberration-corrected scanning electron microscopy (AC-STEM) can provide valuable information on the atomic structure of nanoclusters, an essential input for gaining an understanding of their physical and chemical properties. A systematic method is presented here for the extraction of atom coordinates from an AC-STEM image in a way that is general enough to be applicable to irregular structures. The two-dimensional information from the image is complemented with an approximate description of the atomic interactions so as to construct a three-dimensional structure and, at a final stage, the structure is refined using electron density functional theory (DFT) calculations. The method is applied to an AC-STEM image of $Au_{55}$. Analysis of the local structure shows that the cluster is a combination of a part with icosahedral structure elements and a part with local atomic arrangement characteristic of crystal packing, including a segment of a flat surface facet. The energy landscape of the cluster is explored in calculations of minimum energy paths between the optimal fit structure and other candidates generated in the analysis. This reveals low energy barriers for conformational changes, showing that such transitions can occur on laboratory timescale even at room temperature and lead to large changes in the AC-STEM image. The paths furthermore reveal additional cluster configurations, some with lower DFT energy and providing nearly as good fit to the experimental image.

## Keywords

Nanocluster, gold, optimization, atomic structure, electron microscopy

In the past few decades, the study of small metallic nano-clusters has been an active field of research, in part as a result of the numerous applications in optoelectronics, magnetism and catalysis.[1–3] Knowledge of the atomic scale structure is a prerequisite for gaining a clear understanding of cluster properties, as is the case for any form of matter, and can help to identify possible future applications. Experimental studies of the atomic scale structure of nanoclusters have, however, been hampered by lack of appropriate tools. The aberration-corrected scanning transmission electron microscope (AC-STEM) technique[4,5] has recently become a powerful tool for gaining information about the structure of nanoclusters and has thereby opened up new territory in nanocluster research.[6–8] The information extracted from AC-STEM images has, however, so far mainly been qualitative and analysis techniques are needed for systematic, quantitative structural determination.

A great deal of AC-STEM measurements have been dedicated to the study of gold nanoclusters. The analysis of the experimental images has mainly involved visual comparison with pre-calculated images for the three regular structure motifs, *i.e.* decahedral, icosahedral and cuboctahedral geometries.[6,9–13] While the basic structure of many clusters has been identified using this technique, there are also clusters, such as $Au_{55}$, where the structure does not fit any of the standard motifs. This is likely also going to be the case for many multicomponent clusters. Wang and Palmer[14] carried out an extensive study of $Au_{55}$, and could relate about half the images obtained to a prediction made earlier by Garzón *et al.*[15,16] based on simulations using an empirical potential function.

While the generation of an AC-STEM image from an assumed structure is typically carried out using electron scattering calculations,[17] Li *et al.*[6] have shown that the intensity in experimental images of $Au_n$ clusters with $n \leq 1500$ increases nearly linearly with the number of atoms. Furthermore, they showed that images generated from electron scattering calculations can be reproduced to good approximation with a simple superposition of a Gaussian-like contribution from each atom in the cluster. This simplifies greatly the simulation of an AC-STEM image from an assumed atomic structure. For a given model for the structure, an approximate simulation of an AC-STEM image for a Au cluster is, therefore, quite simple.

Finding the stable, low energy structures of a nanocluster theoretically is, however, a significant challenge. The number of local minima on the energy surface is typically large and an exhaustive exploration is not practical even for relatively small clusters.[18–20] While it may be easy to find some low lying minima, the search for the global minimum may be impossible and it is difficult to know whether it has been found or remains to be seen. This even applies to calculations using simple, empirical potential functions, which have limited predictive power (as demonstrated below, but for which the pioneering work of Garzón *et al.*on $Au_{55}$ is a notable exemption), while the more accurate, but still typically approximate electronic structure calculations, are limited to even smaller clusters and less exploration.

Several studies have made use of genetic algorithms (GAs) or other optimization algorithms combined with empirical potential functions or electronic structure calculations in order to obtain structures of nanoclusters.[21–26] A method tailored to analysis of AC-STEM data in particular has been presented by Yu *et al.*[27] who applied it to a model of a large Au nanoparticle (∼6000 atoms). For such large clusters, the local ordering of the atoms is the same as in the crystal and the analysis can be simplified in terms of positions and intensities of columns and rows of atoms, as well as surface facets. However, the structure of smaller Au clusters can be less regular, increasing the difficulty of both the search of low energy minima and the analysis of the experimental image. In fact, it has been shown recently that the common notion of magic clusters, *i.e.* cluster that are particularly stable because they correspond to shell closings of the ideal structure motifs, does not hold for Au clusters in the range of 100 to 2000 atoms.[28]

In this work, a method is presented for the analysis of AC-STEM images that is applicable in general, to disordered as well as ordered clusters. An AC-STEM image of a $Au_{55}$ cluster reported by Wang and Palmer[14] is analyzed using a two phase optimization method based on an objective function that includes the discrepancy between a simulated and the experimental image as well as an approximate estimate of the energy of the cluster. In this way, several three-dimensional structures of $Au_{55}$ are generated and finally optimized using DFT calculations. Additionally, the minimum energy path between the various structural candidates is calculated using DFT to explore further the potential energy surface of the system, thereby revealing new local minima on the energy surface and identifying facile transitions between structures. A brief account of a preliminary version of the analysis method has been published previously.[29]

## Generation of structures from an AC-STEM image

Using the results obtained by Li *et al.*[6] showing that an AC-STEM image of a Au cluster can be approximated by a superposition of Gaussians, the intensity at a given pixel can be described as a linear combination of intensity contributions from each of the atoms in the cluster. Thus the intensity at pixel $(i, j)$ can be written as

$$I_{ij}(\boldsymbol{x},\boldsymbol{y},\sigma)=\sum_{k=1}^{N}\mathcal{A}\exp\left(-\frac{\left(x_i'-x_k\right)^2+\left(y_j'-y_k\right)^2}{2\sigma^2}\right), \quad (1)$$

where $N$ is the number of atoms in the cluster with coordinates $\boldsymbol{x}=(x_1,\cdots,x_N)$ and $\boldsymbol{y}=(y_1,\cdots,y_N)$ projected on a plane parallel to the image, $x'$ and $y'$ are the spatial coordinates corresponding to the pixels of the image, and $\sigma$ and $\mathcal{A}$ are the width and height of the Gaussian peaks. The parameter $\mathcal{A}$ is obtained by matching the integrated intensity of $N$ atoms to the integrated intensity of the experimental image

$$\mathcal{A}=\frac{1}{2\pi\sigma^2R^2N}\sum_{i=1}^{m}\sum_{j=1}^{n}I'_{ij}, \quad (2)$$

where $I'$ is the experimental image, $m$ and $n$ give the number of rows and columns of pixels in the image and $R$ is the resolution of the image in pixels/Å. The unknown parameters of the model are the atom coordinates and the width ($\sigma$) of the Gaussians. These are estimated by fitting the simulated image to the AC-STEM image.

A simple measure of the agreement between a simulated image and an experimental image can be obtained as a sum over the squared difference between the measured ($I'$) and calculated ($I$) intensity at each pixel

$$\chi^2(\boldsymbol{x},\boldsymbol{y},\sigma)=\sum_{i=1}^{m}\sum_{j=1}^{n}\left(I'_{ij}-I_{ij}(\boldsymbol{x},\boldsymbol{y},\sigma)\right)^2. \quad (3)$$

The displacement of the atoms in the model that reduces the discrepancy between the images most rapidly can be found analytically by differentiating $\chi^2$, see the *Methods* section. With this analytical gradient, the structure optimization can be made more efficient. The simple $\chi^2$ measure turns out, however, to be less than optimal, as shown below.

At this level of approximation, the AC-STEM image does not give any information about the $z$-coordinate of the atoms. Therefore, an objective function that also includes the energy of the cluster is included to complement the fit to the image. An objective function is thus defined as the weighted sum of the pixel-by-pixel discrepancy and the estimate of the energy of the cluster as

$$f(\boldsymbol{x},\boldsymbol{y},\boldsymbol{z},\sigma)=\omega\chi^2(\boldsymbol{x},\boldsymbol{y},\sigma)+U(\boldsymbol{x},\boldsymbol{y},\boldsymbol{z}), \quad (4)$$

where $\boldsymbol{z}=(z_1,\cdots,z_N)$ corresponds to the $z$-coordinates of the atoms, $U$ is the estimated energy of the cluster and $\omega$ is a weight parameter used to control the relative importance of the two contributions. The gradient of this combined objective function then consist of the gradient of the energy (negative of the atomic force) plus a weighted contribution from the gradient of $\chi^2$. Setting $\omega=0$ during optimization results in pure energy minimization and identifies a low energy structure but not a fit to the AC-STEM image. On the other hand, setting $\omega$ to a large value results in pure image fitting providing two-dimensional images that fit the experimental image well, but likely correspond to a high energy structure. Therefore, by choosing an intermediate value for the weight, a compromise between image fitting and energy is struck. The energy is estimated here using the effective medium theory (EMT) potential function,[30] which works well in the present context even though the lowest energy structure found for $Au_{55}$, is predicted to be entirely different from the estimate obtained from the analysis of the AC-STEM image, as shown below. It is important that the method does not require a highly accurate estimate of the energy, as it mainly serves to control the nearest neighbor distance between the atoms and to provide interatomic attraction to ensure that a compact cluster model is generated.

The method for generating the atomic coordinates of the nanocluster consists of two

phases. The first phase starts out by locating local intensity maxima in the AC-STEM image. The first atom in the model is then placed at the location of the highest maximum and its $z$-coordinate is arbitrarily given a value of $z = 0$. The intensity contribution of this atom is then subtracted from the experimental image and a second atom is placed at the location of the maximum in the reduced image. The $z$-coordinate of the second atom, and all subsequent atoms, is generated randomly between $-10$ Å and 10 Å while ensuring a minimal interatomic distance of 2.8 Å. A local minimization of the combined objective function is performed with a weight of $\omega = 1000$ eV after the placement of each atom. This process is continued until the coordinates of a predefined number, $N$, of atoms has been assigned. By repeating this process with different random number seeds, several three-dimensional atomic structures are generated with $(x, y)$ coordinates that almost perfectly fit the AC-STEM image, but have relatively high energy and are slightly elongated in the $z$-direction. They serve as input for a structure optimization procedure in the second phase. It should be noted that from the fitting procedure in the first phase, an estimate for the width ($\sigma$) of the Gaussians is obtained. This value is kept fixed during the optimization of the structures in the second phase. Figure 1 shows a comparison between the experimental image (inset *a*) and an image obtained by the fitting process described above (inset *b*). Horizontal line scans illustrate the excellent agreement with respect to both the peak positions and the relative peak intensities.

## Optimization of the structures

An optimization of the atomic coordinates of the cluster generated in the first phase is carried out by minimizing the combined objective function given by eq 4 with a smaller value of the weight on the image, $\omega$. In order to get a good compromise between the information from the AC-STEM image and the energy estimate, a suitable value of $\omega$ needs to be determined.

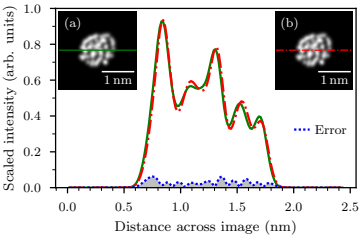


Figure 1: (a) Experimental AC-STEM from ref.[14] and (b) simulated image of a $Au_{55}$ cluster after the first phase of the fitting procedure, as well as line scans of the intensity (green for experimental and broken red for simulated). At this point the energy of the cluster is high as the $z$-coordinate of the atoms has not been optimized, except for local minimization. The difference between the two intensity profiles is shown by the blue dotted curve.

Figure 2 shows the relationship between image fit and cluster energy for different values of the weight parameter. When $\omega$ is small, the objective function is dominated by the energy term and the optimization therefore leads to low energy structures, but there is not much similarity between the experimental image and the fit, as shown in Figure 2 for $\omega = 0$ eV. Conversely, when $\omega$ is large, the simulated image fits well the experimental image but the resulting cluster structure has relatively high energy and a rough surface as shown in Figure 2 for $\omega = 1000$ eV.

We have used two different methods in the structure optimization in the second phase. Given that a value for $\omega$ ranging between 100 and 300 eV seems to give a good compromise between the image fit and the energy, the optimizations are carried out for different values within this range. The two methods used give roughly the same success rate with similar computational effort and are briefly described below, but more details can be found in the *Methods* section.

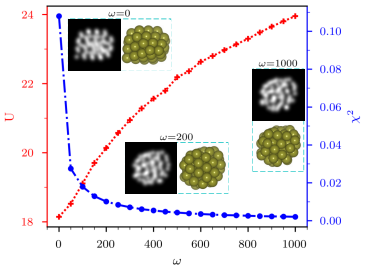


Figure 2: Relationship between the energy, $U$, of a $Au_{55}$ cluster and the measure, $\chi^2$, of the fit to an AC-STEM image as a function of the weight parameter $\omega$ (in eV) in Eq. 4. The axis on the left and the red curve show the energy given by the EMT potential function, the axis on the right and the blue curve show the sum of squared discrepancy, $\chi^2$, between the experimental AC-STEM image (shown in figure 1(a)) and a simulated image. Note the large discrepancy in the image generated from the lowest energy configuration obtained from the EMT potential, where the local ordering is essentially that of a face centered cubic crystal, but this approximate interatomic potential still suffices for the present purposes.

### A. Optimization via saddle point searches

This method is based on finding a new local minimum on the objective function surface by driving the system through regions of first order saddle points and then sliding down on the other side. The method has been referred to as global optimization using saddle traversals (GOUST).[31] For every cluster structure obtained in the first stage, multiple saddle point searches are performed. The minimum mode following method is used to converge onto the saddle points.[32,33] Afterwards, a displacement of the system along the minimum mode at the saddle point is carried out, followed by minimization to slide down to the adjacent minimum. In this way, the system heads down a funnel in the combined objective function surface, by hopping over barriers, until a minimum with the lowest value compared to nearby local minima has been reached.

### B. Optimization using a genetic algorithm

Alternatively, a genetic algorithm (GA) is used, as is commonly done in nanocluster simulations.[27,34–37] New structures are generated from parent structures by crossover and mutations. To maintain population diversity and guarantee the survival of the fittest, parent structures are selected with a bias towards configurations that give low values of the objective function and have been less frequently selected.

Both of these optimization methods provide a set of structures that have low values of the objective function and are thereby candidates for describing the atomic structure of the cluster. After the GOUST or GA optimization, a local minimization of the objective function is carried out with a weight parameter of $\omega = 100$ eV (regardless of the value of $\omega$ used in the optimization procedure). This is repeated for smaller and smaller weight down to $\omega = 50$ eV. In this way, the energy of a cluster is gradually reduced while maintaining some level of a fit to the experimental AC-STEM image. At this point, the EMT paart of the objective function is replaced by a DFT calculation using the PBEsol functional to get a more accurate estimate of the energy and a minimization carried out with $\omega = 50$. Since DFT calculations involve significant computational effort, only the best 25 structures were selected for this final minimization. Finally, the contribution of the AC-STEM image in the objective function is turned off, $\omega = 0$ eV, and the DFT energy minimized until the magnitude of the atomic forces drops below 0.01 eV Å$^{-1}$.

## Results and Discussion

Figure 3 shows a set of simulated images (labeled $S1-S5$) obtained by fitting an AC-STEM image reported by Wang and Palmer.[14] The $\chi^2$ value shows the sum of squared pixel in-

tensity differences between the simulated image and the experimental one, as defined by Eq. 3. In most cases, the main features of the experimental image are reproduced, in particular the bright feature in the lower left region and ring surrounding it. Structure $S4$ has the lowest $\chi^2$ value. Nevertheless, some shortcomings are also evident, mostly on the right hand side of the image. The $S1$ structure, which has only slightly higher $\chi^2$ value, shows some inconsistencies in intensity distribution at the edges of the image. The simulated image has distinct peaks in the intensity along the edge while the experimental image is more diffuse in this region possibly because of large thermal vibrations of the surface atoms. The reason for such discrepancies can also be transitions between structures during the imaging. The temperature is raised beyond room temperature because of heating by the electron beam, and observations of transitions during the imaging have been reported.[13,14,38] This can make it difficult to obtain close correspondence between any one cluster structure and an experimental image especially for such a small and disordered cluster. Considering such limitations, the agreement between these simulated images and the AC-STEM image can be considered to be adequate.

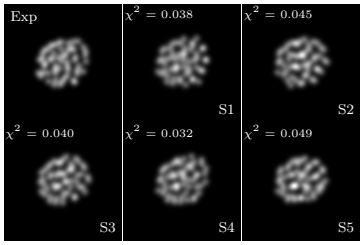


Figure 3: The AC-STEM image obtained from ref.[14] and simulated images, labeled $S1$-$S5$, for five of the $Au_{55}$ cluster structures obtained from the two phase fitting process which concludes with energy minimization using DFT/PBEsol. The $\chi^2$ value is the sum of squared pixel intensity differences between the AC-STEM image and the simulated image for each structure.

## Minimum Energy Path calculations

To explore the energy landscape in the vicinity of the optimal structures ($S1 - S5$), the minimum energy path connecting the corresponding minima on the DFT/PBEsol energy surface is calculated. The cluster structures are first ordered according to the average total distance between the atoms (*i.e.* the root mean square displacement, RMSD) and the path between adjacent pairs then calculated using the climbing image nudge elastic band (CI-NEB) method.[39?,40] with atomic forces obtained from DFT/PBEsol. When points indicating intermediate minima are found along the path, those configurations are further relaxed to the local minima, thereby revealing new low energy configurations ($S6-S11$) as can be seen in figure 4. Interestingly, minimum energy structures that are adjacent on the path can give quite different simulated images, showing that significant structural changes can take place as the system hops over a single, low energy barrier.

Table 1 gives the value of the $\chi^2$ measure of the fit to the AC-STEM image for the various structures, as well as the cluster structure with lowest energy found from the EMT potential function. Remarkably, the image produced from this EMT predicted structure image ranks rather high even though it bears no resemblance to the AC-STEM image. There, the local ordering of the atoms corresponds to that of the FCC crystal. It is, therefore, clear that the $\chi^2$ measure of the goodness of fit as defined in eqn. 3 is not sufficiently reliable. This sum over all pixels can be dominated by regions of the image that are not revealing about the atomic structure. To tackle this, a modified measure is defined by increasing the weight of the brighter pixels in the AC-STEM image. The pixels are ranked according to the intensity and divided into two equally large groups, the brighter and the fainter pixels. A weight parameter is introduced in the pixel-by-pixel discrepancy and

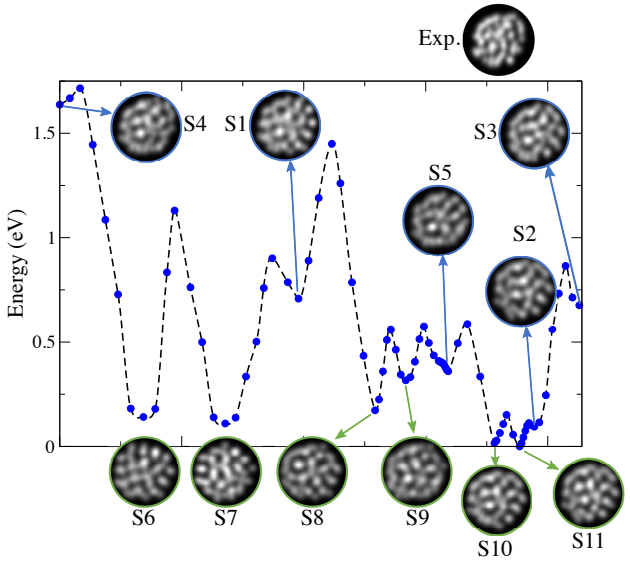


Figure 4: Minimum energy path between the five optimal $Au_{55}$ structures ($S1 - S5$) obtained in repeated fits of the AC-STEM image. Each blue dot corresponds to a cluster structure (an image) along the path obtained from the nudged elastic band calculation. New local minima ($S6$-$S11$) are found along the path and the corresponding simulated images are shown below. For comparison, the AC-STEM image is located above the graph.

equation 3 rewised as

$$ {}_s\chi^2(\boldsymbol{x},\boldsymbol{y},\sigma) = \sum_{i=1}^{m}\sum_{j=1}^{n}\Big(1+g_{ij}\Big)\Big(I'_{ij}-I_{ij}(\boldsymbol{x},\boldsymbol{y},\sigma)\Big)^2, \tag{5} $$

where $g_{ij} = 4$ if pixel $ij$ is among the brighter pixels, otherwise $g_{ij} = 0$.

Table 1 shows how the ranking of the fits changes by placing higher weight on the brighter pixels. In addition to the structures obtained from the image fit, some of the structures obtained from the minimum energy path calculation as well as the Garzón structure (referred to as Gar for short) and the EMT global minimum (shown in figure 2) are evaluated. With the increased weight on the brighter pixels, a better ranking of the structures is obtained. The EMT structure is, for example, ranked lower than the fitted structures. The Garzón structure, though, still ranks even lower than the clearly incorrect EMT structure.

It is clear that the $\chi^2$ measure can be deceiving and that increasing the importance of the brighter pixels in the experimental image, as expressed in eqn. 5, the ranking is more consistent with visual inspection (see ${}_s\chi^2$ values in table 1). The values reported in table 1 are obtained without further reorientation of the structures (*i.e.* the same set of structures is evaluated with the two objective functions). It is important to find a reliable numerical measure for the fit and while this increase in the weight of bright pix-

Table 1: Ordering of selected structures using the sum of squared pixel-by-pixel, $\chi^2$, discrepancy defined in eqn. 3 and a revised version where the brighter half of the pixels in the experimental image contribute five times more to the sum than the fainter pixels ${}_s\chi^2$, defined in eqn. 5. By increasing the weight of the brighter pixels, the numerical measure is more consistent with a visual inspection, lowering, for example, the rank of the image generated from the EMT lowest energy structure.

| $\chi^2$ | Structure | ${}_s\chi^2$ | Structure |
|---|---|---|---|
| 0.032 | S4 | 0.232 | S4 |
| 0.038 | S1 | 0.285 | S1 |
| 0.040 | S3 | 0.305 | S3 |
| 0.043 | EMT | 0.311 | S5 |
| 0.045 | S2 | 0.316 | S10 |
| 0.046 | S10 | 0.393 | S2 |
| 0.049 | S5 | 0.441 | EMT |
| 0.060 | S7 | 0.591 | GAR |
| 0.075 | Gar | 0.702 | S7 |

els clearly is a step in the right direction, more work on this is needed, possibly making use of techniques developed in signal processing and related fields. One advantage of the $\chi^2$ and ${}_s\chi^2$ measures is that they are differentiable so the atom displacements that decrease the discrepancy measure can, therefore, be obtained from the gradient with respect to the atom coordinates.

As can be seen from figure 4, a large difference can be seen between images of structures that are adjacent on the minimum energy path, *i.e.* separated by a single energy barrier. This occurs because of a concerted displacement of a large number of atoms. Note that overall rotation of the cluster is suppressed in the calculations as the RT-NEB algorithm was used.[41] To illustrate this, figure 5 shows the atomic displacement that take place when $S5$ transforms to $S9$. The RMSD between these structures is around 0.5 Å, and the energy barrier that needs to be surmounted is only 0.17 eV, which means that these kinds of fluctuations can occur frequently during the time scale of an AC-STEM measurement. Figure 5 shows a superposition of the $S5$ structure overlapped with the $S9$ structure and the displacement of each atom between the two is marked. Further analysis shows that the atoms moving most during the transition are located almost exclusively on the right hand side of the cluster, which is where the simulated images differ most from each other and from the AC-STEM image, as noted above.

In the experimental study of Wang and Palmer, a time series is reported where the AC-STEM image changes strongly with time and this was ascribed to rotations of the cluster.[14] There, each experimental image was matched as closely as possible to the structure predicted by Garzón *et al.* by rotating the cluster in small steps and visually comparing the simulated image to the experimental one. The results presented here from the minimum energy path calculation show that the structural fluctuations observed in the experiments may in fact be due to concerted change in the relative position of the atoms as the system undergoes a thermally activated structural transition, even a hop over just a single energy barrier, rather than rotation

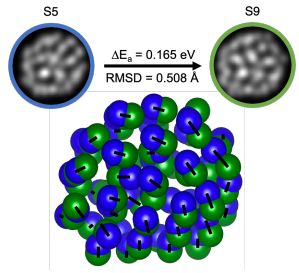


Figure 5: Transition between $S5$ and $S9$ structures of the $Au_{55}$ cluster. Top: Simulated images as well as the activation energy and the root-mean-square displacement between the structures. Bottom: A superposition of the atomic structures of $S5$ (blue) and $S9$ (green). Black lines connect initial and final positions of each atom.

of the cluster.

Table 2 gives the relative energy of various cluster structures obtained in the calculations. For the sake of comparison, the table also gives results for the high-symmetry $Au_{55}$ clusters such as the icosahedral, decahedral and cuboctahedral structures as well as configurations originating from energy minimization using Gupta function, EMT function and DFT based tight binding (DFTB)[42] followed by relaxation at the DFT/PBEsol level of theory. The relaxation is performed carefully using a small step size to ensure convergence to the nearest local minimum. There are only minor changes in the structures obtained with Gupta, EMT, and DFTB, and virtually no structural changes in the highly symmetry structures. (Information on the changes in the atomic coordinates during the DFT/PBEsol minimization can be found in the Supporting Information.)

As one might expect, there is a large difference in the energy of the various clusters. The optimal structure found by Garzón *et al.*[16] using the Gupta potential has the ninth highest energy of 0.51 eV above the lowest energy structure. The slightly distorted FCC-type structure predicted by the EMT potential function is much higher, 1.1 eV. The symmetric icosahedral (Ico), Ino-decahedral (Dec) and cuboctahedral (Cub) configurations are the least stable structures. The difference in the energy of the isomers found here from the fit to the AC-STEM image is less than 0.75 eV, with the exception of $S4$, and the energy barriers between most of them are small. As mentioned above, the small energy barriers between the isomers may be overcome by thermal activation and lead to the superposition of different isomers during AC-STEM imaging. This could account for smearing of the experimental image, especially around the edges of the cluster.

Table 2: Energy (eV) obtained with DFT/PBEsol of the $Au_{55}$ structures generated relative to the most stable one, $S11$. The energy difference between $S10$ and $S11$ is insignificant.

| Structure | $\Delta E$ | Structure | $\Delta E$ | Structure | $\Delta E$ |
|---|---|---|---|---|---|
| S11 | 0.00 | S9 | 0.32 | EMT | 1.12 |
| S10 | 0.02 | S5 | 0.41 | S4 | 1.64 |
| S2 | 0.10 | Gar | 0.51 | Ico | 1.71 |
| S7 | 0.12 | S3 | 0.68 | Dec | 2.59 |
| S6 | 0.16 | S1 | 0.71 | Cub | 3.31 |
| S8 | 0.18 | DFTB | 0.87 | | |

## Structural Analysis

To examine the atomic ordering of the clusters, the coordination number of the atoms is calculated and the local environment of pairs of atoms classified using the common neighbor analysis (CNA). Also, the electronic density obtained from the DFT/PBEsol calculations is analyzed. More details about the analyses can be found in the Methods section.

### Coordination Numbers

The coordination numbers of atoms in the five cluster structures that best agree with the AC-STEM image according to the ${}_s\chi^2$ measure (see table 1) are presented in figure 6. A cutoff distance of 3.3 Å is used to define neighboring (*i.e.* 'bonded') atoms. A similar analysis for other clusters is presented in the Supporting Information. Most of the clusters show pronounced peaks for coordination numbers 12, 8, 7, and 6. The exception is $S10$, the one with lowest

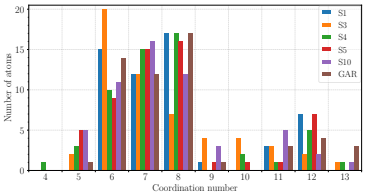


Figure 6: Top: Coordination numbers for the five structures that give best fit to the AC-STEM image according to the ${}_s\chi^2$ measure (see table 1), as well as the Garzón structure (after local minimization with DFT/PBEsol). Vertical axis shows number of atoms found with each coordination number. The cutoff distance for classifying atoms as neighbors ('bonded') is 3.3 Å.

DFT/PBEsol energy, which has a peak at a coordination number of 11 (the same is true for the similar $S11$ structure). The Garzón structure differs from the clusters obtained from the AC-STEM fitting in that it has higher coordination numbers, in particular three atoms with a coordination number of 13. The lower coordination numbers of structures obtained here by fitting the AC-STEM image, and even more so the lowest DFT/PBEsol energy structures, show that they are less compact than the Garzón structure.

### Common Neighbor Analysis

The CNA method characterizes the local environment of pairs of atoms by a set of three integer indices. The first one denotes the number of atoms that are neighbors of both atoms in the pair, the second index is the total number of bonds between the common neighbors, and the third index is the number of bonds in the longest continuous chain of bonds between the common neighbors. Additional information about CNA can be found in refs.[43–45]

Table 3 shows the relative abundance bonded pairs with the most common CNA indices for the five cluster structures that give best agreement with the AC-STEM image according to the ${}_s\chi^2$ measure (see table 1). Data on additional structures is provided in the Supporting Information. The CNA signature can, in particular, be used to distinguish between the local ordering in a crystal, as in the cuboctahedral structure, and the non-crystallographic, five-fold symmetry icosahedral structure. A distinction between the two can be made by looking at the numbers of pairs of type 421, 422 and 555, as can be seen from the table. The main difference between these structures is that pairs of type 421 that are abundant in the cuboctahedral structure, are not present in the icosahedral structure. On the contrary, pairs of type 555 and 422, which are abundant in the 55 atom icosahedral structure, are not present in the cuboctahedral structure. The Ino-decahedral cluster has slightly more 422 pairs than 421 pairs, due to local hexagonal close pack (HCP) ordering at the stacking faults. Otherwise, it has similar local ordering as the cuboctahedral structure. The 544 and 433 pairs are indicative of distorted icosahedral order as they form when a single bond is broken in the icosahedron. The sum of 555, 544, and 433 pairs in some of the structures obtained from the fit is comparable to the number of 555 pairs in the perfect icosahedron. For example, the sum of the 555, 544, and 433 pairs for $S10$ is 10.5%, similar to the total number of 555 pairs in the Ico structure, 10.3%. With this information, it becomes clear that the cluster structures obtained here from the AC-STEM image mainly have pairs that are typical of icosahedral ordering. Nevertheless, there is also a significant but smaller number of 421 pairs indicative of local FCC-type ordering of the atoms.

Figure 7 shows a a histogram of the CNA pairs. The blue color represents icosahedral while the red represents local FCC ordering as in the cuboctahedral structure. The main result of the CNA is that the $Au_{55}$ structures found here from the AC-STEM image have local atomic ordering that corresponds mainly to distorted icosahedral order, but also some that correspond to local FCC order. The Garzón

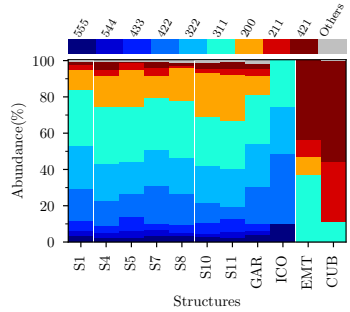


Figure 7: Histograms of various CNA pairs for selected structures. The color code is chosen to distinguish between icosahedral local order (blue) and FCC-type local order (red). CNA indices with small relative abundance are included as 'others'.

Table 3: Relative abundance of selected CNA pairs (in %) for the five structures that give best fit to the AC-STEM image according to the ${}_s\chi^2$ measure (see table 1). For comparison, the CNA pairs for Garzón, icosahedron, EMT, cuboctahedron and Ino-decahedron locally minimized with DFT/PBEsol are also given. Indices with small relative abundance, such as 444, are ignored.

| CNA index | S1 | S3 | S4 | S5 | S10 | Gar | Ico | EMT | Cub | Dec |
|---|---|---|---|---|---|---|---|---|---|---|
| 211 | 3 | 9 | 3 | 4 | 2 | 4 | 0 | 9 | 33 | 18 |
| 311 | 31 | 28 | 31 | 31 | 27 | 27 | 26 | 37 | 11 | 14 |
| 322 | 24 | 12 | 21 | 17 | 21 | 24 | 26 | 0 | 0 | 9 |
| 421 | 2 | 6 | 4 | 1 | 3 | 3 | 0 | 44 | 56 | 23 |
| 422 | 17 | 6 | 14 | 13 | 11 | 21 | 38 | 0 | 0 | 30 |
| 433 | 6 | 9 | 4 | 8 | 6 | 4 | 0 | 0 | 0 | 0 |
| 544 | 2 | 3 | 3 | 4 | 2 | 2 | 0 | 0 | 0 | 0 |
| 555 | 3 | 1 | 2 | 2 | 3 | 4 | 10 | 0 | 0 | 2 |

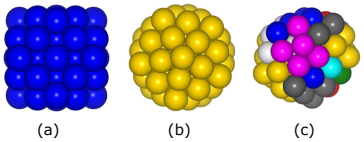


Figure 8: $Au_{55}$ structures with atoms colored according to the three critical CNA pairs: 421, 422 and 555. (a) cuboctahedral (Cub), (b) Icosahedral (Ico) and (c) $S10$ structure. Blue atoms are involved in 421 pairs, yellow atoms are involved in 422 and 555 pairs, magenta atoms are involved in 421 and 422 pairs (a characteristic of local hexagonal close pack ordering, HCP). Red atoms are characteristic of local FCC ordering, where 421 pairs are formed but not 422 pairs. White atoms are involved in all three types of pairs, 421, 422 and 555 and gray atoms are not involved in any of those three.

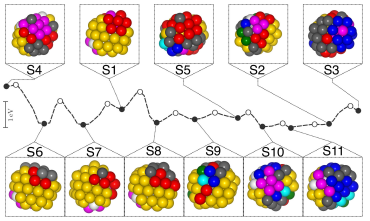


Figure 9: Color coding of the atoms in the $Au_{55}$ structures $S1 - S11$ according to the local environment characterized by the three critical CNA pairs as in figure 8. The minimum energy path connecting the structures is also shown (as in figure 4). Local energy minima and saddle points are represented by black and white circles, respectively.

structure has similar characteristics[15] but it has more icosahedral order than the structures that best fit the AC-STEM image.

To illustrate this analysis further, figure 8 shows color-coded configurations of the icosahedral, cuboctahedral and $S10$ structures. Even though the $S10$ structure appears to be highly disordered, it presents mostly an icosahedral-like structure with just a couple of atoms containing pairs related to the local FCC ordering. Every atom in the cuboctahedral structure has at least one 421 bonded pair and no 422 or 555 pairs. Every atom in the icosahedral structure has at least one 422 and one 555 pair but no 421. In the $S10$ structure, the majority of atoms have at least one 422 and one 555 pair but some atoms are involved in 421 pairs. These three types of pairs, 421, 422 and 555, can be used to classify the local atomic ordering in the core of the cluster, while some of the outer shell atoms are not involved in any of these pairs but rather lower CNA index pairs.

The evolution of the local atomic ordering

along the minimum energy path connecting structures $S1 - S11$ is shown in figure 9. The color scheme is the same as in figure 8, based on the three types of pairs that best describe the type of local ordering (*i.e.* 421, 422 and 555). Structures $S1$, $S7$, $S8$ and $S9$ in figure 9 are predominantly yellow, indicating local icosahedral ordering. Again, it can be seen how different two structures can be even if they are separated by only a single low energy barrier. This shows that a transition involving a hop over a single energy barrier changes the local environment of several atoms. The structures obtained for the $Au_{55}$ cluster can be described as 'Janus' structures in that they have a part that corresponds to icosahedral structure and another part that exhibits local order characteristic of the FCC crystal.

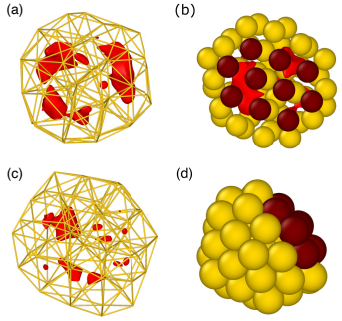


Figure 10: Electron density isosurface shown in (a) and (c) in red for $S10$ and Garzón structures, resp. The isosurface level rendered is 0.1 e $Å^{-3}$. This highlights cavities in the electron density between the core of the cluster and the surface shell. In (b) and (d) the the atoms forming a flat surface facet in the $S10$ structure are colored in dark red. The two figures correspond to different viewing angle.

**Electronic density**

The DFT/PBEsol calculations also give valuable information about the electronic structure of the cluster. A surprising feature is that the electron density shows regions of low density in between the surface layer of atoms and the inner core of the cluster. This is particularly notable for the lowest energy structures, such as $S10$ as shown figure 10(a). The presence of such cavities has been previously noted and discussed in terms of compaction of the surface layer.[42] A more detailed inspection shows that out of the three largest cavities in the structure, two of them are below a flat facet of the cluster. Figure 10(b) shows $S10$ with a view directly on this flat facet where the atoms constituting it have been highlighted. The atoms are arranged as in a close packed layer,indicating local ordering analogous to that in the FCC crystal. While such cavities in the electronic density are also present in the DFT/PBEsol relaxed Garzón structure (figure 10(c)), they are significantly smaller, consistent with a more compact atom packing. Figure 10(d) shows an orientation of $S10$ where the flat facet can be seen clearly.

## Conclusion

To summarize, a method is presented for performing systematic analysis of experimental AC-STEM images and it is applied to the $Au_{55}$ cluster to obtain a set of low-energy structures that fit an AC-STEM image reasonably well. A more detailed fit may be impossible in this case as the structure of such a small and disordered cluster may easily be changing during the measurement. The first phase of the method corresponds to the extraction of $(x, y)$ coordinates of the atoms by placing a Gaussian representing the contribution of each atom to the image, and assigning a $z$-coordinate using a random number generator to construct a three-dimensional structure. Local optimization of the structure is carried out after the placement of each atom using an objective function that combines pixel-by-pixel fit to the image and approximate energy function to represent the interaction be-

tween the atoms. Then, after generating several such trial structures using different random number seeds, an optimization is carried out using either GOUST or GA algorithm. A simple EMT energy function was used in the objective function to keep the computational cost low. Even though the lowest energy structure predicted by the EMT potential is inconsistent with the experimental image, it has turned out to be adequate as a component in the objective function. It only serves to give a rough estimate of the distance between neighboring atoms and an attraction to ensure compact structure. Finally, the optimized structures are relaxed using electronic structure calculations based on DFT/PBEsol. A simple numerical measure for the goodness of fit generated as a sum over pixel-by-pixel squared intensity difference turns out be useful for fine adjustments in the cluster structure, but does not eliminate well enough images that differ strongly from the target image. A revised measure where the weight of bright pixels is increased fivefold is found to work better in such cases.

The potential energy surface in the vicinity of the best fit structures is characterized by calculating the minimum energy path connecting the local energy minima. This reveals the presence of several new, adjacent local minima, some with lower energy and nearly as good fit to the AC-STEM image. Transitions between neighboring structures along the minimum energy path can in some cases occur readily by thermal activation and a hop over a single energy barrier typically involves concerted displacement of several atoms in the cluster. This rearrangement of the atoms can lead to large changes in the simulated AC-STEM images and could shed light on the rapid structural fluctuations observed in the AC-STEM experiments. They have been attributed to rotations of the cluster, but from the calculations presented here it is evident that they are more likely due to concerted displacements of several atoms that may even involve a hop over just a single energy barrier. Given that some of the calculated energy barriers between the structures are small, the corresponding transitions could be fast on the time scale of the experimental measurements, so the measured images may be a superposition of two or more structures, making a perfect fit with any one structure impossible in this case.

The CNA structural analysis performed reveals that the structures obtained can be described as 'Janus' type clusters, where a part of the structure has local icosahedral ordering of the atoms and the other part has local order characteristic of the crystal. This is also manifested by a flat surface segment corresponding to a close-packed layer with 10 atoms, characteristic of crystalline ordering.

## Methods

**Minimization of the $\chi^2$ measure.** An important aspect of the analysis method is systematic optimization of the atom coordinates as well as the width parameter in the Gaussian representing the signal originating at an atom. Using the $\chi^2$ measure, the steepest descent direction for reducing the in the discrepancy between a simulated and measured images can be obtained by differentiating $\chi^2$. Using $I_{ij} = I_{ij}(\boldsymbol{x},\boldsymbol{y},\sigma)$ and $\chi^2 = \chi^2(\boldsymbol{x},\boldsymbol{y},\sigma)$ to shorten the notation, the partial derivative of $\chi^2$ with respect to the $x$-component of atom $k$ can be written as

$$\frac{\partial \chi^2}{\partial x_k} = -2 \sum_{i=1}^{m} \sum_{j=1}^{n} \left(I'_{ij} - I_{ij}\right) \frac{\partial I_{ij}}{\partial x_k}, \qquad (6)$$

with

$$\frac{\partial I_{ij}}{\partial x_k} = \frac{1}{\sigma^2} \left(x'_i - x_k\right) I_{ij}(x_k, y_k, \sigma). \qquad (7)$$

Substituting Eq. 7 into Eq. 6 and using $I^{(k)}_{ij} = I_{ij}(x_k,y_k,\sigma)$, the $x$-component of the steepest descent vector for atom $k$ is

$$\frac{\partial \chi^2}{\partial x_k} = -\frac{2}{\sigma^2} \sum_{i=1}^{m} \sum_{j=1}^{n} \left(I'_{ij} - I_{ij}\right) \left(x'_i - x_k\right) I^{(k)}_{ij}. \quad (8)$$

Similarly, the $y$-component of the steepest descent vector for atom $k$ is

$$\frac{\partial \chi^2}{\partial y_k} = -\frac{2}{\sigma^2} \sum_{i=1}^{m} \sum_{j=1}^{n} \left(I'_{ij} - I_{ij}\right) \left(y'_j - y_k\right) I^{(k)}_{ij}, \quad (9)$$

and the $\sigma$-component of the gradient vector is

$$\frac{\partial \chi^2}{\partial \sigma} = -\frac{2}{\sigma^3}\sum_{i=1}^{m}\sum_{j=1}^{n}(I'_{ij}-I_{ij})\left(\left(x'_i-x_k\right)^2+\left(y'_j-y_k\right)^2\right)I_{ij}. \quad (10)$$

It is important to note that $I_{ij} = I_{ij}(\boldsymbol{x}, \boldsymbol{y}, \sigma)$ in the above equations represents the intensity from all atoms whereas $I_{ij}^{(k)} = I_{ij}(x_k, y_k, \sigma)$ represents the intensity from atom $k$ only.

**Preparation of AC-STEM Image.** The experimental AC-STEM image used in this work is adapted from figure 3(a) in ref.[14] Based on the scale bar presented in the image, a box of size roughly 2.5 nm by 2.5 nm containing the cluster is cropped from the image (see Fig 11a). Although the image had been processed by the authors to remove noise and enhance image quality, some noise is still visible in the vicinity of the cluster, especially around the edges. For example, small bright spots that are spatially separated from the main cluster can be seen in the image, as indicated by red circles in figure 11b. These isolated features and small intensity patches around the edges are not considered as part of the cluster and are removed from the image. In this way, the noise in the image is significantly reduced as shown in figure 11c.

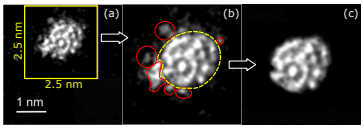


Figure 11: (a) Experimental AC-STEM image for $Au_{55}$ from ref.[14] (b) Cropped image. Noise can be seen in the vicinity of the cluster, as indicated by red circles. (c) Image used in the fitting process, with noise removed.

**GOUST Algorithm.** The method is based on finding new local minima of the objective function by identifying first order saddle points (SPs) on the objective function surface starting from a given local minimum and then sliding down to adjacent local minima on the other side of the SP. The method is implemented in the EON software[46] and a more detailed explanation of the method can be found in refs.[31,47] To minimize the objective function given in Eq. 4, the first step is to perform a local minimization starting from some value of the parameters (*i.e.* atom coordinates and Gaussian width) so as to make sure that the search for saddle points will start from a local minimum. In this and other energy minimization calculations carried out here, the velocity projection optimization (VPO) method[48] is first used until the magnitude of atomic forces has dropped below 0.5 eV/Å, and then convergence to 0.01 eV/Å is reached with the BFGS[49,50] method. After a local minimum has been reached, a slight change in the parameter values (atom coordinates and Gaussian width) is made, as in the adaptive kinetic Monte Carlo method.[51] The set of new values serves as a starting point for the SP searches. A climb up the objective function surface to a SP is carried out using the minimum mode following method.[32,33] After reaching a SP, a displacement along the minimum mode vector is made followed by a local minimization to get to the adjacent minimum. For a given local minimum, several SP searches are carried out in order to find several surrounding SPs and adjacent minima. Finally, from the list of local minima found in this way, the one with the lowest value of the objective function is selected and a new search for SPs carried out. The process is repeated until the system reaches a local minimum of the objective function that is lower than any of the nearby local minima. In this way, the system is taken down a funnel on the objective function surface, but it does not guarantee that a global minimum has been reached.

**Genetic Algorithm.** A genetic algorithm (GA) implemented in the Atomic Simulation Environment (ASE)[52,53] is used. The starting configurations were generated by the fitting process in the first phase. During the GA evolution, new structures are generated either by crossover or mutation. In the case of crossover, two structures are selected from the population and an offspring is produced through the pairing of the parent structures. Crossover is carried out 75% of the time using the standard cut-splice algorithm.[54] To maintain population diversity, mutation is performed 25% of the time.

During a mutation a cluster is selected and a new structure is generated by randomly displacing the atoms in the cluster in random directions by a distance that ranges from zero to 1.5 Å. The new structure is locally relaxed using BFGS to the nearest local minimum on the combined objective function and the population is updated so that it always contains the best 20 unique structures. The loop is repeated until 2000 structures have been tested.

**DFT Calculations.** The DFT calculations are performed using the PBEsol functional approximation,[?] and a plane-wave basis set with a kinetic energy cutoff of 250 eV. The choice of this functional was motivated by recent studies that found PBEsol to be more accurate than other generalized gradient approximation (GGA) functionals for small gold clusters.[55] The calculations are performed in a cubic simulation box of side length 25 Å. Gaussian smearing is used with a width of 0.1 eV. Spin polarization is not included. The Vienna *ab initio* simulation package (VASP) is used in the DFT calculations.[56]

**CI-NEB Calculations.** The minimum energy path between structures $S1$-$S5$ is calculated using the climbing image nudged elastic band (CI-NEB) method.[39,40] Six intermediate images are used to provide a discrete representation of the path. The image dependent pair potential (IDPP) method[57] is used to generated an initial path from which the CI-NEB optimization is carried out. To avoid rotation of intermediate images, the RT-NEB algorithm is used.[41]

**Visualization.** Matplotlib,[58] an open-source Python visualizations package, is used for graphical data visualization. All cluster structures are rendered using VESTA.[59]

## Acknowledgements

This project was funded by the Icelandic Research Fund and the research fund of the University of Iceland. KSB acknowledges a Ph.D. fellowship from the Doctoral Fund of the University of Iceland. We thank Emil Gauti Fridriksson for help in implementing the objective function in the EON software. The calculations were carried out at the Icelandic Research High Performance Computing (IRHPC) facility.

## References

1. Ray, P. C. Size and Shape Dependent Second Order Nonlinear Optical Properties of Nanomaterials and Their Application in Biological and Chemical Sensing. *Chemical Reviews* **2010**, *110*, 5332–5365.

2. Liu, J.; Fullerton, E.; Gutfleisch, O.; Sellmyer, D. *Nanoscale Magnetic Materials and Applications*; Springer US, 2014.

3. Corain, B.; Schmid, G.; Toshima, N. *Metal Nanoclusters in Catalysis and Materials Science: The Issue of Size Control*; Elsevier Science, 2011.

4. Dellby, N.; Krivanek, L.; Nellist, D.; Batson, E.; Lupini, R. Progress in aberration-corrected scanning transmission electron microscopy. *Journal of Electron Microscopy* **2001**, *50*, 177–185.

5. Batson, P.; Dellby, N.; Krivanek, O. Sub-Å resolution using aberration corrected electron optics. *Nature* **2002**, *418*, 617.

6. Li, Z. Y.; Young, N. P.; Di Vece, M.; Palomba, S.; Palmer, R. E.; Bleloch, A. L.; Curley, B. C.; Johnston, R. L.; Jiang, J.; Yuan, J. Three-dimensional atomic-scale structure of size-selected gold nanoclusters. *Nature* **2008**, *451*, 46–48.

7. Van Aert, S.; Batenburg, K. J.; Rossell, M. D.; Erni, R.; Van Tendeloo, G. Three-dimensional atomic imaging of crystalline nanoparticles. *Nature* **2011**, *470*, 374–377.

8. Deepak, F. L.; Anumol, E. A.; Li, J. In *Metal Nanoparticles and Clusters: Advances in Synthesis, Properties and Applications*; Deepak, F. L., Ed.; Springer International Publishing: Cham, 2018; pp 219–287.

9. Wells, D. M.; Rossi, G.; Ferrando, R.; Palmer, R. E. Metastability of the atomic structures of size-selected gold nanoparticles. *Nanoscale* **2015**, *7*, 6498–6503.

10. Jian, N.; Stapelfeldt, C.; Hu, K.-J.; Fröba, M.; Palmer, R. E. Hybrid atomic structure of the Schmid cluster $Au_{55}(PPh3)_{12}Cl_6$ resolved by aberration-corrected STEM. *Nanoscale* **2015**, *7*, 885–888.

11. Liu, J.; Jian, N.; Ornelas, I.; Pattison, A. J.; Lahtinen, T.; Salorinne, K.; Häkkinen, H.; Palmer, R. E. Exploring the atomic structure of 1.8 nm monolayer-protected gold clusters with aberration-corrected STEM. *Ultramicroscopy* **2017**, *176*, 146 – 150.

12. Wang, Z. W.; Toikkanen, O.; Quinn, B. M.; Palmer, R. E. Real-Space Observation of Prolate Monolayer-Protected $Au_{38}$ Clusters Using Aberration-Corrected Scanning Transmission Electron Microscopy. *Small* **2011**, *7*, 1542–1545.

13. Wang, Z. W.; Toikkanen, O.; Quinn, B. M.; Palmer, R. E. Real-Space Observation of Prolate Monolayer-Protected Au38 Clusters Using Aberration-Corrected Scanning Transmission Electron Microscopy. *Small* **2011**, *7*, 1542–1545.

14. Wang, Z.; Palmer, R. E. Experimental Evidence for Fluctuating, Chiral-Type $Au_{55}$ Clusters by Direct Atomic Imaging. *Nano Letters* **2012**, *12*, 5510–5514.

15. Garzón, I. L.; Posada-Amarillas, A. Structural and vibrational analysis of amorphous $Au_{55}$ clusters. *Phys. Rev. B* **1996**, *54*, 11796–11802.

16. Garzón, I. L.; Michaelian, K.; Beltrán, M. R.; Posada-Amarillas, A.; Ordejón, P.; Artacho, E.; Sánchez-Portal, D.; Soler, J. M. Lowest Energy Structures of Gold Nanoclusters. *Phys. Rev. Lett.* **1998**, *81*, 1600–1603.

17. Koch, C. Determination of Core Structure Periodicity and Density Along Dislocations. *PhD dissertation* **2002**,

18. Wales, D. J.; Scheraga, H. A. Global Optimization of Clusters, Crystals, and Biomolecules. *Science* **1999**, *285*, 1368–1372.

19. Wales, D. *Energy Landscapes: Applications to Clusters, Biomolecules and Glasses*; Cambridge Molecular Science; Cambridge University Press, 2004.

20. Oakley, M. T.; Johnston, R. L.; Wales, D. J. Symmetrisation schemes for global optimisation of atomic clusters. *Phys. Chem. Chem. Phys.* **2013**, *15*, 3965–3976.

21. Watanabe, K.; Yamazaki, T.; Hashimoto, I.; Shiojiri, M. Atomic-resolution annular dark-field STEM image calculations. *Phys. Rev. B* **2001**, *64*, 115432.

22. Kirkland, E. *Advanced Computing in Electron Microscopy*; 2010.

23. Ferrer, D.; Blom, D. A.; Allard, L. F.; Mejía, S.; Pérez-Tijerina, E.; José-Yacamán, M. Atomic structure of three-layer Au/Pd nanoparticles revealed by aberration-corrected scanning transmission electron microscopy. *J. Mater. Chem.* **2008**, *18*, 2442–2446.

24. Deepak, F. L.; Mayoral, A.; Steveson, A. J.; Mejía-Rosales, S.; Blom, D. A.; José-Yacamán, M. Insights into the capping and structure of MoS2 nanotubes as revealed by aberration-corrected STEM. *Nanoscale* **2010**, *2*, 2286–2293.

25. Logsdail, A. J.; Li, Z. Y.; Johnston, R. L. Development and optimization of a novel genetic algorithm for identifying nanoclusters from scanning transmission electron microscopy images. *Journal of Computational Chemistry* **2012**, *33*, 391–400.

26. Meredig, B.; Wolverton, C. A hybrid computational–experimental approach for

automated crystal structure solution. *Nature Materials* **2013**, *12*, 123–127.

27. Yu, M.; Yankovich, A. B.; Kaczmarowski, A.; Morgan, D.; Voyles, P. M. Integrated Computational and Experimental Structure Refinement for Nanoparticles. *ACS Nano* **2016**, *10*, 4031–4038.

28. Garden, A. L.; Pedersen, A.; Jónsson, H. Reassignment of 'magic numbers' for Au clusters of decahedral and FCC structural motifs. *Nanoscale* **2018**, *10*, 5124–5132.

29. Sukuta, K.; Van den Bossche, M.; Pedersen, A.; Jónsson, H. Nanocluster structure deduced from AC-STEM images coupled to theoretical modelling. *Nanosystems: Physics, Chemistry, Mathematics* **2017**, *8*, 723–731.

30. Jacobsen, K.; Stoltze, P.; Nørskov, J. A semi-empirical effective medium theory for metals and alloys. *Surface Science* **1996**, *366*, 394 – 402.

31. Plasencia, M.; Pedersen, A.; Arnaldsson, A.; Berthet, J.-C.; Jónsson, H. Geothermal model calibration using a global minimization algorithm based on finding saddle points and minima of the objective function. *Computers & Geosciences* **2014**, *65*, 110 – 117.

32. Henkelman, G.; Jónsson, H. A dimer method for finding saddle points on high dimensional potential surfaces using only first derivatives. *The Journal of Chemical Physics* **1999**, *111*, 7010–7022.

33. Gutiérrez, M. P.; Argáez, C.; Jónsson, H. Improved minimum mode following method for finding first order saddle points. *J. Chem. Theory Comput.* **2017**, *13*, 125.

34. Daven, D.; Tit, N.; Morris, J.; Ho, K. Structural optimization of Lennard-Jones clusters by a genetic algorithm. *Chemical Physics Letters* **1996**, *256*, 195 – 200.

35. Michaelian, K.; Rendón, N.; Garzón, I. L. Structure and energetics of Ni, Ag, and Au nanoclusters. *Phys. Rev. B* **1999**, *60*, 2000–2010.

36. Vilhelmsen, L. B.; Hammer, B. A genetic algorithm for first principles global structure optimization of supported nano structures. *The Journal of Chemical Physics* **2014**, *141*, 044711.

37. Van den Bossche, M. DFTB-Assisted Global Structure Optimization of 13- and 55-Atom Late Transition Metal Clusters. *The Journal of Physical Chemistry A* **2019**, *123*, 3038–3045.

38. Wang, Z. W.; Palmer, R. E. Determination of the Ground-State Atomic Structures of Size-Selected Au Nanoclusters by Electron-Beam-Induced Transformation. *Phys. Rev. Lett.* **2012**, *108*, 245502.

39. Henkelman, G.; Uberuaga, B. P.; Jónsson, H. A climbing image nudged elastic band method for finding saddle points and minimum energy paths. *The Journal of Chemical Physics* **2000**, *113*, 9901–9904.

40. Henkelman, G.; Jónsson, H. Improved tangent estimate in the nudged elastic band method for finding minimum energy paths and saddle points. *The Journal of Chemical Physics* **2000**, *113*, 9978–9985.

41. Melander, M.; Laasonen, K.; Jónsson, H. Removing External Degrees of Freedom from Transition-State Search Methods using Quaternions. *Journal of Chemical Theory and Computation* **2015**, *11*, 1055–1062.

42. Van den Bossche, M. DFTB-Assisted Global Structure Optimization of 13- and 55-Atom Late Transition Metal Clusters. *The Journal of Physical Chemistry A* **2019**, *123*, 3038–3045.

43. Honeycutt, J. D.; Andersen, H. C. Molecular dynamics study of melting and freezing of small Lennard-Jones clusters. *The Journal of Physical Chemistry* **1987**, *91*, 4950–4963.

44. Clarke, A. S.; Jónsson, H. Structural changes accompanying densification of random hard-sphere packings. *Phys. Rev. E* **1993**, *47*, 3975–3984.

45. Faken, D.; Jónsson, H. Systematic analysis of local atomic structure combined with 3D computer graphics. *Computational Materials Science* **1994**, *2*, 279 – 286.

46. Chill, S. T.; Welborn, M.; Terrell, R.; Zhang, L.; Berthet, J.-C.; Pedersen, A.; Jónsson, H.; Henkelman, G. EON: software for long time simulations of atomic scale systems. *Modelling and Simulation in Materials Science and Engineering* **2014**, *22*, 055002.

47. Pedersen, A.; Berthet, J.-C.; Jónsson, H. Simulated Annealing with Coarse Graining and Distributed Computing. *Lecture Notes in Computer Science* **2014**, *7134*, 34.

48. Jónsson, H.; Mills, G.; Jacobsen, K. W. *Nudged elastic band method for finding minimum energy paths of transitions*; World Scientific, 1998.

49. Head, J. D.; Zerner, M. C. A Broyden-Fletcher-Goldfarb-Shanno optimization procedure for molecular geometries. *Chemical Physics Letters* **1985**, *122*, 264 – 270.

50. Nocedal, J.; Wright, S. J. *Numerical Optimization*, 2nd ed.; Springer: New York, NY, USA, 2006.

51. Pedersen, A.; Hafstein, S. F.; Jónsson, H. Efficient Sampling of Saddle Points with the Minimum-Mode Following Method. *SIAM Journal of Scientific Computing* **2011**, *33*, 633.

52. Larsen, A. H.; Mortensen, J. J.; Blomqvist, J.; Castelli, I. E.; Christensen, R.; Dułak, M.; Friis, J.; Groves, M. N.; Hammer, B.; Hargus, C. *et al.* The atomic simulation environment—a Python library for working with atoms. *Journal of Physics: Condensed Matter* **2017**, *29*, 273002.

53. Bahn, S. R.; Jacobsen, K. W. An object-oriented scripting interface to a legacy electronic structure code. *Comput. Sci. Eng.* **2002**, *4*, 56–66.

54. Wolf, M. D.; Landman, U. Genetic Algorithms for Structural Cluster Optimization. *The Journal of Physical Chemistry A* **1998**, *102*, 6129–6137.

55. Johansson, M. P.; Lechtken, A.; Schooss, D.; Kappes, M. M.; Furche, F. 2D-3D transition of gold cluster anions resolved. *Phys. Rev. A* **2008**, *77*, 053202.

56. Kresse, G.; Furthmüller, J. Efficient iterative schemes for ab initio total-energy calculations using a plane-wave basis set. *Phys. Rev. B* **1996**, *54*, 11169–11186.

57. Smidstrup, S.; Pedersen, A.; Stokbro, K.; Jónsson, H. Improved initial guess for minimum energy path calculations. *The Journal of Chemical Physics* **2014**, *140*, 214106.

58. Hunter, J. D. Matplotlib: A 2D graphics environment. *Computing in Science & Engineering* **2007**, *9*, 90–95.

59. Momma, K.; Izumi, F. *VESTA3* for three-dimensional visualization of crystal, volumetric and morphology data. *Journal of Applied Crystallography* **2011**, *44*, 1272–1276.

## Graphical TOC Entry

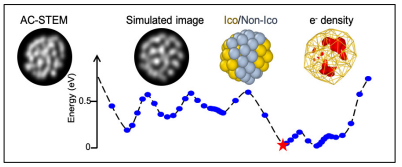

# Article III

**Theoretical Analysis of AC-STEM Images of Nanoclusters: Feature Based Method for Assessing the Quality of Fit**

Kusse S. Bersha, Hannes Jónsson

*Submitted to Nanosystems: Physics, Chemistry, Mathematics*. 2021. 0(0):0-8

NANOSYSTEMS: PHYSICS, CHEMISTRY, MATHEMATICS, 2021, 0 (0), P. 0–8

# Theoretical Analysis of AC-STEM Images of Nanoclusters: Feature Based Method for Assessing the Quality of Fit

Kusse S. Bersha, Hannes Jónsson

Science Institute and Faculty of Physical Sciences, University of Iceland, 107 Reykjavík, Iceland

The physical and chemical properties of nanoclusters depend strongly on the arrangement of the atoms, i.e. the atomic structure of the cluster, but this is difficult to determine experimentally as well as theoretically. The aberration corrected scanning transmission electron microscope (AC-STEM) is a recently developed experimental technique that can provide valuable information about nanocluster structure, but the analysis of such images in terms of atomic structure has so far mainly been qualitative rather than quantitative. Detailed analysis of AC-STEM images using theoretical modeling requires a reliable, quantitative measure of the extent to which a simulated image agrees with an experimentally measured image. A simple sum of pixel-by-pixel error squared turns out to be unreliable and a more advanced measure is needed. Here, a quantitative measure based on the 'Speeded Up Robust Features' (SURF) algorithm is presented and applied to an image of a $Au_{55}$ cluster, a particularly challenging case since the atomic structure is irregular. The method does not rely on an alignment of atoms into rows and it can be applied successfully even when significant noise is added to the image.

**Keywords:** nanocluster, AC-STEM, atomic structure, global optimization, pattern recognition.

## 1. Introduction

Nanoclusters have attracted much attention in recent years in a range of applications such as catalysis, optoelectronics, and magnetism [1–4]. Gold nanoclusters have, for example, been found to have remarkable catalytic properties, such as efficient low temperature oxidation of CO, but mainly when the cluster diameter is within a rather narrow range, between 2-3nm [5, 6]. A major obstacle in gaining a better understanding of nanoclusters is the lack of information about the atomic structure. An experimental technique providing information about the atomic scale structure of nanoclusters has largely been lacking until the development of the aberration-corrected scanning transmission electron microscope (AC-STEM) [7, 8].

The development of AC-STEM has enabled researchers to obtain high-resolution, two-dimensional images of nanoclusters, in particular Au clusters [9, 10]. However, while the experimental capabilities of AC-STEM equipment have been developed to a high degree, the analysis of the images to determine the atomic structure of the clusters has remained rather simple. In some cases, a catalog of simulated images based on ideal cluster structures is generated and the measured images then compared to the catalog by visual inspection. While this type of analysis of the AC-STEM images is in many ways good enough to distinguish between types of ordered structures such as cuboctahedra, icosahedra, and decahedra, these ideal structure motifs do not apply in all cases and more robust and powerful analysis tools are required. This is particularly true for small Au clusters such as $Au_{55}$ where the atomic ordering is irregular.

In recent years, some effort has been made to develop analysis methods for AC-STEM images. For example, Yu *et al.* used a genetic algorithm to extract atomic coordinates of

columns of atoms, but such a method is not applicable to irregular structures such as $Au_{55}$ where the atoms are not lined up in well defined columns. In an impressive experimental study, Wang and Palmer [10] could, nevertheless, identify about 50% of the measured AC-STEM images for $Au_{55}$ as being consistent with a structure predicted from simulations based on the empirical Gupta atomic interaction potential [12]. In another experimental study, Li *et al.* identified the structures of various Au nanoclusters containing $309 \pm 6$ atoms as being close to one of the three ideal structure motifs [9] but deviations between the simulated and experimental images are still evident and indicate that more information about the atomic structure of the clusters could be obtained with a more quantitative analysis.

Recently, a general method applicable in studies of irregular atomic structures has been developed for the analysis of AC-STEM images [13,14]. The method was applied to an experimental AC-STEM image of $Au_{55}$ cluster to estimate the coordinates of the atoms in the cluster. Together with electron density functional theory (DFT) calculations of minimum energy structures and minimum energy paths between low energy structures, the method has provided valuable information about possible atomic ordering in this nanocluster. The method involves optimization of a combined objective function that takes into account the discrepancy between a simulated image and the experimental AC-STEM image, as well as an energy estimate given by a rough approximation of the interaction between the atoms in the cluster. This is followed by a DFT calculation to finally rank the structures obtained. There, the discrepancy between a simulated image and the experimental AC-STEM image was based on a sum over pixel-by-pixel difference in intensity squared. This comparison, which we will refer to as the mean squared error (MSE) measure, turns out to be useful only when the images have a high degree of similarity and it can then be used to refine the atomic structure. But, remarkably, images that are entirely different can give a similarly low value of the MSE and falsely indicate a good match. Examples of that are given below.

In this article, a new quantitative measure is presented for the difference between a simulated image and an experimental AC-STEM image. The new method is based on a computer vision algorithm for determining the similarity between images through distinct features extracted from the image. The method is compared with the MSE, an improved version of the MSE where brighter pixels have more weight, as well as another method, the structural similarity index method (SSIM). The results obtained from studies of the $Au_{55}$ cluster indicate that the measure proposed here is efficient and would be useful in future AC-STEM image analysis.

## 2. Methodology

A similarity measure is important in many signal processing applications. Three commonly used measures of image similarity are: (1) the mean squared error (MSE), (2) the peak signal-to-noise ratio (PSNR), and (3) the structural similarity index measure (SSIM). Algorithms for determining image similarity have in many cases been based on one of these measures. The PSNR is mainly useful for comparing images having different dynamic range but otherwise does not provide new information relative to the MSE. Since the dynamic range of the images in the present case is similar, PSNR will not be considered in this work. A quantitative measure based on the 'Speeded Up Robust Features' (SURF) algorithm is presented and its performance in analysis of an AC-STEM image of a $Au_{55}$ cluster compared with that of the MSE measure, an improved MSE where brighter pixels are given higher weight, and the SSIM.

### 2.1. Mean squared error

The mean squared error (MSE) measure is widely used in signal processing applications. It has been the standard measure not only for the evaluation of signal fidelity and quality but also for the design and optimization of signal processing algorithms and systems [15]. It has many desirable mathematical properties such as symmetry, convexity, and differentiability. Moreover, it is simple to understand and easy to compute. The MSE is calculated by summing the squared intensity difference pixel-by-pixel between the images being compared. Given two images $I$ and $I'$, the MSE is defined as

$$\mathrm{MSE} = \frac{1}{mn}\sum_{i=1}^{m}\sum_{j=1}^{n}\Big(I_{ij} - I'_{ij}\Big)^2 \tag{1}$$

where $m$ and $n$ are the numbers of rows and columns of pixels in the image. An MSE value of 0 indicates perfect similarity. The numerical value depends on the normalization used for the intensity. In the present case, the integrated intensity over all pixels is set to unity.

### 2.2. Improved mean squared error

The MSE turns out not to correlate well with the perceived similarity of simulated and measured AC-STEM images unless they are similar enough. An image that is entirely different from the target image can give a value of MSE that is similar to that of a good fit. Bersha *et al.* modified the MSE by introducing a weight parameter to emphasize the brighter pixels and this was shown to improve the ranking of various cluster structures [14]. The pixels of the target image are grouped into two equally large groups, the brighter pixels and the less bright pixels. The improved mean squared error (IMSE) measure is

$$\mathrm{IMSE} = \frac{1}{mn}\sum_{i=1}^{m}\sum_{j=1}^{n}\omega_{ij}\Big(I_{ij} - I'_{ij}\Big)^2 \tag{2}$$

where the weight is $\omega_{ij} = 5$ if the pixel $(i, j)$ belongs to the set of brighter pixels, otherwise it is $\omega_{ij} = 1$. This IMSE measure was found to eliminate images generated for cluster structures that are clearly not accurate for $Au_{55}$ and have no apparent similarity to the experimentally measured AC-STEM image, but nevertheless give a low value of MSE [14].

### 2.3. Structural similarity index measure

The structural similarity index measure (SSIM) is widely used when digital images are compared [16]. It is computed locally within a sliding window of a certain size, defining a patch of the image, that moves across the image. The average intensity of a patch of image $I$ centered on pixel $(i, j)$ is

$$\mu_{ij} = \sum_{k=i-N}^{i+N}\sum_{l=j-N}^{j+N} I_{kl} \tag{3}$$

and similarly $\mu'_{ij}$ is calculated for the other image, $I'$. Here, the size of the patch is chosen to correspond to $N = 3$. The luminance, $l$, of the patch is defined as

$$l_{ij} = \frac{2\mu_{ij}\mu'_{ij} + \epsilon_1}{(\mu_{ij})^2 + (\mu'_{ij})^2 + \epsilon_1} \tag{4}$$

where $\epsilon_1$ is a small positive constant chosen to prevent the denominator from having zero value. Similarly, a standard deviation, $\sigma$, of the intensity is evaluated for each patch and the

contrast, $c$, defined as

$$c_{ij} = \frac{2\sigma_{ij}\sigma'_{ij} + \epsilon_2}{(\sigma_{ij})^2 + (\sigma'_{ij})^2 + \epsilon_2} \tag{5}$$

where again $\epsilon_2$ is a small positive constant chosen to prevent the denominator from having zero value. Finally, a covariance $\sigma_{ij,i'j'}$ is evaluated for the patches and structural similarity measure, $s$, defined as

$$s_{ij} = \frac{\sigma_{ij,i'j'} + \epsilon_3}{\sigma_{ij}\sigma'_{ij} + \epsilon_3} \tag{6}$$

where $\epsilon_3$ is a small positive number.

The local similarity measure, $M$, for the image patch centered at pixel $(i, j)$ is then a weighted combination of these three quantities

$$\mathrm{M}_{ij} = (l_{ij})^{\alpha}\ (c_{ij})^{\beta}\ (s_{ij})^{\gamma} \tag{7}$$

If the weights are chosen to be equal, $\alpha$=$\beta$=$\gamma$=1, and $\epsilon_3$=$\epsilon_2/2$, the local similarity measure becomes

$$\mathrm{M}_{ij} = \frac{(2\mu_{ij}\mu'_{ij} + \epsilon_1)(2\sigma_{ij,i'j'} + \epsilon_2)}{((\mu_{ij})^2 + (\mu'_{ij})^2 + \epsilon_1)((\sigma_{ij})^2 + (\sigma'_{ij})^2 + \epsilon_2)}. \tag{8}$$

The final SSIM score of the entire image is then computed by simply averaging the local values over all pixels of the image

$$\mathrm{SSIM} = \frac{1}{mn}\sum_{i=1}^{m}\sum_{j=1}^{n}\mathrm{M}_{ij}. \tag{9}$$

### 2.4. Feature based image distance measure

A more powerful measure can be developed by identifying local features in the images and comparing the type and location of these features. The features are local maxima, minima, and corners and they are detected at certain locations in the images. These are called interest points or keypoints in the SURF framework [17]. Then, a descriptor vector is generated for each keypoint thereby providing a unique fingerprint to distinguish one keypoint from other keypoints. Finally, keypoint locations and the descriptor vectors are matched between the images using a Euclidean distance measure. The implementation of the SURF algorithm in the open-source computer vision library (OpenCV) [18] is used here. For more details on the SURF algorithm, the reader is referred to Ref. [17].

The keypoints are extracted using the SURF keypoint detector which uses the determinant of the Hessian matrix. This step produces a large number of key points, some of which are redundant. The hierarchical agglomerative clustering (HAC) [19] with average linkage criterion [20] is then used to merge keypoints that are closer than a Euclidean distance criterion, here chosen to be $t_1$=5 pixels. Figure 1 shows a set of detected keypoints as color-coded circles superimposed on an experimental AC-STEM image (taken from Ref. [10]). The radius of each circle is proportional to the scale at which the key point was detected. The color bar shows the strength of the keypoints. More distinctive features, such as brighter blobs, have a stronger Hessian response. The figure also shows the results of HAC clustering of the key points to simplify the results of the keypoint analysis.

After keypoints have been identified and refined, a descriptor is computed for each one. For more distinctiveness, we use the extended 128 dimensional version of the SURF descriptor. We also use Upright-SURF to improve speed as rotational invariance is not required for our application. To compare an image to a reference image, each feature in the reference image is compared to all features in the test image by calculating the Euclidean

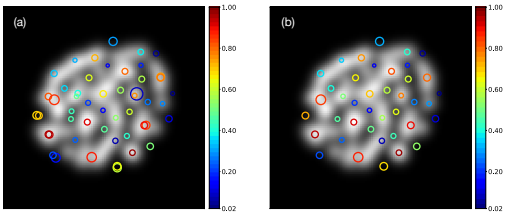


FIG. 1. Keypoints extracted from an experimental AC-STEM image from Ref. [10] are superimposed as color coded circles. The color bars show the color relates to the strength of each keypoint. (a) Shows 50 keypoints originally detected, some of them overlapping. (b) Shows the keypoints after hierarchical agglomerative clustering where the number of keypoints is reduced to 40.

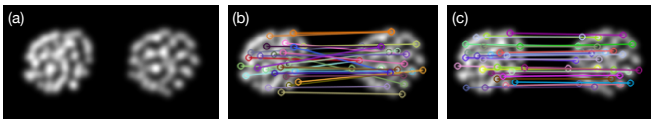


FIG. 2. (a) Experimental AC-STEM image [10] (left) and simulated image from atomic structure S10, taken from Ref. [14] (right). (b) Matches obtained by comparing descriptors only. (c) Matches obtained by taking the locations of the keypoints into account.

distance between their descriptors. For each keypoint in the reference image, the best three candidates in the test image are identified. The one with the smallest spatial distance is selected if it lies within a threshold of $t_2 = 1.5t_1$ pixels from the reference keypoint where $t_1$ denotes the threshold used in the HAC clustering. This matching strategy eliminates many of the false matches without significantly affecting the correct ones. Figure 2 shows an example of feature matching with and without taking into account the location of the keypoints.

The feature based image distance (FBID) measure proposed here is a combination of the descriptor distances $d_s$ and spatial distance $d_p$ plus a weighted fraction of the number keypoints for which matches are not found. The new distance measure FBID is defined as

$$\mathrm{FBID} = \sum_{i}^{N_k} (d_p)_i \, (d_s)_i + \gamma \, \frac{N_k - N_m}{N_k} \tag{10}$$

where $N_k$ is the total number of keypoints in the reference image and $N_m$ is the number of keypoints for which correct matches are found. The weight parameter $\gamma$ is introduced to balance the two terms in the equation. The descriptor distance $d_s$ between two descriptors $D$ and $D'$ is calculated as:

$$d_s = \sqrt{\sum_{i=1}^{N_d} (D_i - D'_i)^2}, \tag{11}$$

where $N_d = 128$ denotes the number of dimensions of the descriptors. The spatial distance $d_p$ between the locations of the two keypoints is calculated as

$$d_p = \sqrt{(x - x')^2 + (y - y')^2}, \tag{12}$$

where $(x, y)$ and $(x', y')$ are the coordinates of the keypoints.

## 3. Results

Calculations of the various measures were carried out for a set of simulated images in a comparison with an experimental AC-STEM image reported by Wang and Palmer [10].

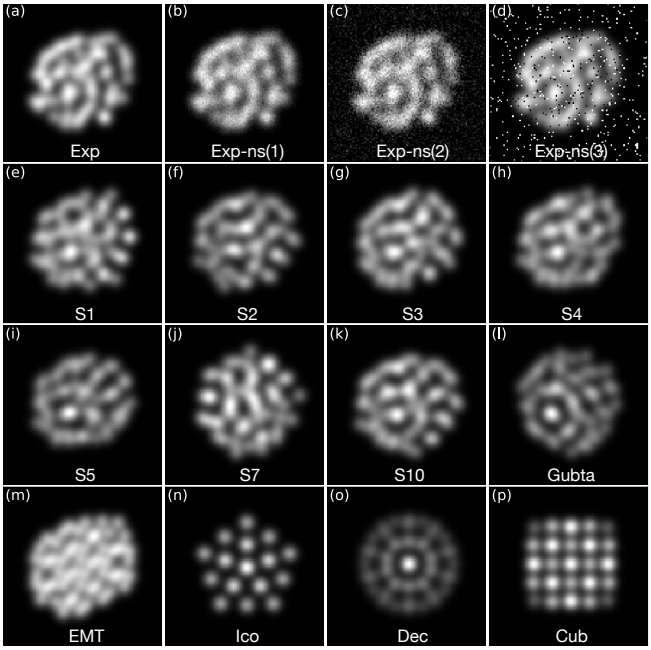


FIG. 3. Comparison of simulated images of $Au_{55}$ $(e-p)$ with an experimental image $(a)$. Images $(b-d)$ are same as (a) but corrupted with speckle, Gaussian and salt-and-pepper noise.

Figure 3 shows the experimental image $(a)$ and the 15 test images. Images $(b - d)$ are the same as the experimental image, but the image has been corrupted with speckle, Gaussian and salt-and-pepper noise, respectively. They are referred to as Exp-ns(1-3). With

the exception of small changes in intensity, the corrupted images are visually similar to the original image. The Gaussian and speckle noises were sampled from the normal distribution with zero mean and standard deviation of 0.1. The salt-and-pepper noise was produced by adding random bright and dark pixels to about 10% of the image pixels. It looks noticeably corrupted by the noise. Images $(e-k)$ were simulated from atomic coordinates of $Au_{55}$ structures presented in Ref. [14]. They correspond to structures $S1-S5$, $S7$ and $S10$ using the notation used in the article. The algorithm for extracting 3D structures from AC-STEM images can be found in our recent articles [13, 14]. Images $(l)$ and $(m)$ were generated from the global minimum structure obtained from the Gupta potential by Garzón [12] and the global minimum structure obtained from effective medium theory (EMT) potential function [21], respectively. They are referred to as EMT and Gupta. The last 3 images, $(n-p)$, are generated from ordered $Au_{55}$ structures belonging to icosahedral, decahedral and cuboctahedral (face centered cubic) structures. They are referred to as Ico, Dec and Cub, and are visually different from the reference image in content, shape and brightness and are included here to represent outliers. All the images have the same size of $160 \times 160$ pixels.

Table 1 lists the various calculated measures, MSE, SSIM and the FBID, for the comparison of the 15 test images with the experimental AC-STEM image. For each measure, the images are ranked based on the calculated value, the lower value of the measure indicating a better fit. The image with the lowest value was ranked as 1 and the image with the highest valued ranked as 15. For each measure, image $(a)$ necessarily has a value of zero since it is the reference image.

## 4. Discussion

The values obtained for images Exp-ns(1-3) test how robust the various measures are towards noise. The speckle, Gaussian and salt-and-pepper noise corrupted images are indeed found to be the first, second and third closest matches with the FBID. This is reassuring as it is consistent with the visual similarity of the noisy images with the original. The MSE measure fails to recognize the similarity of image Exp-ns(2) which includes Gaussian noise, and the SSIM fails to recognize both image Exp-ns(2) and image Exp-ns(3), the latter having salt-and-pepper noise. These measures are, therefore, found to be vulnerable to noise.

The results for Ico, Dec and Cub structures are interesting and particularly important, as these cluster structures are far from being optimal for $Au_{55}$ and the corresponding images are in not similar to the experimental image. Nevertheless, the MSE and SSIM measures indicate a better match for these images than some of the noisy images derived from the experimental image. The MSE even gives a preference to these images over images generated from optimized $Au_{55}$ structures, such as the structure obtained with the Gupta potential function.

The lowest energy cluster structure according to the EMT potential is completely different from any of the $Au_{55}$ structures obtained with higher level theoretical methods and the image calculated from it bears no similarity to the experimental image. This is essentially a structure characteristic of the face centered cubic ordering of the crystal. Yet, the SSIM measure indicates a closer match than the Gupta structure. This shows that the SSIM measure is not reliable. The MSE measure also gives nearly the same value for the EMT structure as the Gupta structure, showing that it cannot be trusted.

The FBID measure correctly places images for EMT, Ico, Dec and Cub at the bottom of the list. It, furthermore, gives ranking to the images of low energy $Au_{55}$ structures that corresponds well with visual inspection. The image for structure $S4$ is deemed best, as was concluded in Ref. [14], and the image for $S3$ second best. The cluster with lowest DFT

TABLE 1. Comparison of the MSE, IMSE, SSIM and FBID measures for matching the images shown in Figure 3 with the experimental AC-STEM image of a $Au_{55}$ cluster. Images labeled Exp-ns(1-3) are the AC-STEM image with speckle, Gaussian and salt/pepper noise added, resp. Images labeled $S1$-$S10$ refer to $Au_{55}$ structures presented in Ref. [14]. Images labeled EMT and Gupta are obtained from the lowest energy structure predicted by the effective medium theory and Gupta potential functions, resp. *Ico* stands for icosahedron, *Dec* for the Ino-decahedron and *Cub* for a cuboctahedral cluster carved out of the face centered cubic crystal. All but the Exp-ns(1-3) and $S1$-$S10$ images are based on structures that have been minimized locally using DFT/PBEsol and rotated in order to minimize the MSE.

| MSE | | IMSE | | SSIM | | FBID | |
|---|---|---|---|---|---|---|---|
| Value | Config. | Value | Config. | Value | Config. | Value | Config. |
| 0.0045 | Exp-ns(1) | 0.050 | Exp-ns(1) | 0.018 | Exp-ns(1) | 0.068 | Exp-ns(1) |
| 0.0320 | S4 | 0.232 | S4 | 0.099 | S4 | 0.076 | Exp-ns(2) |
| 0.0383 | S1 | 0.285 | S1 | 0.108 | S2 | 0.143 | Exp-ns(3) |
| 0.0404 | S3 | 0.305 | S3 | 0.109 | S1 | 0.396 | S4 |
| 0.0430 | EMT | 0.311 | S5 | 0.111 | S10 | 0.434 | S3 |
| 0.0448 | S2 | 0.316 | S10 | 0.112 | S3 | 0.494 | S10 |
| 0.0459 | S10 | 0.393 | S2 | 0.122 | S5 | 0.496 | S1 |
| 0.0490 | S5 | 0.414 | Exp-ns(3) | 0.149 | EMT | 0.502 | S2 |
| 0.0584 | Exp-ns(2) | 0.423 | Exp-ns(2) | 0.170 | Gupta | 0.505 | S5 |
| 0.0601 | S7 | 0.441 | EMT | 0.184 | Cub | 0.574 | Gupta |
| 0.0750 | Gupta | 0.591 | Gupta | 0.196 | Dec | 0.578 | S7 |
| 0.1074 | Ico | 0.702 | S7 | 0.200 | S7 | 0.603 | EMT |
| 0.1127 | Cub | 0.935 | Cub | 0.203 | Ico | 0.606 | Cub |
| 0.1509 | Exp-ns(3) | 1.073 | Ico | 0.663 | Exp-ns(3) | 0.661 | Ico |
| 0.2461 | Dec | 1.831 | Dec | 0.829 | Exp-ns(2) | 0.765 | Dec |

energy, $S10$ is identified as the third best. This is reassuring and shows that the FBID measure is providing numerical ranking that is consistent with visual inspection as well as known quality of the atomic structures of the clusters. This measure could be used in future AC-STEM analysis. It is, however, not differentiable so it is not as easy to optimize atomic structure directly from a comparison with an AC-STEM image as the MSE and IMSE measures. A practical way forward in that respect may be to develop IMSE by adjusting weights and penalty measures in such a way as to get agreement with ranking from FBID for a set of test images and the use the obtained IMSE in structure optimization.

## 5. Acknowledgements

This work was supported by the Icelandic Research Fund and the University of Iceland Research Fund. KS was supported by a fellowship from the University of Iceland Doctoral Fund. We thank Alejandro Peña-Torres for helpful discussions and Ignacio Garzón for providing us with the atomic coordinates in the optimal $Au_{55}$ structure deduced from the Gupta potential function. The calculations were carried out at the Icelandic Research High Performance Computing (IRHPC) center at the University of Iceland.

### References


[1] Haruta M. Gold as a novel catalyst in the 21st century: Preparation, working mechanism and applications. *Gold bulletin*, 2004, **37**, P. 27.

[2] Metal Nanoclusters in Catalysis and Materials Science: The Issue of Size Control. Corain B., Schmid G., Toshima N. (eds), Elsevier Science, 2011.

[3] Ray P.C. Size and shape dependent second order nonlinear optical properties of nanomaterials and their application in biological and chemical sensing. *Chemical Reviews*, 2010, **110**, P. 5332.

[4] Liu J.P., Fullerton E., Gutfleisch O., Sellmyer D.J. (Eds.) Nanoscale Magnetic Materials and Applications. Springer US, 2014.

[5] Valden M., Lai X., Goodman D.W. Onset of catalytic activity of gold clusters on titania with the appearance of nonmetallic properties. *Science*, 1998, **281**, P. 1647.

[6] Cuenya B.R. Synthesis and catalytic properties of metal nanoparticles: Size, shape, support, composition, and oxidation state effects. *Thin Solid Films*, 2010, **518**, P. 3127.

[7] Krivanek O.L., Dellby N., Lupini A.R. Towards sub-Å electron beams. *Ultramicroscopy*, 1999, **78**(1-4), P. 1.

[8] Batson P.E., Dellby N., Krivanek, O.L. Sub-Åangstrom resolution using aberration corrected electron optics. *Nature*, 2002, **418**, P. 617.

[9] Li Z.Y., Young N.P., Di Vece M., Palomba S., Palmer R.E. , Bleloch A.L., Curley B.C., Johnston R.L., Jiang J., Yuan J. Three-dimensional atomic-scale structure of size-selected gold nanoclusters. *Nature*, 2008, **451**, P. 46.

[10] Wang Z.W., Palmer R.E. Experimental evidence for fluctuating, chiral-type $Au_{55}$ clusters by direct atomic imaging. *Nano Letters*, 2012, **12**, P. 5510.

[11] Yu M., Yankovich A.B., Kaczmarowski A., Morgan D., Voyles P.M. Integrated computational and experimental structure refinement for nanoparticles. *ACS Nano*, 2016, **10**, P. 4031.

[12] Garzón I.L. *et al.* Lowest energy structures of gold nanoclusters. *Phys. Rev. Letters*, 1998, **81**, P. 1600.

[13] Sukuta K., Van den Bossche M., Pedersen A., Jónsson H. Nanocluster structure deduced from AC-STEM images coupled to theoretical modelling. *Nanosystems: Physics, Chemistry, mathematics*, 2017, **8**, P.723.

[14] Bersha K.S., Pena-Torres A., Jónsson H. Systematic analysis of AC-STEM images to extract atomic structure of $Au_{55}$ clusters. *arXiv*, 2021.

[15] Wang Z., Bovik A.C. Modern image quality assessment. In *Synthesis Lectures on Image, Video, and Multimedia Processing*, Morgan & Claypool Publishers (2006).

[16] Wang Z., Bovik A.C., Sheikh H.R., Simoncelli E.P. Image quality assessment: from error visibility to structural similarity. *IEEE Transactions on Image Processing*, 2004, **13**, P. 600.

[17] Bay H., Tuytelaars T., Van Gool L. SURF: Speeded Up Robust Features. In: Leonardis A., Bischof H., Pinz A. (eds) Computer Vision – ECCV 2006. ECCV 2006. *Lecture Notes in Computer Science*, **3951**. Springer, Berlin, Heidelberg.

[18] Bradski, G. The OpenCV Library. Dr. Dobb's Journal of Software Tools, 2000, **120**, P. 122.

[19] Müllner D. Modern hierarchical, agglomerative clustering algorithms. 2011, arXiv: 1109.2378.

[20] Bar-Joseph Z., Gifford D.K., Jaakkola T.S. Fast optimal leaf ordering for hierarchical clustering. *Bioinformatics*, 2001, **17**, P. S22.

[21] Jacobsen K.W., Stoltze P., Nørskov J.K. A semi-empirical effective medium theory for metals and alloys. *Surf. Sci. 1996*, **366** 394.

# References


[1] Badri Bhattarai, Yeakub Zaker, Aydar Atnagulov, Bokwon Yoon, Uzi Landman, and Terry P Bigioni. Chemistry and structure of silver molecular nanoparticles. *Accounts of chemical research*, 51(12):3104–3113, 2018.

[2] Indranath Chakraborty and Thalappil Pradeep. Atomically precise clusters of noble metals: emerging link between atoms and nanoparticles. *Chemical reviews*, 117(12):8208–8271, 2017.

[3] C Stephenson and A Hubler. Stability and conductivity of self assembled wires in a transverse electric field. *Scientific reports*, 5(1):1–9, 2015.

[4] JP Wilcoxon and BL Abrams. Synthesis, structure and properties of metal nanoclusters. *Chemical Society Reviews*, 35(11):1162–1194, 2006.

[5] Andrew A Herzing, Christopher J Kiely, Albert F Carley, Philip Landon, and Graham J Hutchings. Identification of active gold nanoclusters on iron oxide supports for co oxidation. *Science*, 321(5894):1331–1335, 2008.

[6] Mika Valden, Xiaofeng Lai, and D Wayne Goodman. Onset of catalytic activity of gold clusters on titania with the appearance of nonmetallic properties. *science*, 281(5383):1647–1650, 1998.

[7] Britt Hvolbæk, Ton VW Janssens, Bjerne S Clausen, Hanne Falsig, Claus H Christensen, and Jens K Nørskov. Catalytic activity of au nanoparticles. *Nano Today*, 2(4):14–18, 2007.

[8] Gang Han, Partha Ghosh, and Vincent M Rotello. Functionalized gold nanoparticles for drug delivery. 2007.

[9] Ximei Qian, Xiang-Hong Peng, Dominic O Ansari, Qiqin Yin-Goen, Georgia Z Chen, Dong M Shin, Lily Yang, Andrew N Young, May D Wang, and Shuming Nie. In vivo tumor targeting and spectroscopic detection with surface-enhanced raman nanoparticle tags. *Nature biotechnology*, 26(1):83–90, 2008.

[10] Puskal Kunwar, Jukka Hassinen, Godofredo Bautista, Robin HA Ras, and Juha Toivonen. Direct laser writing of photostable fluorescent silver nanoclusters in polymer films. *ACS nano*, 8(11):11165–11171, 2014.

[11] David T Thompson. Using gold nanoparticles for catalysis. *Nano Today*, 2(4): 40–43, 2007.

[12] Geoffrey C Bond, Catherine Louis, and David Thompson. *Catalysis by gold*, volume 6. World Scientific, 2006.

[13] Christopher W Corti, Richard J Holliday, and David T Thompson. Progress towards the commercial application of gold catalysts. *Topics in catalysis*, 44(1-2): 331–343, 2007.

[14] Li Xiao, Bethany Tollberg, Xiankui Hu, and Lichang Wang. Structural study of gold clusters. *The Journal of chemical physics*, 124(11):114309, 2006.

[15] Gianluca Santarossa, Angelo Vargas, Marcella Iannuzzi, and Alfons Baiker. Free energy surface of two-and three-dimensional transitions of au 12 nanoclusters obtained by ab initio metadynamics. *Physical Review B*, 81(17):174205, 2010.

[16] Mikael P Johansson, Ingolf Warnke, Alexander Le, and Filipp Furche. At what size do neutral gold clusters turn three-dimensional? *The Journal of Physical Chemistry C*, 118(50):29370–29377, 2014.

[17] I. L. Garzón, K. Michaelian, M. R. Beltrán, A. Posada-Amarillas, P. Ordejón, E. Artacho, D. Sánchez-Portal, and J. M. Soler. Lowest energy structures of gold nanoclusters. *Phys. Rev. Lett.*, 81:1600–1603, Aug 1998.

[18] D Schebarchov, F Baletto, and DJ Wales. Structure, thermodynamics, and rearrangement mechanisms in gold clusters—insights from the energy landscapes framework. *Nanoscale*, 10(4):2004–2016, 2018.

[19] Sumio Iijima and Toshinari Ichihashi. Structural instability of ultrafine particles of metals. *Physical review letters*, 56(6):616, 1986.

[20] ZW Wang and RE Palmer. Experimental evidence for fluctuating, chiral-type $au_{55}$ clusters by direct atomic imaging. *Nano letters*, 12(11):5510–5514, 2012.

[21] ZY Li, NP Young, Marcel Di Vece, S Palomba, RE Palmer, AL Bleloch, BC Curley, RL Johnston, J Jiang, and Jun Yuan. Three-dimensional atomic-scale structure of size-selected gold nanoclusters. *Nature*, 451(7174):46–48, 2008.

[22] Hui Li, Lei Li, Andreas Pedersen, Yi Gao, Navneet Khetrapal, Hannes Jónsson, and Xiao Cheng Zeng. Magic-number gold nanoclusters with diameters from 1 to 3.5 nm: Relative stability and catalytic activity for co oxidation. *Nano letters*, 15 (1):682–688, 2015.

[23] Günter Schmid, Reinhard Pfeil, Roland Boese, Friedhelm Bandermann, Sonja Meyer, Gijs HM Calis, and Jan WA van der Velden. Au55 [p (c6h5) 3] 12ci6—ein goldcluster ungewöhnlicher größe. *Chemische Berichte*, 114(11):3634–3642, 1981.

[24] Guenter Schmid. The relevance of shape and size of au 55 clusters. *Chemical Society Reviews*, 37(9):1909–1930, 2008.

[25] Matthew A Marcus, Mark P Andrews, Jorg Zegenhagen, Arun S Bommannavar, and Pedro Montano. Structure and vibrations of chemically produced au 55 clusters. *Physical Review B*, 42(6):3312, 1990.

[26] Mary C Fairbanks, Robert E Benfield, Robert J Newport, and Gunter Schmid. An exafs study of the cluster molecule au55 (pph3) 12cl6. *Solid state communications*, 73(6):431–436, 1990.

[27] Kuo Bao, Stefan Goedecker, Kenji Koga, Frédéric Lançon, and Alexey Neelov. Structure of large gold clusters obtained by global optimization using the minima hopping method. *Physical Review B*, 79(4):041405, 2009.

[28] Jonathan PK Doye and David J Wales. Global minima for transition metal clusters described by sutton–chen potentials. *New journal of chemistry*, 22(7):733–744, 1998.

[29] W Vogel, B Rosner, and B Tesche. Structural investigations of gold (au55) organometallic complexes by x-ray powder diffraction and transmission electron microscopy. *The Journal of Physical Chemistry*, 97(45):11611–11616, 1993.

[30] Hannu Häkkinen, Michael Moseler, Oleg Kostko, Nina Morgner, Margarita Astruc Hoffmann, and Bernd v Issendorff. Symmetry and electronic structure of noble-

metal nanoparticles and the role of relativity. *Physical review letters*, 93(9):093401, 2004.

[31] Wei Huang, Min Ji, Chuan-Ding Dong, Xiao Gu, Lei-Ming Wang, Xin Gao Gong, and Lai-Sheng Wang. Relativistic effects and the unique low-symmetry structures of gold nanoclusters. *Acs Nano*, 2(5):897–904, 2008.

[32] Nathalie Tarrat, Mathias Rapacioli, Jérôme Cuny, Joseph Morillo, Jean-Louis Heully, and Fernand Spiegelman. Global optimization of neutral and charged 20-and 55-atom silver and gold clusters at the dftb level. *Computational and Theoretical Chemistry*, 1107:102–114, 2017.

[33] Maxime Van den Bossche. Dftb-assisted global structure optimization of 13- and 55-atom late transition metal clusters. *The Journal of Physical Chemistry A*, 123 (13):3038–3045, 2019.

[34] KW Jacobsen, JK Norskov, and Martti J Puska. Interatomic interactions in the effective-medium theory. *Physical Review B*, 35(14):7423, 1987.

[35] Raju P Gupta. Lattice relaxation at a metal surface. *Physical Review B*, 23(12): 6265, 1981.

[36] Vittorio Rosato, M Guillope, and B Legrand. Thermodynamical and structural properties of fcc transition metals using a simple tight-binding model. *Philosophical Magazine A*, 59(2):321–336, 1989.

[37] Manfred Von Ardenne. Das elektronen-rastermikroskop. *Zeitschrift für Physik*, 109(9):553–572, 1938.

[38] DH Shin, EJ Kirkland, and J Silcox. Annular dark field electron microscope images with better than 2 å resolution at 100 kv. *Applied physics letters*, 55(23): 2456–2458, 1989.

[39] Christian Kisielowski, B Freitag, M Bischoff, H Van Lin, S Lazar, Georg Knippels, Peter Tiemeijer, Maarten van der Stam, Sebastian von Harrach, Michael Stekelenburg, et al. Detection of single atoms and buried defects in three dimensions by aberration-corrected electron microscope with 0.5-å information limit. *Microscopy and Microanalysis*, 14(5):469, 2008.

[40] Qing-Hua Zhang, Dong-Dong Xiao, and Lin Gu. Aberration-corrected scanning transmission electron microscopy for complex transition metal oxides. *Chinese Physics B*, 25(6):066803, 2016.

[41] JM Cowley, MS Hansen, and S-Y Wang. Imaging modes with an annular detector in stem. *Ultramicroscopy*, 58(1):18–24, 1995.

[42] Robert Hovden and David A Muller. Efficient elastic imaging of single atoms on ultrathin supports in a scanning transmission electron microscope. *Ultramicroscopy*, 123:59–65, 2012.

[43] Ian MacLaren and Quentin M Ramasse. Aberration-corrected scanning transmission electron microscopy for atomic-resolution studies of functional oxides. *International Materials Reviews*, 59(3):115–131, 2014.

[44] Max T Otten. High-angle annular dark-field imaging on a tem/stem system. *Journal of electron microscopy technique*, 17(2):221–230, 1991.

[45] Stephen J Pennycook, Matthew F Chisholm, Andrew R Lupini, M Varela, Albina Y Borisevich, Mark P Oxley, WD Luo, Klaus van Benthem, S-H Oh, DL Sales, et al. Aberration-corrected scanning transmission electron microscopy: from atomic imaging and analysis to solving energy problems. *Philosophical Transactions*

*of the Royal Society A: Mathematical, Physical and Engineering Sciences*, 367 (1903):3709–3733, 2009.

[46] PE Batson, AG Domenicucci, and E Lemoine. Atomic resolution electronic structure in device development. *Microscopy and Microanalysis*, 3(S2):645–646, 1997.

[47] Niklas Dellby, L Krivanek, D Nellist, E Batson, and R Lupini. Progress in aberration-corrected scanning transmission electron microscopy. *Microscopy*, 50 (3):177–185, 2001.

[48] Jingyue Liu. Scanning transmission electron microscopy and its application to the study of nanoparticles and nanoparticle systems. *Journal of electron microscopy*, 54(3):251–278, 2005.

[49] Sergey N Rashkeev, Andrew R Lupini, Steven H Overbury, Stephen J Pennycook, and Sokrates T Pantelides. Role of the nanoscale in catalytic co oxidation by supported au and pt nanostructures. *Physical Review B*, 76(3):035438, 2007.

[50] John M Cowley and A F_ Moodie. The scattering of electrons by atoms and crystals. i. a new theoretical approach. *Acta Crystallographica*, 10(10):609–619, 1957.

[51] Earl J Kirkland. *Advanced computing in electron microscopy*. Springer, 1998.

[52] Min Yu, Andrew B. Yankovich, Amy Kaczmarowski, Dane Morgan, and Paul M. Voyles. Integrated computational and experimental structure refinement for nanoparticles. *ACS Nano*, 10(4):4031–4038, 2016.

[53] SJ Pennycook and LA Boatner. Chemically sensitive structure-imaging with a scanning transmission electron microscope. *Nature*, 336(6199):565–567, 1988.

[54] Tony Lindeberg. Scale selection properties of generalized scale-space interest point detectors. *Journal of Mathematical Imaging and vision*, 46(2):177–210, 2013.

[55] Karsten W Jacobsen, Per Stoltze, and JK Nørskov. A semi-empirical effective medium theory for metals and alloys. *Surface Science*, 366(2):394–402, 1996.

[56] R Kilaas. Optimal and near-optimal filters in high-resolution electron microscopy. *Journal of Microscopy*, 190(1-2):45–51, 1998.

[57] Samuel T Chill, Matthew Welborn, Rye Terrell, Liang Zhang, Jean-Claude Berthet, Andreas Pedersen, Hannes Jónsson, and Graeme Henkelman. EON: software for long time simulations of atomic scale systems. *Modelling and Simulation in Materials Science and Engineering*, 22(5):055002, may 2014.

[58] Manuel Plasencia, Andreas Pedersen, Andri Arnaldsson, Jean-Claude Berthet, and Hannes Jónsson. Geothermal model calibration using a global minimization algorithm based on finding saddle points and minima of the objective function. *Computers & Geosciences*, 65:110 – 117, 2014. ISSN 0098-3004.

[59] Andreas Pedersen, Jean-Claude Berthet, and Hannes Jónsson. Simulated annealing with coarse graining and distributed computing. In *International Workshop on Applied Parallel Computing*, pages 34–44. Springer, 2010.

[60] Graeme Henkelman and Hannes Jónsson. A dimer method for finding saddle points on high dimensional potential surfaces using only first derivatives. *The Journal of Chemical Physics*, 111(15):7010–7022, 1999.

[61] D.M. Daven, N. Tit, J.R. Morris, and K.M. Ho. Structural optimization of lennard-jones clusters by a genetic algorithm. *Chemical Physics Letters*, 256(1):195 – 200,

1996. ISSN 0009-2614.

[62] Ask Hjorth Larsen, Jens Jørgen Mortensen, Jakob Blomqvist, Ivano E Castelli, Rune Christensen, Marcin Dułak, Jesper Friis, Michael N Groves, Bjørk Hammer, Cory Hargus, Eric D Hermes, Paul C Jennings, Peter Bjerre Jensen, James Kermode, John R Kitchin, Esben Leonhard Kolsbjerg, Joseph Kubal, Kristen Kaasbjerg, Steen Lysgaard, Jón Bergmann Maronsson, Tristan Maxson, Thomas Olsen, Lars Pastewka, Andrew Peterson, Carsten Rostgaard, Jakob Schiøtz, Ole Schütt, Mikkel Strange, Kristian S Thygesen, Tejs Vegge, Lasse Vilhelmsen, Michael Walter, Zhenhua Zeng, and Karsten W Jacobsen. The atomic simulation environment—a python library for working with atoms. *Journal of Physics: Condensed Matter*, 29(27):273002, 2017.

[63] S. R. Bahn and K. W. Jacobsen. An object-oriented scripting interface to a legacy electronic structure code. *Comput. Sci. Eng.*, 4(3):56–66, MAY-JUN 2002. ISSN 1521-9615.

[64] Matthew D. Wolf and Uzi Landman. Genetic algorithms for structural cluster optimization. *The Journal of Physical Chemistry A*, 102(30):6129–6137, 1998.

[65] Jorge Nocedal and Stephen J. Wright. *Numerical Optimization*. Springer, New York, NY, USA, second edition, 2006.

[66] Nuno Ricardo Costa and João Alves Lourenço. Exploring pareto frontiers in the response surface methodology. In *Transactions on Engineering Technologies*, pages 399–412. Springer, 2015.

[67] John P. Perdew, Adrienn Ruzsinszky, Gábor I. Csonka, Oleg A. Vydrov, Gustavo E. Scuseria, Lucian A. Constantin, Xiaolan Zhou, and Kieron Burke. Restoring the density-gradient expansion for exchange in solids and surfaces. *Phys. Rev. Lett.*, 100:136406, Apr 2008.

[68] Mikael P. Johansson, Anne Lechtken, Detlef Schooss, Manfred M. Kappes, and Filipp Furche. 2d-3d transition of gold cluster anions resolved. *Phys. Rev. A*, 77: 053202, May 2008.

[69] Matthew Fishman, Houlong L Zhuang, Kiran Mathew, William Dirschka, and Richard G Hennig. Accuracy of exchange-correlation functionals and effect of solvation on the surface energy of copper. *Physical Review B*, 87(24):245402, 2013.

[70] G. Kresse and J. Furthmüller. Efficient iterative schemes for ab initio total-energy calculations using a plane-wave basis set. *Phys. Rev. B*, 54:11169–11186, Oct 1996.

[71] Zhi Wei Wang, Outi Toikkanen, Bernadettte M. Quinn, and Richard E. Palmer. Real-space observation of prolate monolayer-protected au38 clusters using aberration-corrected scanning transmission electron microscopy. *Small*, 7(11): 1542–1545, 2011.

[72] Z. W. Wang and R. E. Palmer. Determination of the ground-state atomic structures of size-selected au nanoclusters by electron-beam-induced transformation. *Phys. Rev. Lett.*, 108:245502, Jun 2012.

[73] D. Porezag, Th. Frauenheim, Th. KÃ¶hler, G. Seifert, and R. Kaschner. Construction of tight-binding-like potentials on the basis of density-functional theory: Application to carbon. *Physical Review B*, 51(19):12947–12957, 1995.

[74] Daniel Faken and Hannes Jónsson. Systematic analysis of local atomic structure

combined with 3d computer graphics. *Computational Materials Science*, 2(2):279 – 286, 1994. ISSN 0927-0256.

[75] J. Dana. Honeycutt and Hans C. Andersen. Molecular dynamics study of melting and freezing of small lennard-jones clusters. *The Journal of Physical Chemistry*, 91(19):4950–4963, 1987.

[76] Andrew S. Clarke and Hannes Jónsson. Structural changes accompanying densification of random hard-sphere packings. *Phys. Rev. E*, 47:3975–3984, Jun 1993.

[77] Alexander Stukowski. Structure identification methods for atomistic simulations of crystalline materials. *Modelling and Simulation in Materials Science and Engineering*, 20(4):045021, may 2012. doi: 10.1088/0965-0393/20/4/045021.

[78] Graeme Henkelman, Blas P. Uberuaga, and Hannes Jónsson. A climbing image nudged elastic band method for finding saddle points and minimum energy paths. *The Journal of Chemical Physics*, 113(22):9901–9904, 2000.

[79] Graeme Henkelman and Hannes Jónsson. Improved tangent estimate in the nudged elastic band method for finding minimum energy paths and saddle points. *The Journal of Chemical Physics*, 113(22):9978–9985, 2000.

[80] Herbert Bay, Tinne Tuytelaars, and Luc Van Gool. Surf: Speeded up robust features. In Aleš Leonardis, Horst Bischof, and Axel Pinz, editors, *Computer Vision – ECCV 2006*, pages 404–417, Berlin, Heidelberg, 2006. Springer Berlin Heidelberg. ISBN 978-3-540-33833-8.

[81] Christopher Evans. Notes on the opensurf library. *University of Bristol, Tech. Rep. CSTR-09-001, January*, (1), 2009.

[82] Franklin C Crow. Summed-area tables for texture mapping. In *Proceedings of the 11th annual conference on Computer graphics and interactive techniques*, pages 207–212, 1984.

[83] Stefan Leutenegger, Margarita Chli, and Roland Y Siegwart. Brisk: Binary robust invariant scalable keypoints. In *2011 International conference on computer vision*, pages 2548–2555. Ieee, 2011.

[84] David G Lowe. Object recognition from local scale-invariant features. In *Proceedings of the seventh IEEE international conference on computer vision*, volume 2, pages 1150–1157. Ieee, 1999.

[85] Matthew Brown and David G Lowe. Invariant features from interest point groups. In *BMVC*, volume 4. Citeseer, 2002.

[86] Tony Lindeberg and Lars Bretzner. Real-time scale selection in hybrid multi-scale representations. In *International Conference on Scale-Space Theories in Computer Vision*, pages 148–163. Springer, 2003.

[87] G. Bradski. The OpenCV Library. *Dr. Dobb's Journal of Software Tools*, 2000.